Paint It Black: Weak Lensing Analysis of an All-Sky Simulation

A thesis presented
by

Carlos López-Arenillas

to the
Department of Astronomy and Meteorology

in partial fulfillment of the requirements
for the degree of

Doctor of Philosophy

in the subject of

Physics

Thesis Director: Dr. Enrique Gaztañaga
Thesis Co-Director: Dr. Pablo Fosalba
Thesis Tutor: Dr. Alberto Manrique

 doi:10.20944/preprints202303.0387.v1

Abstract

Paint It Black: Weak Lensing Analysis of an All-Sky Simulation

Carlos López-Arenillas

2013

This Thesis is concerned with one of the most promising probes to constrain the "Dark Universe", and, particularly, the dark matter distribution. Based on MICE cosmological simulation, and the all-sky convergence maps generated by Fosalba et al. [58], we perform a mass calibration of the dark matter halos there contained up to z=1. In order to do that, we analyse the average halo density profiles of all the halos with masses ranging from 5×10^{13} to 3.751×10^{14} $h^{-1}M_{\odot}$, divided into four mass bins and three redshift bins. Through this analysis we address two main issues: the relatively low mass resolution of the simulation (m_p=2.34×10^{11} $h^{-1}M_{\odot}$) and the relatively high softening length (l_{soft}=50 h^{-1} Kpc). We do that by using a two-step procedure. First, we simulate analytical pure NFW density profiles (with different mass resolutions) using two input values: the virial radii of MICE halos and the expected concentrations, according to the fixed mass-concentration relation from Oguri and Hamana [130]. Second, we model the effect of the softening length with a Gaussian filter, smoothing the halo core. The results show that MICE halos are, in average, NFW halos. Best-fit NFW radii are in very good agreement with the average radii of our samples, overestimating the data by ∼1%, but best-fit NFW concentrations are in average 50% lower than the expected values. It is possible to account for part of this deviation by distinguishing between relaxed and unrelaxed halos, finding that, depending on the degree of relaxedness, the improvement can be as high as 30%. We also find that the analytical NFW halos simulated with MICE mass resolution have an overall concentration 40% lower than the input concentration, in the case of 3D profiles, and 25% lower in that of the projected profiles. The Gaussian-smoothed NFW profile is a good approximation for our projected halos. Additionally, we analyse the morphology of the halos, characterizing their triaxiality at R_{200} and calculating their orientation with respect to the line-of-sight (LOS). MICE halos tend to adopt a more prolate morphology, as might be expected from a ΛCDM simulation (Shaw et al. [159]), and the

 doi:10.20944/preprints202303.0387.v1

percentage of prolate halos grows as their mass grows. The mass resolution is, nonetheless, not good enough to draw conclusive inferences from the shape analysis, but it allows us to discern a trend and estimate the effect of halo shape and orientation on the weak lensing masses. Finally, we use the all-sky convergence maps to study the scatter in mass measurements of MICE halos. We determine the intrinsic scatter in the recovered masses by assuming the smoothed NFW profile as the "true" profile, and creating two new convergence maps from different mass cuts. We estimate also the scatter due to the correlated structure by studying the angles between the major axes of the halos and the LOS, and also that due to projection effects (i.e. all the dark matter between observer and source). We find an irreducible scatter (intrinsic) of 10-14%, a scatter around a 30% of the intrinsic one due to correlated structure, and a scatter around 40-70% of the intrinsic one due to projection effects. The size of our halo sample allows us to improve the characterization of the cosmic noise, of great importance for present and future surveys.

 doi:10.20944/preprints202303.0387.v1

Abstract

Esta tesis hace uso de una de las metodologías más prometedoras para el estudio de la distribución de materia oscura. Basándonos en la simulacion cosmológica MICE, y en los mapas de convergencia creados por Fosalba et al. [58], realizamos la calibración de la masa de los halos incluidos en dicha simulación hasta z=1. La calibración de masa y el análisis de los perfiles de densidad se ha realizado sobre halos en el lightcone, que consiste en ∼200 capas esféricas concéntricas. Este esquema, apodado *Onion Universe*, imita la estructura de survey fotométrico de galaxias, de ahí nuestro interés. Cada capa ha sido posteriormente proyectada en un mapa HEALPIX de densidad con distintas resoluciones en masa. La identificación de los halos en nuestra simulación ha sido realizada por Crocce et al. [37] mediante el algoritmo denominado *friends-of-friends* (FOF), que calcula todas las partículas vecinas de una partícula dada dentro de una distancia fija denominada *linking length* (en nuestro caso el linking length ha sido fijado a b=0.2, es decir, 0.2 veces la separación promedio entre partículas).El algoritmo se aplica después a cada una de las partículas vecinas de forma recursiva, hasta que ya no se encuentran más vecinas, completando así la definición de halo como una distribución espacial de partículas cuyo contorno es aproximadamente una curva de isodensidad. Diferentes estudios han demostrado que la abundancia de los halos así encontrados es universal. La recuperación de la masa de halos mediante el efecto lente debil es dependiente de la asunción de un modelo para el perfil de densidad. Esto es, hoy por hoy, inevitable, y por eso está sujeto a continuos estudios y debates. Simulaciones y estudios observacionales buscan patrones y tendencias comunes, y ya han logrado elaborar un extenso catálogo de errores sistemáticos asociados a la medida de este efecto. Pero es precisamente el gran número de problemas asociados a esta forma de estimar las masas de los cúmulos de galaxias, lo que hace a los estudios detallados de los perfiles de densidad indispensables a la hora de estimar el sesgo y la dispersión de las medidas. Con este fin analizamos los perfiles de densidad promedio de todos los halos con masas entre 5×10^{13} y 3.751×10^{14} $h^{-1}M_{\odot}$, dividiéndolos en cuatro rangos de masa y tres de redshift. A través de este análisis abordamos dos grandes problemas: la relativamente baja resolución en masa de la simulación (m_p=2.34×10^{11} $h^{-1}M_{\odot}$) y el valor relativamente alto del *softening length* (l_{soft}=50 h^{-1} Kpc), y lo hacemos mediante un procedimiento en dos pasos. En primer lugar simulamos

 doi:10.20944/preprints202303.0387.v1

perfiles de densidad NFW analíticos (con diferentes resoluciones en masa) con los siguientes valores: los radios del virial de los halos MICE y las concentraciones teóricas de acuerdo a la relación masa-concentración que se muestra en Oguri & Hamana [130]. En segundo lugar modelizarmos el efecto producido el *softening length* mediante el uso de un filtro gaussiano que suaviza el perfil de densidad en la parte interior del halo. Los resultados muestran que los halos MICE son, en promedio, halos NFW. Los valores del radio del virial que arroja el ajuste son muy parecidos a los valores promedio de las muestras correspondientes; sin embargo, las concentraciones NFW que estima el ajuste son un 50% menores que los valores esperados. Es posible explicar parte de esta diferencia diferenciando aquellos halos que están en equilibrio, y encontramos que, dependiendo del grado de equilibrio del halo, la mejora en la estimación de la concentración puede ser incluso de un 30%. Encontramos también que los halos NFW analíticos simulados con la resolución en masa de los halos MICE tienen en promedio una concentración un 40% menor de lo esperado en el caso de los perfiles tridimensionales, y un 25% menor en el caso de los perfiles proyectados. El perfil suavizado mediante el filtro gaussiano resulta ser una buena aproximación a nuestros perfiles proyectados. Analizamos también la morfología de los halos, estudiando su triaxialidad a una distancia R_{200} y calculando su orientación con respecto a la línea de vision. Los halos MICE son preferentemente prolatos, como cabría esperar de una simulación ΛCDM (Shaw et al. [159]), y el porcentaje de prolatos crece con la masa. La resolución en masa no es, sin embargo, suficiente como para obtener resultados concluyentes en cuanto a la geometría, pero nos permite discernir una tendencia a nivel estadístico y, posteriormente, hacer una estimación de cómo afecta la forma y la orientación del halo a las masas recuperadas con Weak Lensing. Para finalizar, utilizamos los mapas de convergencia para estudiar la dispersión en la recuperación de las masas de los halos. Determinamos la dispersión intrínseca asumiendo el perfil suavizado NFW como el modelo verdadero para nuestros halos, y construyendo dos nuevos mapas de convergencia a partir de distintos cortes en masa. Estimamos también la dispersión debida a la estrucutra correlacionada mediante el estudio del ángulo que forma el eje mayor del halo con la línea de visión, y a través también de la variabilidad de los perfiles de densidad dentro de una muestra. El tamaño de nuestra muestra nos permite una mejor caracterización del *cosmic noise*, de gran importancia para observaciones presentes y futuras.

 doi:10.20944/preprints202303.0387.v1

Una de las actuales limitaciones que tiene el estudio del efecto lente gravitacional débil en simulaciones es que se realizan generalmente en una pequeña porción del cielo, perdiendo así parte de la información del shear debido a estructuras adyacentes. Si queremos deshacernos de este error sistemático se hace por tanto necesario el uso de mapas de shear (o cualquier otro observable debido al efecto lente) de todo el cielo. Los mapas de shear y flexion de todo el cielo se han construido a partir de los mapas de convergencia, y permiten la visualización conjunta de convergencia y shear/flexion. La resolución en masa de la simulación MICE permite que los mapas de shear creados tengan una gran utilidad en el estudio del efecto lente débil.

 doi:10.20944/preprints202303.0387.v1

 doi:10.20944/preprints202303.0387.v1

ACKNOWLEDGEMENTS

First, I would like to thank my supervisor, Enrique Gaztañaga, for his support throughout the whole of my PhD. I greatly benefited from his advice and skillful guidance over the past four years. Thanks also to my co-supervisor, Pablo Fosalba, for his valuable help and dedication throughout this project.

Special thanks to my collaborators in the Cosmology Group at ICE, and also to Bhuvnesh Jain and the Department of Physics and Astronomy at University of Pennsylvania for their hospitality.

 doi:10.20944/preprints202303.0387.v1

Contents

 doi:10.20944/preprints202303.0387.v1

Chapter 1

Introduction

"*Oh let the sun beat down upon my face*

Stars to fill my dreams

I am a traveler of both time and space

To be where I have been"

Kashmir - Led Zeppelin

We are still fascinated with light. Artists of every epoch have strived for enlightenment and dexterity to capture beauty and movement. The starry nights of Van Gogh, or Duchamp's nudes descending the staircase are just a few examples of this fascination. But as we try to bring art out of nature, nature finds its own ways to show itself as an artistic and subtle conundrum; and in that keenness to appreciate light, physics could not be absent.

Einstein conceived his special and general relativity theories around the concept of light, and reduced gravitation to a geometrical abstraction, thus allowing us to explore the Universe in terms of relative time differences and properties of space. The notion of gravitational lens is a direct consequence of this vision, and although Sir Arthur Eddington referred to it stating that "*one thing at least is certain, light has weight*", the key to understanding the effect falls mainly on the word 'lens', since a change in the path of light is what we observe. Being light the most important source of information for astrophysicists and cosmologists, a phenomenon connecting

Preprints (www.preprints.org) | NOT PEER-REVIEWED | Posted: 22 March 2023 doi:10.20944/preprints202303.0387.v1

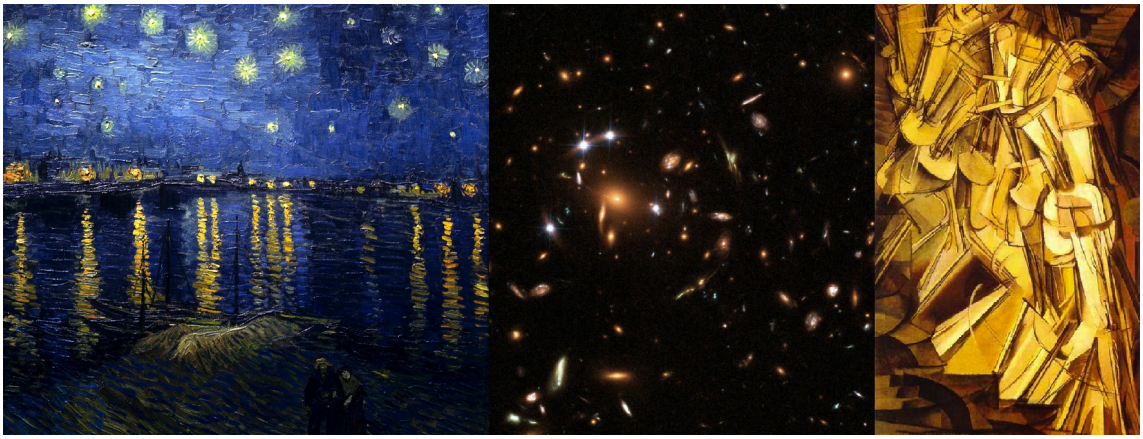

Figure 1.1: From left to right: Van Gogh's "Starry night over the Rhone", Gravitational lens SDSS J1004+4112 (Hubble telescope, NASA), Duchamp's "Nude descending a staircase No. 2". Through the gravitational lensing effect, as through paint, we are allowed to observe multiple facets and different instants of one reality embedded in a two-dimensional surface.

its trajectory to a mass/energy distribution was destined to become a major tool in the study of the Universe; even more so considering that the effect is insensitive to any interaction other than gravitation.

Nonetheless, nothing is as simple as it might seem. Mass distributions seldom exhibit a perfectly spherical or symmetrical structure, thus making the characterization of the lens more difficult; and this is just one among many other issues: dark matter and baryon distribution, interactions and dynamics; relative distance and position between lightsource, lens and observer; instrumental precision, ... Cosmologists have thus become a sort of art critics trying to decipher the laws of nature under the brushstrokes of the most formidable canvas.

In order to study the nature of any reality the first step is always the same: give a name to it. In our case, Universe is the name, and cosmology the rational effort to understand and reach a consensus on that vast concept. In the last 15 years science and technology have enabled the fast development of observational tools from which we have been able to extract a lot of scientific information about the nature of the Cosmos.

The cosmological standard model is based on independent probes which, combined, converge towards similar values of different parameters, and is therefore dubbed the 'Concordance Model'. This concurrence is understood as a smoking gun for a lasting theory of cosmology, and its

Preprints (www.preprints.org) | NOT PEER-REVIEWED | Posted: 22 March 2023 doi:10.20944/preprints202303.0387.v1

accuracy will hopefully be improved by next generation surveys (Euclid, WFXT, SKA, DESI, HSC, WFIRST, LSST, HETDEX ...). The work on dark matter and dark energy constitutes most of the research effort in present cosmology, since they are acknowledged as the central parametric ingredients in the understanding of the accelerating expansion ([6], [184]) and the evolution of structure [39, 138, 141, 20]. The basic unit, object of this study, is the dark matter halo. Quantum fluctuations in the very early Universe resulted in mass density perturbations, which growing linearly due to gravitational interaction finally reached a critical overdensity and collapsed non-linearly to form a halo [36]. A subsequent hierarchical process, consisting of successive mergers of larger and larger halos, eventually led to the present mass density field. The central motivation behind the definition and characterization of these dark matter blocks called halos, is giving sense to the distribution of the visible Universe: stars, galaxies, groups and clusters; hence the interest in establishing a universal pattern for them that would enable us to systemize the analysis of the large scale structure [28, 33, 63, 64, 66, 98]. Typically, halos are modeled using the two-parametric NFW density profile [127], a fairly standard broken power law model, although some works [128, 166, 41, 65, 124] suggest that the Einasto profile [49] may be a better fit for the dark matter halo profiles.

Nevertheless, cosmology, in its commitment to standardize Universe processes, must face the issue of uniqueness. Confronting the singular always makes Science feel like wearing an ill-fitting suit, like remembering that small print of the contract. Some disciplines easily allow to get rid of these unpleasant peculiarities and outliers, but cosmology cannot afford to discard the subject of its study, the one and only Universe we have access to. This is the main reason behind the increasing use of simulations in cosmology [11, 60, 76, 102, 113, 165]; an effort to improve the meaningfulness of the expression 'cosmological realizations' and perform representative statistical analysis on them. Observations point to an underlying mass distribution of halos dominated by dark matter, a collisionless type of (yet unseen) matter. Gravitational lensing by clusters of galaxies and bigger structures reflects this preponderance of dark matter over baryonic matter regarding the evolution of large and medium scale structure, with collisional matter only of great importance at galaxy scale; but this is beyond the scope of this work. Different codes and techniques for collisionless cosmological simulations converge on similar descriptions of gravitational

 doi:10.20944/preprints202303.0387.v1

interaction, thus suggesting a good modelling, but reaching the same level of confidence with baryonic processes remains a challenge.

Considering the cosmological and computational paradigms, formation and evolution of the Large Scale Structure of the Universe would be, in Khun's words, a "*legitimate problem*", being N-body simulations and the gravitational lensing effect "*legitimate methods*" [105]. This thesis is thus restricted to the leading cosmological model, the flat Cold Dark Matter model with a cosmological constant (ΛCDM), and deliberately endowed with the spirit of Francis Bacon's aphorism: "*Truth emerges more readily from error than from confusion*".

The theoretical landscape inhabited by the gravitational lensing effect is a privileged one, because, despite being part of a greater theoretical construct more subject to speculations, it is enriched by observations and an industrious methodological and technological improvement. Moreover, as this effect buries its roots in the fertile soil of Einstein's General Relativity, in this work we will assume the motion of cosmological structures and the trajectories of particles to be well described by this theory, and consequently by the local and global geometry in the scales of our interest, weak and medium lensing regime.

The ΛCDM model closely matches observations, thus being the better choice for the purpose of this study: characterizing the masses of dark matter halos making use of simulated all-sky convergence (κ) maps [58]. There are some conflicts between ΛCDM and observations, one of them regarding the halo density profiles, since the observed concentrations are higher than those predicted by theory [24, 25] . We will address a similar issue related to the recovery of the theoretical concentrations from the modeling of the density profiles of simulated halos. In order to do this we account for different possible error sources: mass resolution of the simulation, the effect of softening length on the innermost region of the density profiles, and the definition of the halo center. In this regard, we simulate a population of pure analytical NFW halos with the same characteristics as the population of one octant of the simulation. Comparison of both populations improves the understanding of the structure of simulated halos and enables us to differentiate between the sources of errors during the mass calibration.

Most of the literature related to the study of halo properties makes use of high resolution simulations and tends to focus on isolated and virialized halos [28, 66, 127, 128, 144], but our

Preprints (www.preprints.org) | NOT PEER-REVIEWED | Posted: 22 March 2023 doi:10.20944/preprints202303.0387.v1

approach consists in working with a low-mass resolution simulation (particle mass M=2.34×10^{11} $M_{\odot}$/h) and consider all halos, regardless their degree of virialization and substructure. This methodology presents some disadvantages, like an underestimation of the number of subhalos or flatter cusps, but also offers great statistics (from all-sky lightcone simulations), and allows us to better average out the effects of large-scale structure on halo profiles, and improve the accuracy of theoretical density profiles for the external regions.

We conceive structure formation as a hierarchical process where matter distribution evolves in a definite direction. Every hierarchical configuration pursues the simplification of the conceptual framework, and behind that idea lies one no less significant for those who deal with simulations: reduction of computational worload and amount of data. Thus, we are interested in performing not only a mathematical and statistical modelling, but also a scalable modelling, i.e. do research with models of data instead of dealing with time-consuming large data sets.

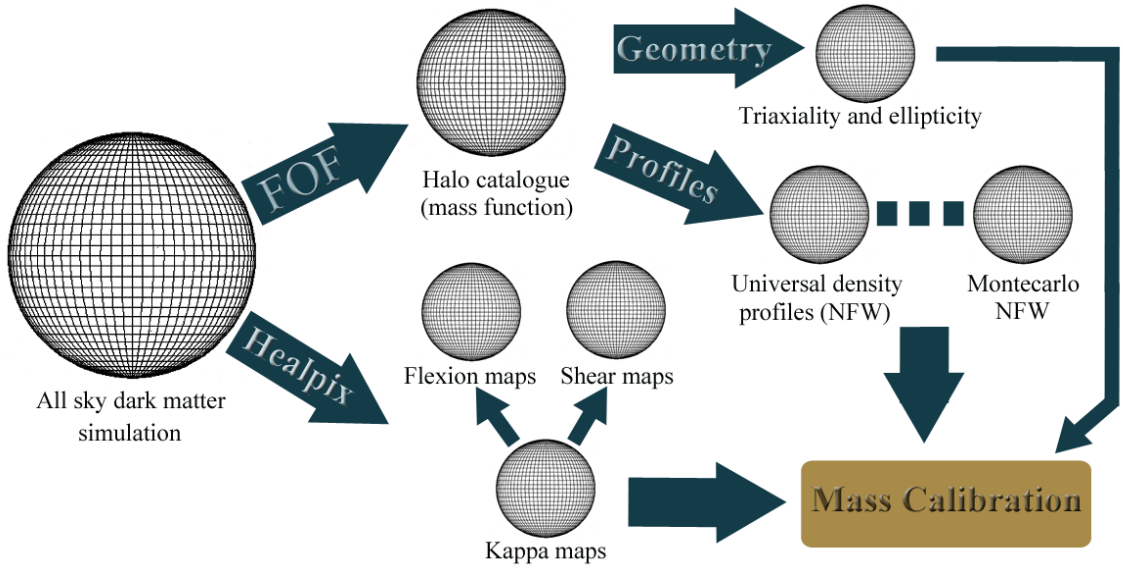

Figure 1.2: Diagram of the thesis content. Here are reflected all the research lines and their outputs. Our work starts from the previous work done by [58](MICE simulations) and [37] (FOF analysis and mass function). The size of the different spheres try to reflect, roughly, how data scales for the different probes compared with the initial dark matter simulation data set.

Although much of this work focuses on the mass calibration of dark matter halos from N-body simulations, other tools have been implemented to probe both large and small scales: all-sky

 doi:10.20944/preprints202303.0387.v1

shear (γ) and flexion maps ($\mathcal{F}$ and $\mathcal{G}$), and magnification maps (based on the model described in Lima et al. [114]). All-sky shear and flexion maps can be generated up to redshift z=50, using the all-sky shells from Fosalba et al. [58]. We have built both shear and flexion maps as Healpix maps [67], combining in the same map convergence and shear, or convergence and first flexion $\mathcal{F}$ (or second flexion $\mathcal{G}$), thus permitting the joint visualization of the projected surface density and the spin fields. The scope of these maps covers tomographic analysis, mass calibration, mock galaxy catalogs and lensing maps.

The next chapter includes an overview of the simulations and a detailed description of the halo density profiles, including softening and mass resolution modeling. Chapter 3 introduces the statistical analysis of MICE dark matter halos geometry. Chapter 4 presents the techniques to generate all-sky flexion and shear maps, as well as their validation. Chapter 5 puts forward a new mass calibration procedure for different redshifts, and addresses the effects of correlated and uncorrelated structure on the mass recovery. The final chapter provides a summary and a discussion of the results of this work.

1.1 The cosmological context

1.1.1 The concordance model

The description of the Universe currently favoured by observations is known as ΛCDM, where Λ represents *dark energy* and CDM stands for *cold dark matter*. This model attempts to simultaneously explain the matter structure observed throughout the Universe, the temperature pattern observed in the cosmic microwave background (CMB), and the accelerated expansion of the Universe indicated by e.g. supernova studies. In the process ΛCDM is able to quantify the size of the mass-energy density constituents. Surprisingly, the known components of the Standard Model of Particle Physics, such as electrons, protons and neutrons, compose only a minor part — about 5% — while the majority of the matter constituents appears to be something different: dark matter. Even more surprising is that the majority of the energy density appears to be composed of the enigmatic dark energy, which makes up some 70% of the total. Dark matter is necessary for structure formation as it adds gravity which holds large structures such

 doi:10.20944/preprints202303.0387.v1

as clusters of galaxies together. Though we have not yet determined exactly what dark matter is, there are some indications of what it could possibly be. Traditionally there are three categories of dark matter: cold, warm and hot. These labels refer to how fast the particles were able to move at the very beginning of the Universe. Cold dark matter became non-relativistic early on, while hot dark matter stayed relativistic until shortly before the epoch known as recombination during which atoms formed. Since we know the temperature of the Universe at that time, this also sets limits on the masses of such particles, with hot dark matter being much lighter than cold dark matter. The most commonly known candidate for a hot dark matter particle is the neutrino. Neutrinos are very light and conform to the constraint that dark matter has to be only *weakly interacting*, making them hard to detect. A model dominated by hot dark matter is inconsistent with hierarchical galaxy formation though, so this alternative has effectively been ruled out via observations. Warm dark matter is then more feasible, and behaves similarly to cold dark matter on large scales though there may be differences on small scales. The most commonly considered candidate warm dark matter particle is the sterile neutrino which is more massive than its hot dark matter counterpart. However, since these sterile neutrinos are not well motivated in particle physics, the current standard model of cosmology prefers cold dark matter. There is now a profusion of candidates for what cold dark matter could be since there is no real upper limit to the mass allowed.

ΛCDM has gained great support due to its ability to successfully reproduce a universe very similar to ours. Among the successes of the model, the results from the COBE (Mather [121]; Gulkis et al. [70]; Mather et al. [122]) and its successor the WMAP (Bennett et al. [19]; Spergel et al. [162]; Jarosik et al. [92]) stand out. The two space missions have together accumulated 15 years' worth of CMB data, producing exceedingly accurate measurements of the echoes of the Big Bang via the CMB angular power spectrum, shown in Fig. 1.3.

1.1.2 Cosmology probes

There are several ways to test and constrain our cosmology models and often each such probe is more sensitive to some parameters than others. Combining several datasets will therefore result in much tighter constraints on cosmology than each on its own. The CMB power spectrum

Preprints (www.preprints.org) | NOT PEER-REVIEWED | Posted: 22 March 2023 doi:10.20944/preprints202303.0387.v1

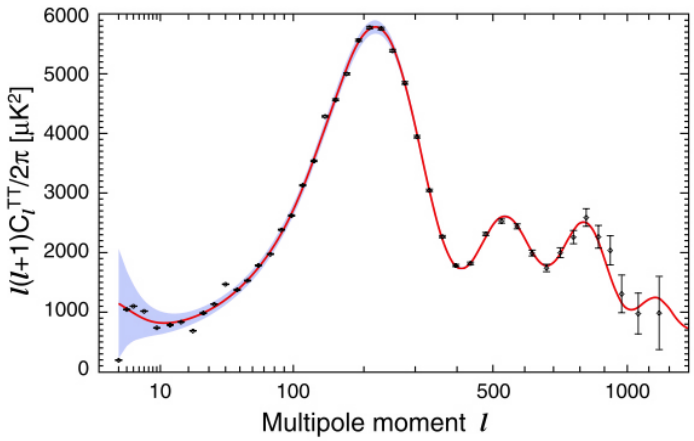

Figure 1.3: CMB angular power spectrum from the 7-year WMAP data release. The red curve represents the best-fit ΛCDM model and the grey band shows the cosmic variance expected for that model. Figure originally published in Larson et al. [106].

is sensitive in shape, peak location and relative peak heights to the underlying cosmology (see Fig. 1.3, and e.g. Hu & White [89]; Peacock [136]). The location of the first acoustic peak is related to the curvature of the Universe; we now know that the Universe is essentially flat. Furthermore, the location of each peak relative to the previous one is an indicator of the nature of the primordial density perturbations. The peak locations measured by WMAP provide strong support for dark energy. Regarding amplitudes, the amplitude of the first peak compared to the second one (or odd peaks versus even ones) holds information on the baryon density. The more baryons present, the more relatively suppressed the second peak is. Finally, by determining the height of the third peak we determine the ratio of dark matter density to radiation density, and since we know the radiation density from other measurements it gives us the dark matter density in the Universe. However, different parameters may affect the power spectrum in a similar way, which means that we cannot tell whether the shift in one direction is due to the variation of one parameter or another. This is what is known as a *parameter degeneracy*. As an example, the Ω_m and H_0 parameters are degenerate which is why the spread in allowed values for Ω_m is so large (see Fig. 1.4). To break such a degeneracy, independent measurements of H_0 are needed and these measurements may be provided by e.g. studies of supernovae (SNe).

Historically, SNe provided one of the first indications of an accelerated expansion (Riess et al.

 doi:10.20944/preprints202303.0387.v1

[147]; Perlmutter et al. [139]). SNe is a collective name for all types of stars exploding during, or at the end of, their life cycle. There are several mechanisms that can cause such an explosion, but for cosmological applications one mechanism is of particular interest: that which leads to a Type Ia SN. This species inevitably results in a characteristic light curve, i.e. how the luminosity resulting from the explosion decays with time is identical for all SNe of a given brightness. By precisely measuring such a light curve and comparing it to the observed brightness, the distance to the SN can be accurately inferred. The redshift of the SN host galaxy is then used to constrain the relationship between distance and redshift which in turn constrains Ω_m and Ω_Λ, breaking the degeneracy in the CMB power spectrum as described above (again, see Fig. 1.4).

Another probe which allows the breaking of the above degeneracy is the study of large-scale structure (LSS). The way galaxies are distributed throughout the observable Universe is a measure of how matter is distributed and how it clusters, something which is sensitive to Ω_m. Galaxies have therefore been mapped in redshift space through spectroscopic surveys such as the Two-Degree-Field Galaxy Redshift Survey (2dFGRS; see e.g. Cole et al. [34], for results from the final data set) and the SDSS (see e.g. Tegmark et al. [169]). However, because we do not know exactly how the locations of galaxies correspond to the location of the underlying dark matter, interpreting the results in terms of Ω_m is difficult. It requires a description of how well galaxies trace the total mass distribution, and this description is quantified via the galaxy bias. The choice of bias constitutes an uncertainty in LSS measurements and needs to be further investigated. In general though, we see a pattern of clustered matter and filaments connecting the clusters, and between the filaments we see voids where there is no matter. This pattern is commonly known as the Cosmic Web and the voids are a signature of sound waves created by cosmological matter perturbations in the early Universe, identified as baryon acoustic oscillations (BAO). The imprint of BAO on the matter power spectrum provides a characteristic length scale, and measuring it constrains the distance-redshift relation giving a measure of Ω_m (e.g. Eisenstein et al. [50]).

A different approach to studying cosmology is to create a new cosmos using the physical laws and properties we are aware of. This can be done using N-body simulations which make use of (dark) matter particles, place them according to some initial conditions and let them

Preprints (www.preprints.org) | NOT PEER-REVIEWED | Posted: 22 March 2023 doi:10.20944/preprints202303.0387.v1

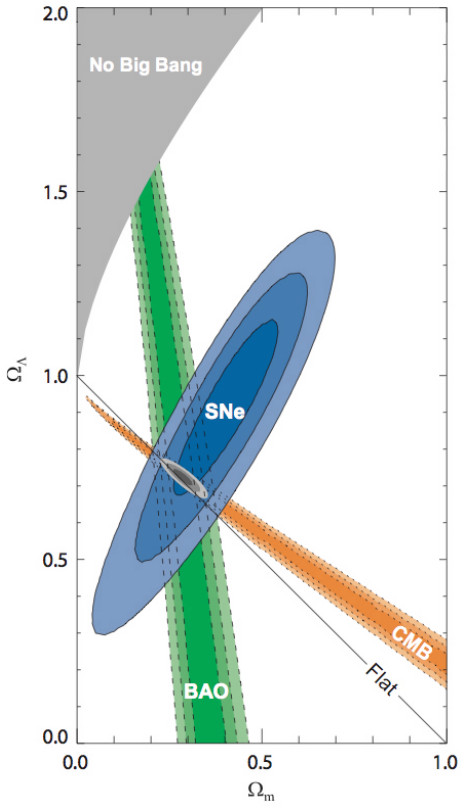

Figure 1.4: Combined probes to constrain cosmology. The datasets shown in this figure are the results from the cos- mic microwave background (CMB; Dunkley et al. [48]), baryon acoustic oscillations (BAO; Eisenstein et al. [50]) and supernovae (SNe; Kowalski et al. [103]). Though each dataset is degenerate in some sense, combining them all gives tight constraints on Ω_m and Ω_Λ (contours at intersection). Figure originally published in Kowalski et al. [103].

interact over the life-span of the Universe. Comparing these simulations at different points in redshift to real observations at the same redshifts tells us how well we have understood the underlying physical processes. In this work we mainly use the MICE Simulation (Fosalba et al. [58]). Shown in Fig. 1.5 are three pictures from this dark matter only simulation at redshift z=0.95 corresponding to three different zoom levels. One application of N-body simulations is, for instance, that the density profile of a simulated cluster may be modelled and then compared to an equivalent observed cluster studied using gravitational lensing, a technique with the power to map the full mass distribution, to see how well the profiles agree. Studying clusters at different redshifts allows us to investigate the evolution of structure as well. A significant limitation of most N-body simulations is, however, that they use only dark matter particles and disregard the

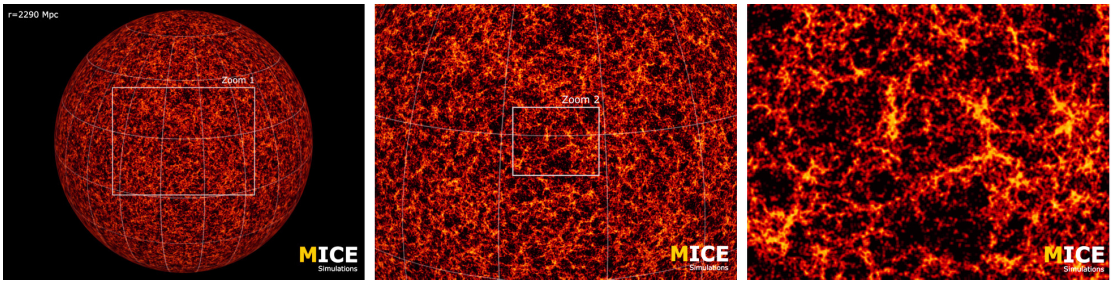

Figure 1.5: MICE Simulation slice at z=0.95. Each panel corresponds to a different scale.

influence of baryons. The reason for this is partly that baryons are expected to follow the general distribution of dark matter and partly that the processes involved are less well understood. The comparison with lensing observations, which are sensitive to all mass, may therefore be somewhat restricted but may also inform us of how the inclusion of baryons affects the dark matter only Universe.

1.2 Weak Lensing

We will here review the fundamentals of weak gravitational lensing, though for a thorough treatment we refer the reader to Bartelmann & Schneider [13] and Schneider [154].Weak gravitational lensing detection is already a reality in the scope of cosmological probes. A relatively young (first detections date back to 1990 [175] and 1994 [23],[52]) and versatile tool that attests to the improvement in observational Cosmology, and which promising development will hopefully lead us to a better understanding of large scale structure, dark matter and dark energy.

1.2.1 Convergence and Shear

We can write the mapping between source and lens plane as

$$\beta_i \simeq A_{ij}\, \theta_j \ , \tag{1.1}$$

Preprints (www.preprints.org) | NOT PEER-REVIEWED | Posted: 22 March 2023 doi:10.20944/preprints202303.0387.v1

In the previous equation θ is a point within the image corresponding to the point β within the source and

$$A_{ij}\left(\boldsymbol{\theta}\right)=\frac{\partial\beta_i}{\partial\theta_j}=\delta_{ij}-\partial_i\partial_j\psi\left(\theta\right)\ , \tag{1.2}$$

where we use the shorthand $\partial_i \equiv \partial/\partial\theta_i$, and ψ is the *lensing potential*. Eq. 1.1 holds true for small source galaxies where the convergence is constant across the source image. If we rewrite eq. 1.2 we can also get an alternative description of the distortion matrix $\mathbf{A}$:

$$\mathbf{A}=\begin{pmatrix}1-\kappa-\gamma_1 & -\gamma_2\\ -\gamma_2 & 1-\kappa+\gamma_1\end{pmatrix} \tag{1.3}$$

where κ is the *convergence*, and γ_1 and γ_2 are the two components of the shear induced by the lensing potential: $\gamma=\gamma_1+i\gamma_2$. These shear components are related to the lensing potential ψ via

$$\gamma_1=\frac{1}{2}\left(\psi_{11}-\psi_{22}\right) \tag{1.4}$$

$$\gamma_2=\psi_{12} \tag{1.5}$$

where e.g. $\psi_{11}=\partial_1^2\psi$ is the second derivative of the lensing potential. Definining the complex gradient operator

$$\partial=\partial_1+i\partial_2 \tag{1.6}$$

using the same shorthand as before we can also relate the shear to convergence in a way which compactly shows that shear is the second-order gradient of the lensing potential:

$$\gamma=\partial\partial\psi \tag{1.7}$$

The effect of shear on a source image is to stretch it in one direction as illustrated in Fig. 1.6 with the direction dependent on the relative amplitudes of the γ_1 and γ_2 distortions. As is clear from Fig. 1.7, the transformation $\gamma \rightarrow$ -γ results in a 90° rotation and pure γ_2 is at 45° to pure γ_1. Generally we also assign a property known as *spin* to weak lensing distortions. A distortion type with spin s is invariant under a rotation of $\varphi = 360°/s$ =$2\pi/s$ radians. Since an

Preprints (www.preprints.org) | NOT PEER-REVIEWED | Posted: 22 March 2023 doi:10.20944/preprints202303.0387.v1

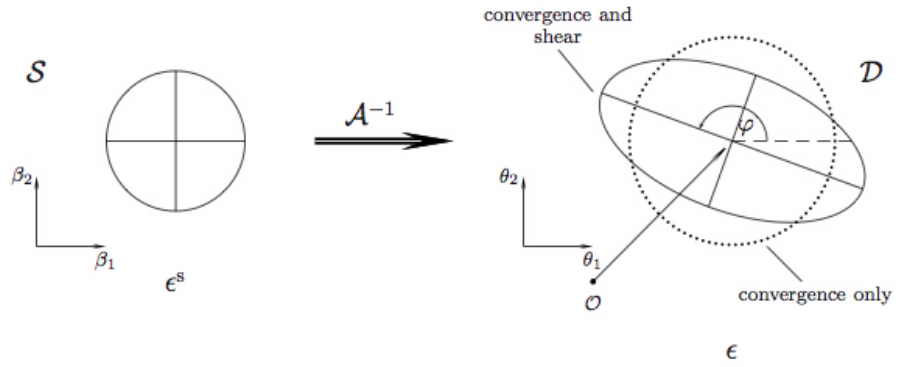

Figure 1.6: Effect of shear and convergence. On the left is the original circular source, while the lensed image is on the right. Convergence only results in an enlargement of the source image while the shear causes a stretch entailing a difference in axis ratio. The orientation of the resulting ellipse depends on the relative amplitudes of γ_1 and γ_2 as illustrated in Fig. 1.7. This figure was originally published in Schneider (2005).

ellipse rotated by 180° looks the same, shear is a *spin-2 quantity*. The lensing displacement field α is a spin-1 quantity which is also the gradient of the spin-0 lensing potential:

$$\alpha = \alpha_1 + i\alpha_2 = \partial\psi \tag{1.8}$$

We can now interpret ∂ as a *spin-raising operator*; applying it once to the lensing potential results in a spin-1 quantity, while applying it twice results in spin-2. Similarly the complex conjugate ∂^* is a *spin-lowering operator*. For instance, the convergence is related to the lensing displacement field and lensing potential via

$$\kappa = \frac{1}{2}\partial^*\alpha = \frac{1}{2}\partial^*\partial\psi \tag{1.9}$$

and is thus a spin-0 quantity.

1.2.2 Cosmic Shear

As light travels through space to reach us it is continuously deflected by the filaments and nodes of the Cosmic Web. Source galaxies are thus sheared and weakly aligned even when there are no

Preprints (www.preprints.org) | NOT PEER-REVIEWED | Posted: 22 March 2023 doi:10.20944/preprints202303.0387.v1

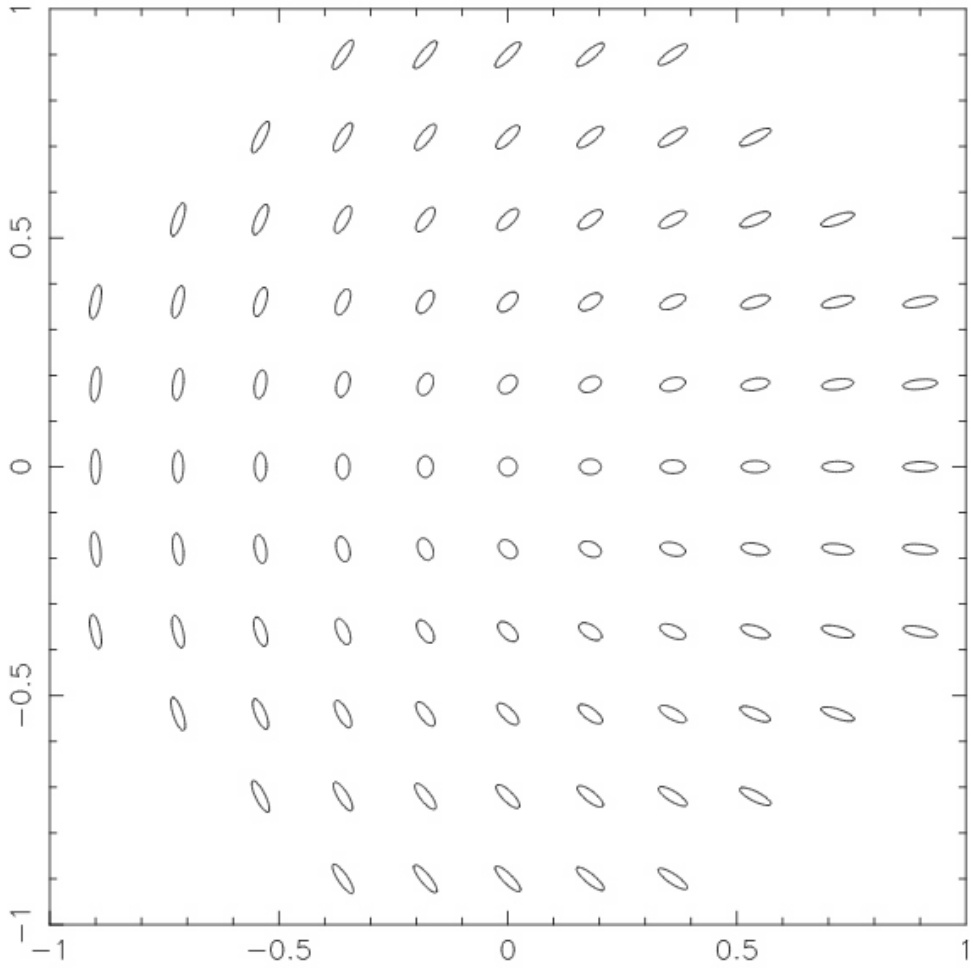

Figure 1.7: Orientation of the ellipse resulting from the relative amplitudes of γ_1 (on the x-axis) and γ_2 (on the y-axis) applied to a circular source. Figure originally published in Schneider (2005).

Preprints (www.preprints.org) | NOT PEER-REVIEWED | Posted: 22 March 2023 doi:10.20944/preprints202303.0387.v1

large structures in the way. The statistics of these distortions and alignments therefore reflect the statistics of the underlying matter distribution. This effect was detected at the turn of the millennium (Bacon et al. [10]; Kaiser et al. [100]; Van Waerbeke et al. [178]; Wittman et al. [185]). It is since being measured with ever more refined accuracy using imaging data of ever increasing area, depth and quality, and used to constrain cosmological parameters (e.g. Hoekstra et al. [85]; Brown et al. [26]; Jarvis et al. [93]; Massey et al. [120]; Van Waerbeke et al. [179]; Hoekstra et al. [84]; Semboloni et al. [157]; Benjamin et al. [18]; Schrabback et al. [155]; Fu et al. [62]; Schrabback et al. [156]; Huff et al. [91]). The correlation between shears across the sky as a function of angular scale can be used to derive the lensing power spectrum which is related to the three-dimensional matter power spectrum (e.g. Kaiser [99]; Bartelmann & Schneider [13]; Schneider [154]; Hoekstra & Jain [83]). Technically, cosmic shear cannot make use of the thin lens approximation because the deflection does not take place in a single lens plane. It turns out, however, that under the assumption that the deflection angle is small the end result is a redshift-dependent convergence κ which behaves just like in ordinary lensing (see e.g. Schneider [154]). We can therefore use ordinary shear measurements to constrain the matter power spectrum, and thus in particular the cosmological parameters Ω_m and σ_8.

Since the measurements do not rely on baryonic tracers there are no assumptions on e.g. galaxy bias necessary and this gives cosmic shear great value. Furthermore, the constraints resulting from cosmic shear intersect the constraints from the CMB in a way that reduces degeneracies adding to the benefits of such analyses. The task of observing this effect is a fairly substantial challenge however, owing to the fact that the distortions are so small. It is impossible to detect a signal on a single galaxy image since the intrinsic ellipticity of the source galaxy is in general much larger than the induced distortion. Assuming that galaxies have random intrinsic ellipticities and that they are randomly oriented on the sky we can discern the lensing signal in a statistical way though. If we average over enough sources we can reduce this shape noise and essentially reason that the mean intrinsic shape is circular. Under ideal conditions, any ellipticity observed must then be produced by lensing.

Unfortunately, such ideal conditions are also difficult to attain. A telescope will in general produce a complicated pattern which correlates galaxy ellipticities in a way that imitates a lensing

 doi:10.20944/preprints202303.0387.v1

signal. This pattern is usually referred to as the point-spread function (PSF), although other distinct processes can be involved as well (such as wind-shake of the telescope). For ground-based surveys the PSF is worsened by turbulence in the atmosphere and these seeing conditions tend to blur the galaxy images and dilute their ellipticities. Generally the PSF is corrected for by taking advantage of the fact that stars should be circular. Any ellipticity observed for stars is therefore due to the PSF and this information may be used to model the distortions. Space-based telescopes face other trials, however, such as the gradual degradation of CCD chips due to the constant bombardment of cosmic radiation.

Additional difficulties include the fact that detectors collect photons in square bins (or pixels) which places a fundamental lower limit on the size galaxy that can be reliably analysed, and the fact that there is some intrinsic alignments of galaxies due to them being affected by tidal fields during formation (e.g. Splinter et al. [163]; Faltenbacher et al. [54]; Lee & Pen [109]) or lower-redshift tidal fields affecting all higher-redshift sources (Hirata & Seljak [79]; Heymans et al. [77]). Another limiting factor is the accuracy of the software used to extract the shear signal from a given image. Great effort has been put into developing reliable software and at the moment there are many alternatives available. To take full advantage of future surveys, however, the accuracy has to be improved even more.

 doi:10.20944/preprints202303.0387.v1

Chapter 2

Modeling MICE Dark Matter Halo Profiles

"*There was the murdered corpse, in covert laid,*
And violent death in thousand shapes displayed"
The Canterbury Tales, Geoffrey Chaucer

2.1 The Simulation

The MICE simulation, developed at the Marenostrum supercomputer with the GADGET-2 code (Springel [164]), models a ΛCDM cosmology with Ω_m=0.25, Ω_Λ=0.75, Ω_b=0.044, n_S=0.95, σ_8=0.8 and h=0.7 in units of 100 kms^{-1} Mpc^{-1}. The box size is 3072 Mpc h^{-1}, thus allowing us to simulate large scale structure up to z$\sim$ 1.4 without replicating the box, and the number of particles is 2048^3, resulting in a particle mass M=$2.34\times10^{11}h^{-1}M_\odot$ and a softening length of 50 Kpc/h. The choice of this values is suitable to perform a weak lensing analisys, but it is clear that mass resolution and softening length will be a drawback for our analysis of the structure of dark matter halos.

The mass calibration and the analysis of the density profiles have been performed making use of the lighcone output, which consists of ∼200 spherical concentric shells whose particles come

 doi:10.20944/preprints202303.0387.v1

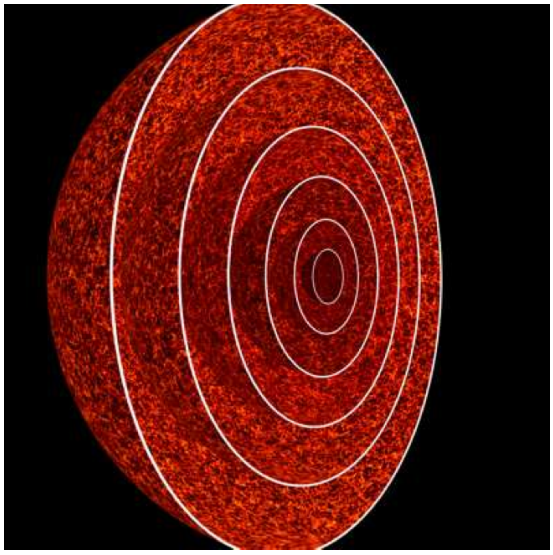

Figure 2.1: A few layers of half of the onion universe structure (from [58]).

from their corresponding comoving outputs. This scheme, dubbed Onion Universe, mimics the data structure in photometric galaxy surveys, therefore our interest. Each onion shell has been projected onto a 2D number density Healpix map with several pixel resolutions.

2.2 Halo Finding

The identification of halos in our simulation has been performed by Crocce et al. [37] using the *friends-of-friends* (FOF) algorithm [39], that determines all the neighbours of a given particle whitin a fixed distance called *linking length* (in our case the linking length has been kept fixed at b=0.2, i.e. 0.2 times the mean interparticle spacing).The algorithm is then applied to each neighbour recursively until no more neighbours are found, thus completing the definition of a halo as a spatial distribution of particles whose boundary approximately matches an iso-density contour. Different studies have shown the abundance of FOF halos to be universal at <10% level [95, 143, 75, 145, 115, 173, 37], hence our interest and the decission to use this halo finding algorithm.

A halo catalog was built for every octant of the full sky lightcone simulation, each catalog consisting of 36 files that include, among other essential data, the position of all the particles in

Preprints (www.preprints.org) | NOT PEER-REVIEWED | Posted: 22 March 2023 doi:10.20944/preprints202303.0387.v1

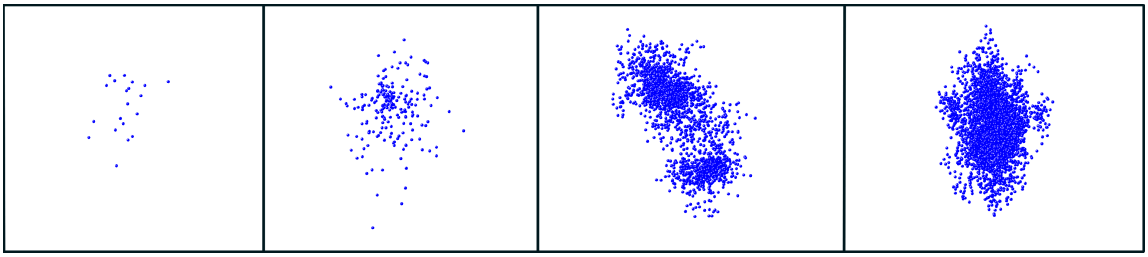

Figure 2.2: Halos with number of particles (from left to right) 20, 200, 2000 and 4000. For our purposes we are considering halos with more than $\sim$ 250 particles.

every halo. The smallest halos considered are those with 20 particles, and the halo masses range from 10^{12} to 10^{15} $h^{-1}M_{\odot}$ (20 to $\sim 10^{4}$ particles). Our density profile and weak lensing analysis will be performed just considering the highest mass ranges (5×10^{13}-5×10^{15} $h^{-1}M_{\odot}$). Still, the amount of particles inside the virial radius is quite small, a problem we have faced during the analysis of density profiles, geometrical characterization and mass calibration, and that will be explained elsewhere in this chapter.

Halo masses from the catalog are affected by a correction, for it has been shown by Warren et al. [182] that the FOF algorithm suffer from a systematic overestimation due to the statistical noise associated with the sampling of the mass density field of each halo with a finite number of particles. But we are not taking it into account for our analyses, as we will not be dealing with the FOF mass but mostly with de virial mass.

2.3 Density Profiles

Dark matter halos are of considerable scientific interest. This interest spans numerous fields including the study of the nature of dark matter, rotation curves, and the highly nonlinear regime.

The density profile of halos is a key element in the definition of the large-scale structure, and although it can be measured for individual halos, a more interesting topic is the characterization of the average density profile of a halo sample.

The first step,concerning the characterization of the halo density profiles, is the definition of the *center of the profile*. The initial halo catalog, the one resulting from the FOF analysis,

Preprints (www.preprints.org) | NOT PEER-REVIEWED | Posted: 22 March 2023 doi:10.20944/preprints202303.0387.v1

referred to the center of mass as the halo center. Nonetheless, we opted for the minimum of the potential as a better choice for the halo center, yet maintaining the initial particles of the FOF halo. In Fig. 2.3 we show three example halos illustrating the difference between the position of the center of mass and that of the particle with the lowest potential energy, even for halos in the low mass range.

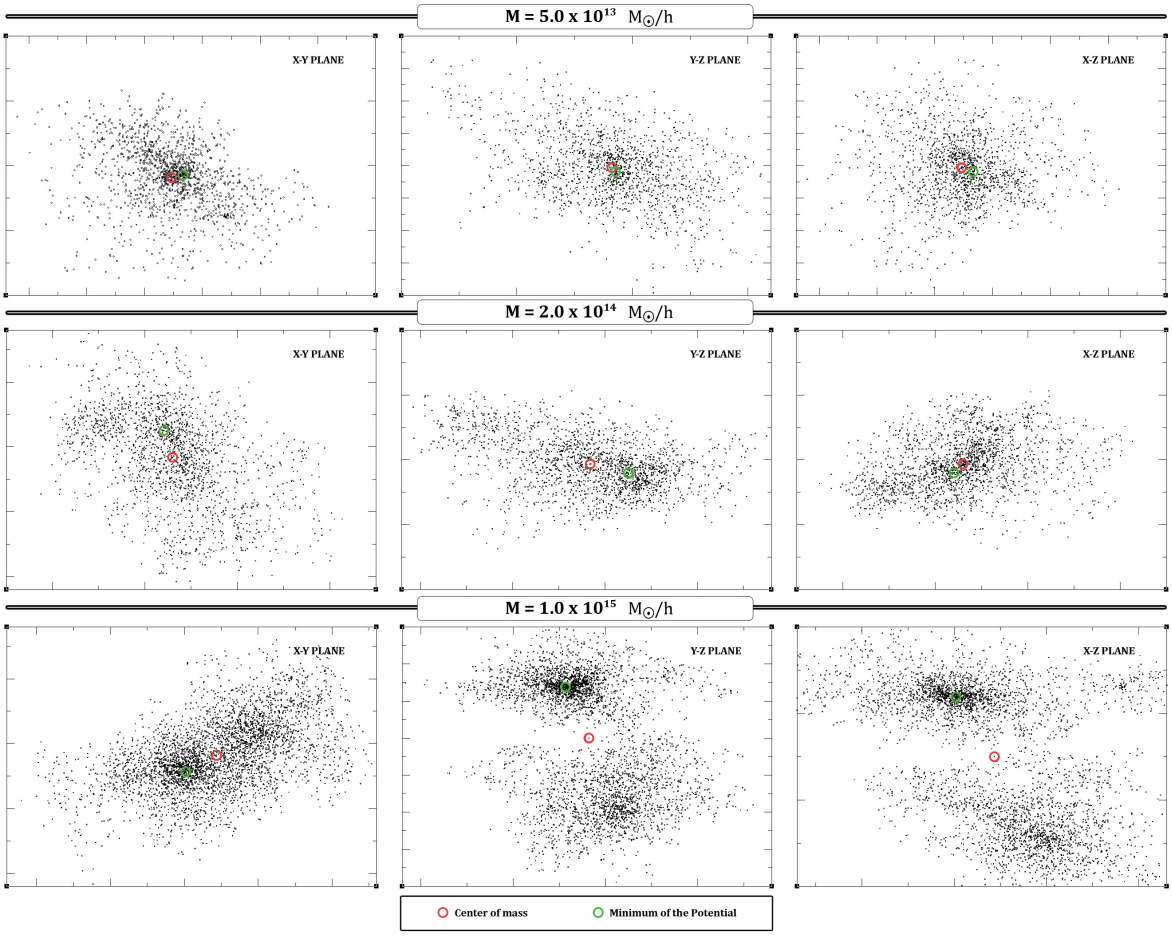

Figure 2.3: Projection planes of three example halos. Black dots are particles of the FOF halo.

Once determined the center of our halos, we partition each one into concentric shells and calculate their average density per unit volume. This translates, when it comes to plotting, into 40 radial bins, equally spaced in logarithmic scale; and each bin is assigned a radius equal to its middle value in log(r). Taking into account the softening length of the simulation (l_{soft}=50

Preprints (www.preprints.org) | NOT PEER-REVIEWED | Posted: 22 March 2023 doi:10.20944/preprints202303.0387.v1

Kpc/h), we will not trust particle positions within R_{smooth}=3*l_{soft} (0.15 Mpc/h). Hence, we will consider for our analysis the part of the profile that ranges from R_{smooth} to R_{200} (radius of a sphere of density $\Delta_{200} \equiv 200$ times the mean density of the Universe at a specific redshift). The number of bins has been thus selected in order to divide the part of the curve of our interest into ~ 20 concentric bins.

It is worth mentioning here that we find, for all the sky octants, a constant percentage of about 1% of ill-defined inner density profiles: profiles whose inner density increases with radius. These appear as a result of how FOF identifies halos, the mass resolution of the simulation, and mergers. All the halos whose density profiles are ill-defined will not be taken into account in the subsequent analysis. In Table 2.1 we summarize the ill-defined statistics for one octant of the simulation, which are representative of the rest of the octants.

Halo Mass Range ($M_\odot$/h)	**Number of ill-defined haloes**
M≤5e12	37661
5e12<M≤1e13	50875
1e13<M≤2e13	10248
2e13<M≤3e13	948
3e13<M≤4e13	196
4e13<M≤7e13	60
7e13<M≤1.225e14	8
M>1.225e14	0

Table 2.1: The number of ill-defined profiles per mass range is 99996 over a total of 10,059,692 haloes in this octant (0.994 percent). Almost 99 percent of the ill-defined profiles correspond to haloes with M<2e13.

We expect, due to the discreteness issue associated to N-body simulations and the value of our softening length, a flattened halo core, as indeed appears to be the case considering the density profiles of MICE dark matter halos. We show some examples in figure 2.4.

Preprints (www.preprints.org) | NOT PEER-REVIEWED | Posted: 22 March 2023 doi:10.20944/preprints202303.0387.v1

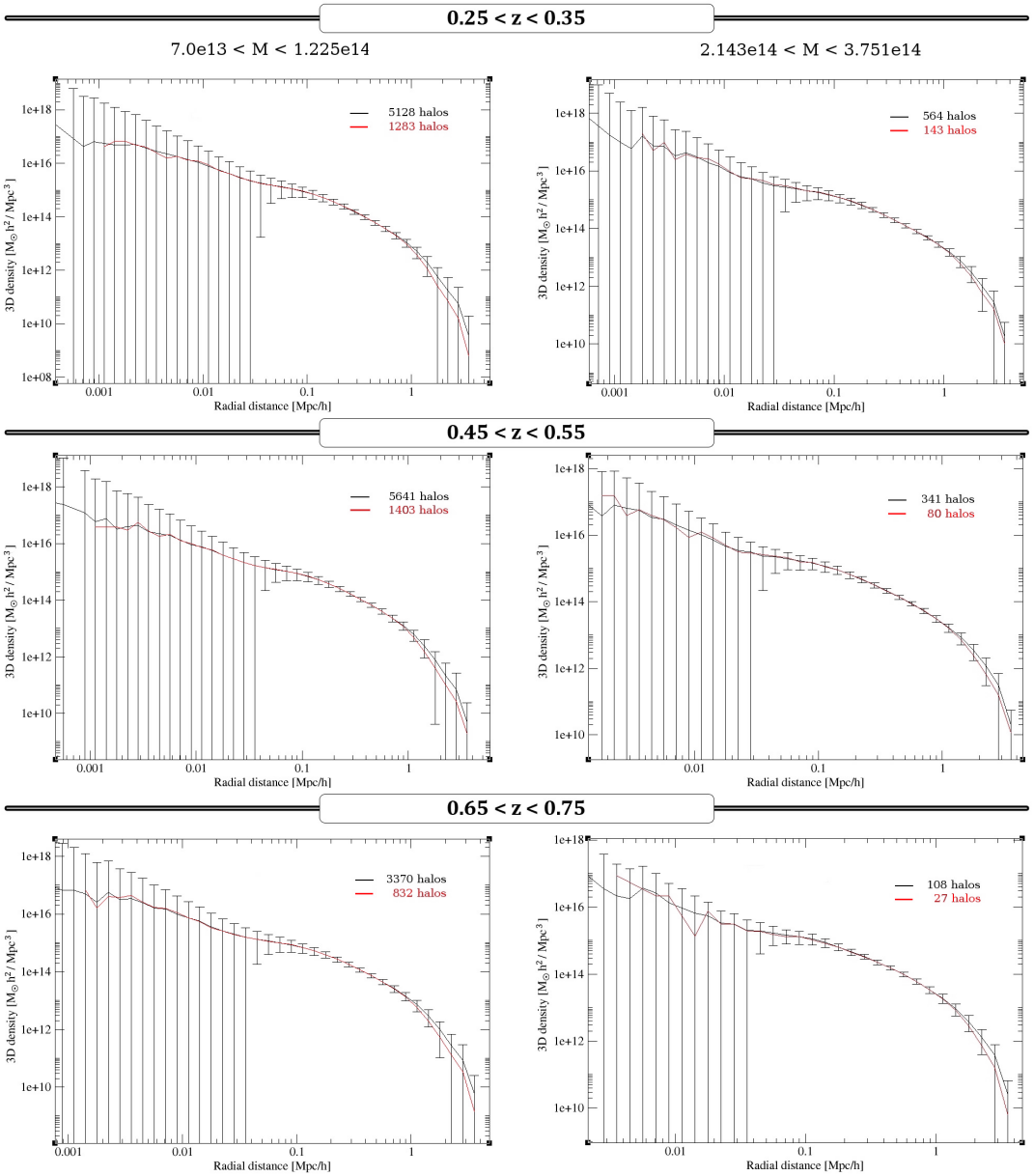

Figure 2.4: Stacked 3D density profiles of halos with masses in the ranges 7.0e13<M<1.225e14 (first column) and 2.143e14<M<3.751e14 (second column) at different redshifts. The red and black line depict the stacking of the corresponding halos in one and four octants respectively. The additional stacking just slightly modifies the outer density profile, leaving the inner part almost unaffected, but smoother. Each point of the profile has an associated Poisson error bar.

Preprints (www.preprints.org) | NOT PEER-REVIEWED | Posted: 22 March 2023 doi:10.20944/preprints202303.0387.v1

2.4 Parametrization of the profiles

We assume that the formation of haloes can be approximated by the spherical collapse, and we will characterize them by making use of a two-parameter functional form: the NFW profile

$$\rho_{NFW}\ (r) = \frac{\delta_c\ \rho_c}{(r/r_s)\,(1+r/r_s)^2}\ , \tag{2.1}$$

where

$$\delta_c = \frac{200}{3}\frac{c^3}{Ln\,(1+c) - \frac{c}{1+c}}\ , \tag{2.2}$$

r_s is the scale radius that indicates the size of the central core of the density profile (and refers also to the scale at which the logarithmic slope, $d\ln\rho/d\ln r$, is equal to -2), and ρ_c is the critical density at a specific redshift. It is convenient for our purpose to express the NFW profile in terms of the concentration c=$c_{200} = r_{200}/r_s$ and the virial mass

$$M_{200} = \frac{4\pi}{3} 200\ r_{200}^3\ \rho_c\ . \tag{2.3}$$

We are still far from a universal density profile for dark matter halos, although recent works (Baushev [15]) suggest that the central region of a halo is almost independent of the properties of the initial perturbation, while the density profile of the outer part (r>0.5 R_{vir}) is significantly more dependent on these intial conditions; but for the sake of comparison with other works, and despite we are dealing with non isolated halos, we have opted for the NFW density profile.

The relatively low mass resolution of our simulation, together with the relatively high softening length, do not define the optimal landscape for an accurate analysis of the density profiles, but our goal is precisely to study how good could be a mass calibration in an all sky simulation where the weight of statistics (number of halos per mass range) is greater than that of the resolution. In other words, our goal is not to study what is the best parametrization for the density profiles of dark matter halos, but to determine if our halos are, on average, NFW halos. Our usual subject of study will be a non-isolated halo, with a number of particles within R_{200} ranging from 150 to 4000, and at different evolution stages (redshift up to 1.0), so relaxed and unrelaxed halos will be considered. We will perform our analysis on the raw density profiles, although we

Preprints (www.preprints.org) | NOT PEER-REVIEWED | Posted: 22 March 2023 doi:10.20944/preprints202303.0387.v1

will try to characterize some of its features by making use of a smoothing kernel window and also numerical simulations of pure NFW profiles. Regarding the smoothing kernel, our purpose is not to smooth away the poisson bin noise (e.g. Reed et al. [144]), but to model the flattening of the central core of the density profiles (e.g. Smith et al. [160]).

The total number of halos is 17,224,164 (up to z=1) but most of them with $M_{200} < 4.0e13$ h^{-1} $\mathbf{M}_{\odot}$. The subsets we will be focusing on are summarized in Table 2.2

Sample	$\mathbf{M}_{200}$ $(\mathbf{M}_{\odot}/\mathbf{h})$	$\mathbf{log}_{10}$ M_{200} $(\mathbf{M}_{\odot}/\mathbf{h})$	**# Halos (0<z<1)**	f_{unrel} (0.25<z<0.35)
M1	[4.0e13,7.0e13]	[13.602,13.845]	95225	0.524
M2	[7.0e13,1.225e14]	[13.845,14.088]	33042	0.563
M3	[1.225e14,2.143e14]	[14.088,14.331]	9943	0.719
M4	[2.143e14,3.751e14]	[14.331,14,574]	2383	0.855

Table 2.2: Halo subsets and their corresponding population. For the sake of comparison with other papers we include the fraction of unrelaxed halos in redshift bin [0.25,0.35]. In this case a halo is considered relaxed if the relaxedness parameter (r) is less than 0.1. The relaxedness parameter is defined as the distance between the minimum of the potential and the centre of mass of the FOF halo divided by the virial radius.

We fit both the 3D ($\rho(r)$) and the projected density profiles ($\Sigma(R)$); the latter being generated by numerical integration of the 3d profiles along the line-of-sight. The fits to $\rho(r)$ are performed via χ^2 minimization in comparison with the theoretical profile (eq. 2.1). We build the 3D density profiles by stacking all the halos, in their respective mass ranges, at redshift intervals of Δz=0.1. Thus, for each stacked profile j, denoted $\rho_j^{(data)}(r_i)$ (for radial bins with index i) with noise variance $\sigma^2\left(\rho_j\ (r_i)\right)$, we find the NFW profile radius and concentration that minimizes

$$\chi_j^2 = \sum_i \frac{\left[\rho_j^{(data)}(r_i) - \rho_j^{(\mathrm{model})}(r_i \mid R_{200}, c_{200})\right]^2}{\sigma^2\left(\rho_j\ (r_i)\right)}. \tag{2.4}$$

For every stacked profile we try 1000 concentrations (c_{200}) between 0.01 and 20.01 in steps of

Preprints (www.preprints.org) | NOT PEER-REVIEWED | Posted: 22 March 2023 doi:10.20944/preprints202303.0387.v1

0.02, and for each of these concentrations we try 2000 radii (R_{200}) between 0.002 and 4.0 in steps of 0.002. Regarding the fit of the projected density profiles, the expression is analogous

$$\chi_j^2 = \sum_i \frac{\left[\Sigma_j^{(data)}(R_i) - \Sigma_j^{(\mathrm{model})}(R_i \mid R_{200}, c_{200})\right]^2}{\sigma^2\left(\Sigma_j\ (R_i)\right)}, \tag{2.5}$$

where R_i is now the transverse distance assigned to the center of each bin. We perform this fit for all the stacked profiles from the mass ranges in Table 2.2, but dividing the sample in 10 redshift ranges, in steps of 0.1.

Preprints (www.preprints.org) | NOT PEER-REVIEWED | Posted: 22 March 2023 doi:10.20944/preprints202303.0387.v1

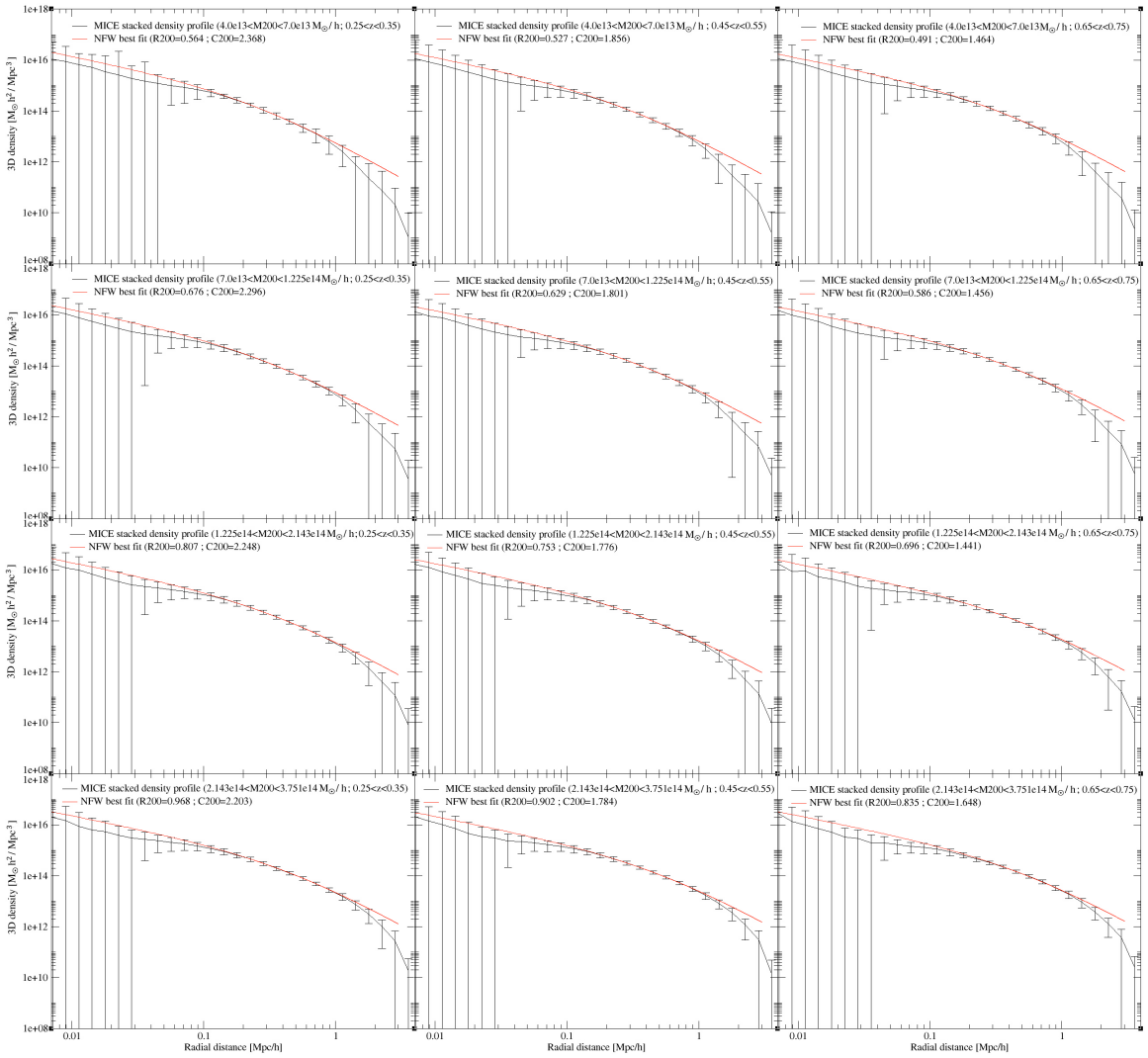

Figure 2.5: Stacked 3D density profiles from three different redshift ranges and the four mass ranges specified in Table 2.2.

In this step of the characterization of the density profiles we are only fitting the region of the profile between R_{smooth} and R_{200}.These twelve stacked profiles are a representative sample of the whole population, and a good indicator of whether our halos are, on average, NFW halos. The reduced chi-square $\left(\chi_r^2\right)$ of every fit is relatively close to 1.0 (Table 2.3), thus indicating the fit is good. But, in addition, in order to assign significance to the reduced chi-square statistic,

Preprints (www.preprints.org) | NOT PEER-REVIEWED | Posted: 22 March 2023 doi:10.20944/preprints202303.0387.v1

we have calculated the probability Q of observing a value of χ_r^2 equal to or greater than the one we found, for a random sample of N density profiles with d degrees of freedom. This probability is expressed as:

$$Q_{\chi^2,d} = \left[2^{d/2}\Gamma\left(\frac{d}{2}\right)\right]^{-1} \int_{\chi^2}^{\infty} (t)^{\frac{d}{2}-1} e^{-\frac{t}{2}} dt \tag{2.6}$$

where Γ is the generalization of the factorial function to real and complex arguments:

$$\Gamma_x = \int_0^{\infty} t^{x-1} e^{-t} dt \tag{2.7}$$

For a fitting function that is a good aproximation to the parent function, the experimental value of χ_r^2 should be close to 1.0 and the probability from eq. 2.6 should be approximately 0.5. Here we consider the NFW profile to be a good fit when χ_r^2 ranges from 1.0 to 1.5, and Q ranges from 0.4 to 0.6. In Table 2.3 we summarize the results of the different fits, along with the values of R_{200} averaged over all the halos in each mass range at each redshift bin, and the expected concentrations according to the fixed mass-concentration relation from Oguri and Hamana [130]:

$$c_{vir}\left(M_{vir}, z\right) = 7.26 \left(\frac{M_{vir}}{10^{12}\mathbf{M}_{\odot}/\mathbf{h}}\right)^{-0.086} (1+z)^{-0.71}, \tag{2.8}$$

which was derived from N-body simulations assuming best-fit cosmological parameters in the WMAP3 [116], with the redshift dependence based on the simulation result of Duffy et al. [47]. The expected concentration is, typically, the mean concentration of the sample used for the stacking (Mandelbaum et al. [119]). We have thus made use of the mean M_{200} of each sample in order to calculate the value of its corresponding expected concentration.

Preprints (www.preprints.org) | NOT PEER-REVIEWED | Posted: 22 March 2023 doi:10.20944/preprints202303.0387.v1

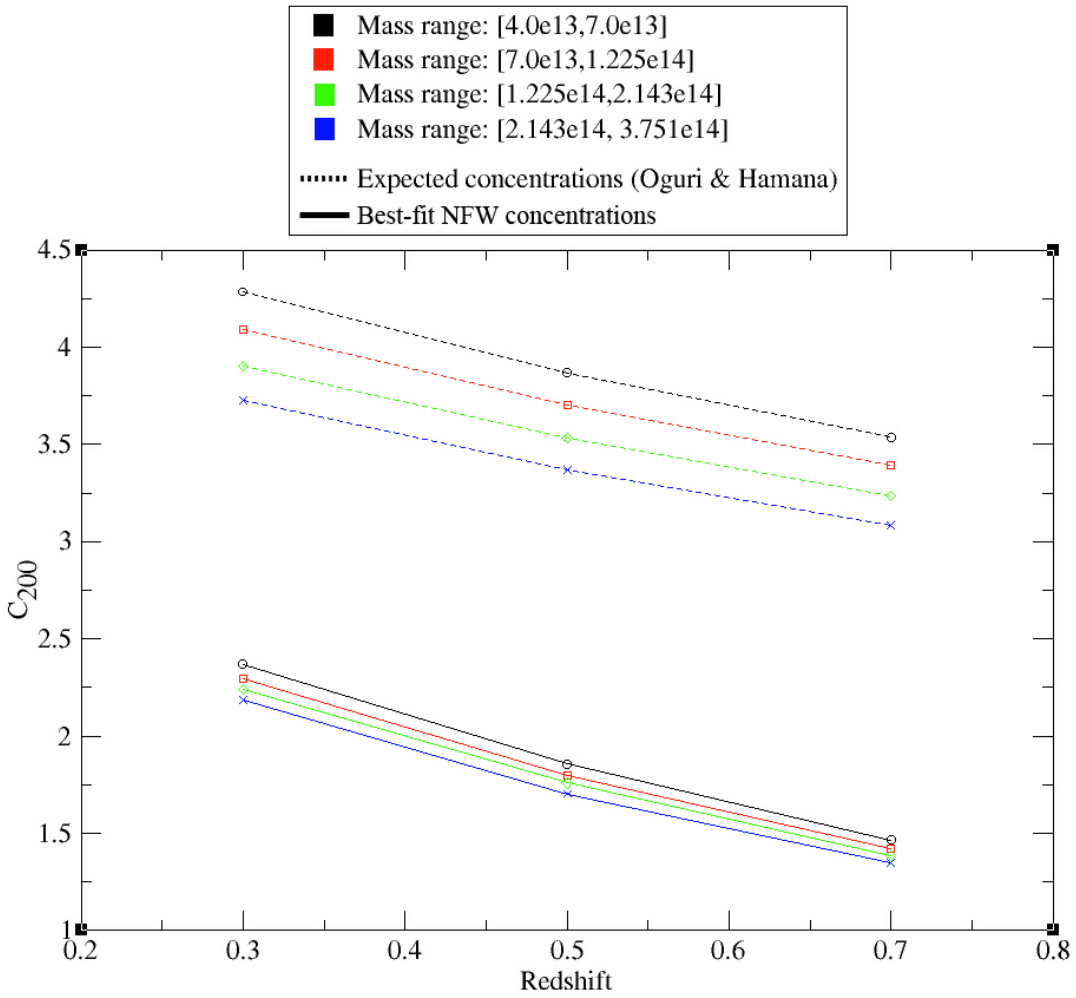

Figure 2.6: Differences between the best-fit NFW concentration values and the expected values. We find that concentrations are underestimated, and also that the best-fit NFW concentration values from one mass range are relatively much closer to those of another mass range than the expected values, which is probably due to the combination of different factors: the average degree of relaxedness, a value of the scale radius greater or lower than R_{smooth}, or the number of particles, among others.

The best-fit NFW radii are in very good agreement with the averaged values, overestimating the data by $\sim 1\%$. But, on the other hand, the best-fit NFW concentrations underestimate the expected values by $\sim 43\%$ for halos in the lowest redshift bin, by $\sim 50\%$ for those in the medium-redshift bin, and by $\sim 57\%$ for those in the highest redshift bin (Fig. 2.6). Hence, although the

Preprints (www.preprints.org) | NOT PEER-REVIEWED | Posted: 22 March 2023 doi:10.20944/preprints202303.0387.v1

fits consistently underestimate concentrations, we observe that redshift, and not the number of halos in each range or the number of particles of each halo, is the most influential factor when it comes to improve data fitting. This fact is probably due to the strong anti-correlation of concentration with relaxedness, demonstrated by Jeeson-Daniel et al. [94] and suggested also by the results shown in Fig. 2.7 , where we have redone the fits making use of various sets of relaxed halos, each one with a different degree of relaxedness. The relaxedness parameter (r) is defined as the distance between the minimum of the potential and the centre of mass of the FOF halo divided by R200.

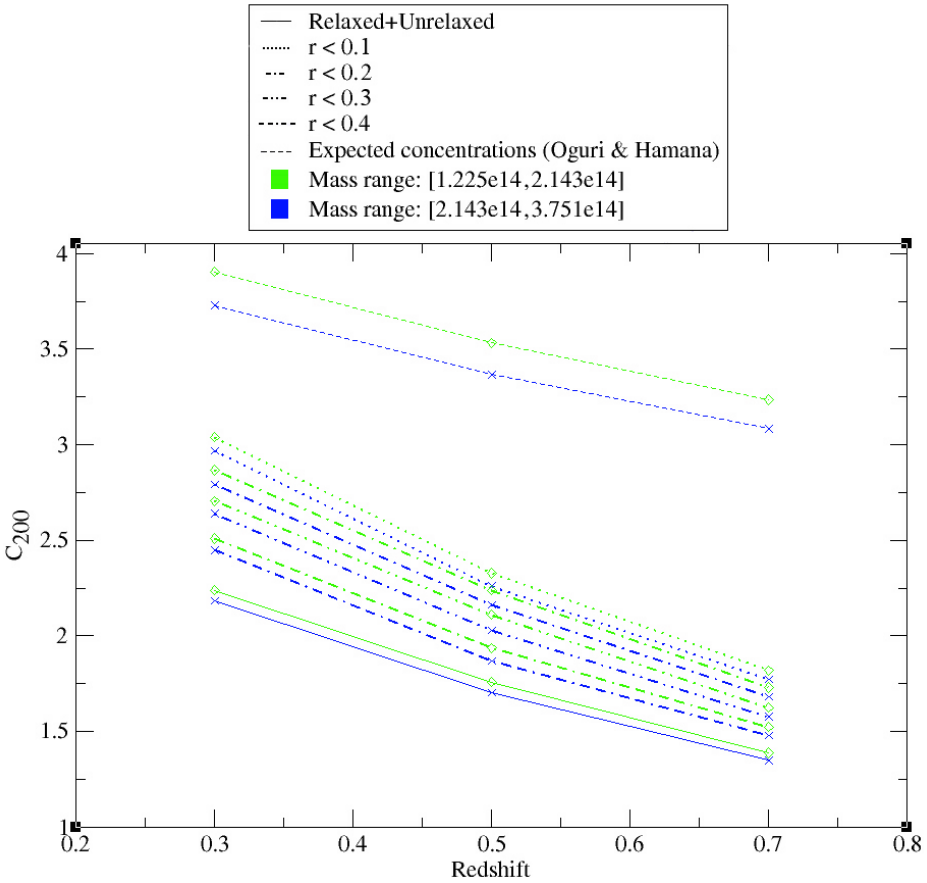

Figure 2.7: Best-fit NFW concentration values change according to the degree of relaxedness (r). Best-fit values are improved by more than 30% for the most relaxed halos (r<0.1), $\sim$ 27% in the case of r<0.2, $\sim$ 18% for r<0.3, and $\sim$ 10% for those halos with r<0.4.

It is also worth noting that for the two less massive bins the value of the scale radius is too close

Preprints (www.preprints.org) | NOT PEER-REVIEWED | Posted: 22 March 2023 doi:10.20944/preprints202303.0387.v1

to, or even lower than, R_{smooth} (i.e. the central core of the profile lies completely, for the mass bin [4e13,7e13] h^{-1} $\mathbf{M}_{\odot}$, or almost completely, as it is the case of the mass bin [7e13,1.225e14] h^{-1} $\mathbf{M}_{\odot}$, inside the non reliable part of the profile). This fact implies an additional source of error for the concentration fit of the two less massive bins (we will try to model the smoothing of the core later in this chapter), although it seems not to influence the R_{200} fit.

M_{200} ($M_\odot$/h)	Redshift	Halos	Avg. R_{200} (Mpc/h)	$R_{200,fit}$ (Mpc/h)	Expected c_{200}	$c_{200,fit}$	χ^2_r	Q
[4.0e13,7.0e13]	[0.25,0.35]	12685	0.559	0.564	4.285	2.368	1.471	0.596
	[0.45,0.55]	15740	0.523	0.527	3.869	1.856	1.476	0.575
	[0.65,0.75]	11023	0.488	0.491	3.538	1.464	1.484	0.588
[7.0e13,1.225e14]	[0.25,0.35]	5128	0.668	0.676	4.092	2.296	1.412	0.581
	[0.45,0.55]	5641	0.619	0.629	3.705	1.800	1.389	0.584
	[0.65,0.75]	3370	0.575	0.586	3.391	1.421	1.392	0.561
[1.225e14,2.143e14]	[0.25,0.35]	1846	0.802	0.807	3.904	2.238	1.289	0.573
	[0.45,0.55]	1634	0.744	0.753	3.533	1.758	1.223	0.590
	[0.65,0.75]	722	0.690	0.696	3.235	1.387	1.218	0.545
[2.143e14,3.751e14]	[0.25,0.35]	564	0.959	0.968	3.728	2.184	1.223	0.556
	[0.45,0.55]	341	0.897	0.902	3.367	1.703	1.209	0.529
	[0.65,0.75]	138	0.831	0.835	3.084	1.349	1.186	0.533

Table 2.3: Three-dimensional best-fit NFW parameters, together with the average radius of every sample and the expected concentration. The reduced chi-square and the probability give us an idea of the goodness of fit.

Preprints (www.preprints.org) | NOT PEER-REVIEWED | Posted: 22 March 2023 doi:10.20944/preprints202303.0387.v1

Regarding the projected profiles, we find a similar trend. The values of the corresponding best-fit NFW R_{200} are in agreement with both the averaged values and those of the 3D profiles, and the best-fit NFW concentrations are again underestimated, although these are about 20-25% higher than the best-fit values of the 3D profiles (Fig. 2.8). An increase probably due to projection, that is, the shift of dark matter particles from the outer to the central bins.

We construct the projected profiles by integrating the 3D profiles (eq. 2.1) along the line-of-sight

$$\Sigma\left(R\right)=2\int_{0}^{\infty}\rho\left(r=\sqrt{R^{2}+\chi^{2}}\right)d\chi, \tag{2.9}$$

where R=$D_d\left(\theta_1^2+\theta_2^2\right)^{1/2}$ is the projected radius relative to the minimum of the potential (center of the halo) and χ is the comoving distance. The result of this integral is elegantly expressed by Wright and Brainerd [186]:

$$\Sigma_{NFW}\left(x\right)=\begin{cases}\frac{2r_s\delta_c\rho_c}{(x^2-1)}\left[1-\frac{2}{\sqrt{1-x^2}}\operatorname{arctanh}\sqrt{\frac{1-x}{1+x}}\right] & \text{x<1,}\\ \frac{2r_s\delta_c\rho_c}{3} & \text{x=1,}\\ \frac{2r_s\delta_c\rho_c}{(x^2-1)}\left[1-\frac{2}{\sqrt{x^2-1}}\arctan\sqrt{\frac{x-1}{1+x}}\right] & \text{x>1.}\end{cases} \tag{2.10}$$

For convenience, a dimensionless transverse distance has been adopted, x=R/r_s.

Summarizing, the fact that our best-fit NFW concentrations, both for the 3D and the projected profiles, are relatively much lower than expected obeys to different reasons, namely, the low mass resolution of our simulations, the softening length, and the stacking of both relaxed and unrelaxed halos. Previous works, like that of Neto et al. [129], establish a minimum number of particles (1,000 in this particular work) within r_{vir} required to obtain unbiased estimates of the concentrations; the greater the number of particles within r_{vir}, the better fit to the NFW profile and the better estimation of the concentration, regardless their equilibrium state. Moreover, they claim that concentration distributions of both unrelaxed and relaxed halos may be approximated by a lognormal distribution

$$p\left(c_{200}\right)dc_{200}=\frac{1}{\sqrt{2\pi}\sigma_c}\exp\left[-\frac{\left(\ln c_{200}-\ln c_{200,median}\right)^2}{2\sigma_c^2}\right]d\ln c_{200}\ , \tag{2.11}$$

Preprints (www.preprints.org) | NOT PEER-REVIEWED | Posted: 22 March 2023 doi:10.20944/preprints202303.0387.v1

where, for the former, the dispersion in concentration seems to decrease as a function of mass, suggesting that massive halos are a more homogeneous population than those with lower mass. This could account for the fact that the more massive ranges produce the better estimates for the concentrations, i.e. the ratio $C_{200,fit}/C_{200,\text{expected}}$ is closer to one for these samples than in the low mass cases. Neto et al. also find that the median of the concentration distribution of the relaxed halos is a good approximation of the overall concentration of the distribution for all halos, being its value $\sim 35\%$ (on average) higher than the median of the concentration distribution of the unrelaxed halos. In our case, the overall concentration of the relaxed halos (r<0.2) is $\sim 33\%$ (on average) higher than the overall concentration of the distribution for all halos, and this could be due to the fact that our fraction of unrelaxed halos in each mass range, and for every redshift bin, is higher than that of Neto et al[1] (see Table 2.2).

In Fig. 2.9, we compare four 3D and four projected stacked density profiles with their corresponding NFW expected profiles (considering the value of the best-fit NFW radius as correct and determining the concentration from eq. 2.8). The difference between the stacked density profiles and their expected NFW profiles seems to be relatively small, the latter providing an even better fitting in the outermost region of the halo, but significant enough in the central region to account for the significant departure of the concentration from the expected value.

[1] Although our mass ranges are not exactly the same as those used by Neto et al., they can be easily compared, since they find that the fraction of unrelaxed halos increases almost consistently with mass.

Preprints (www.preprints.org) | NOT PEER-REVIEWED | Posted: 22 March 2023 doi:10.20944/preprints202303.0387.v1

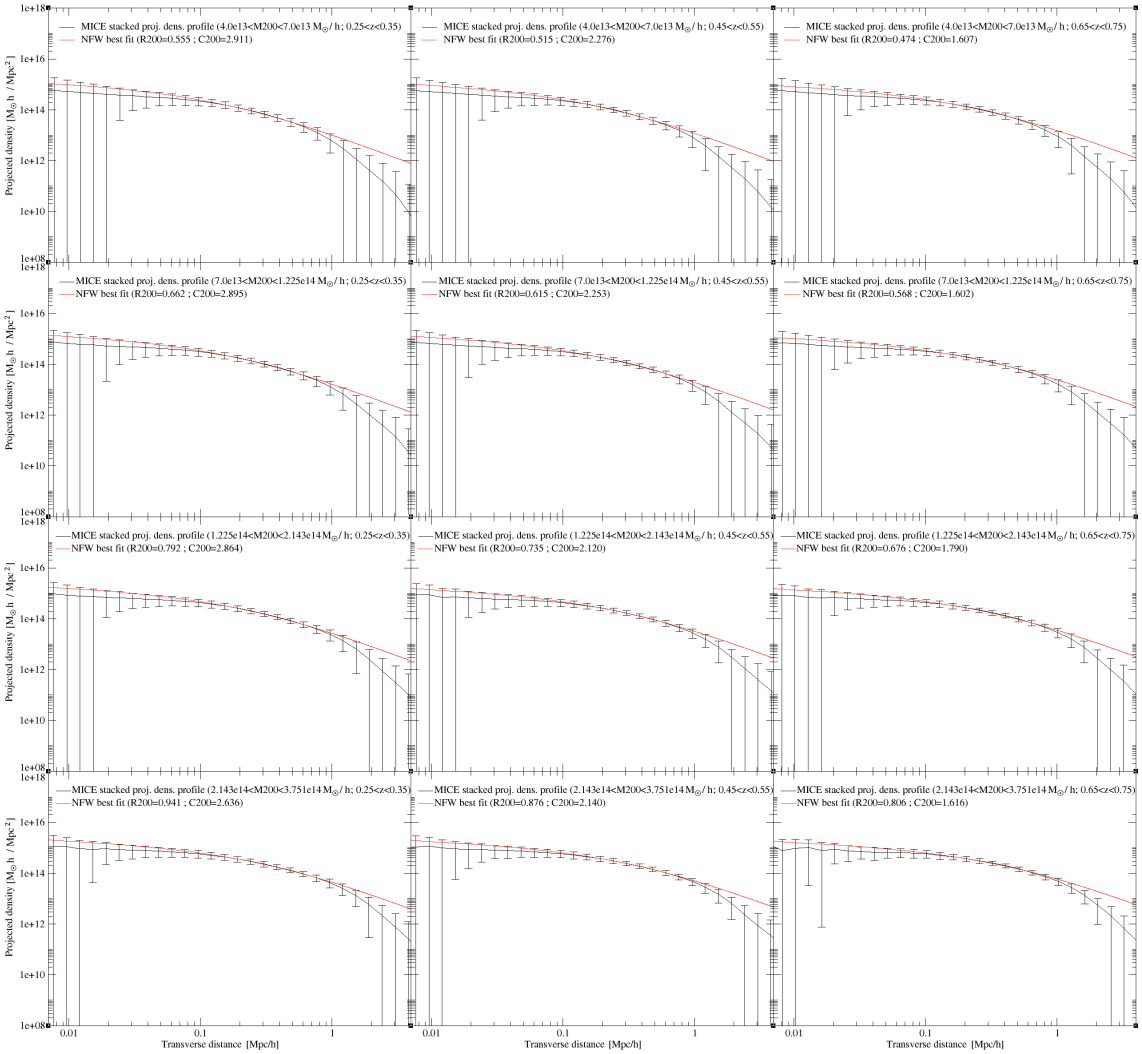

Figure 2.8: Stacked projected density profiles from three different redshift ranges and the four mass samples specified in Table 2.2. Best-fit NFW radii are in agreement with those resulting from the NFW 3D fit, but best-fit concentrations are a bit higher.

Preprints (www.preprints.org) | NOT PEER-REVIEWED | Posted: 22 March 2023 doi:10.20944/preprints202303.0387.v1

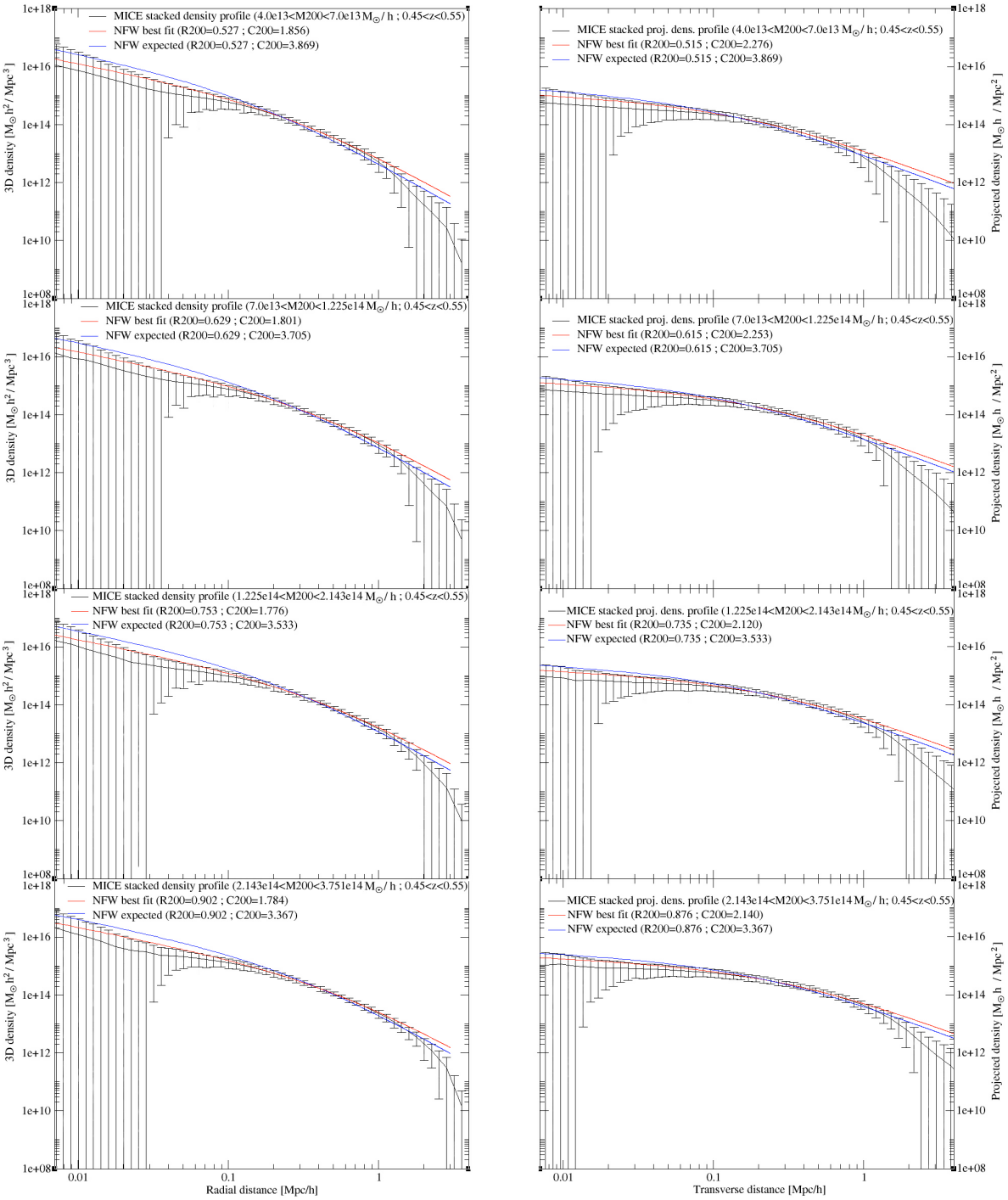

Figure 2.9: Comparison of MICE 3D and projected (stacked) density profiles with their corresponding NFW expected density profiles. For the sake of clarity, and since the rest of profiles present a similar behaviour (namely, the inner cusp of the best-fit NFW profile flatter than that of the expected NFW profile),we show the density profiles from all the mass ranges, but only one redshift bin ($0.45<z<0.55$)

M_{200} ($M_\odot$/h)	Redshift	Halos	Avg. R_{200} (Mpc/h)	$R_{200,fit}$ (Mpc/h)	Expected c_{200}	$c_{200,fit}$	χ^2_r	Q
[4.0e13,7.0e13]	[0.25,0.35]	12685	0.559	0.555	4.285	2.911	1.360	0.586
	[0.45,0.55]	15740	0.523	0.515	3.869	2.276	1.354	0.579
	[0.65,0.75]	11023	0.488	0.474	3.538	1.607	1.371	0.591
[7.0e13,1.225e14]	[0.25,0.35]	5128	0.668	0.662	4.092	2.895	1.343	0.588
	[0.45,0.55]	5641	0.619	0.615	3.705	2.253	1.324	0.580
	[0.65,0.75]	3370	0.575	0.568	3.391	1.602	1.319	0.573
[1.225e14,2.143e14]	[0.25,0.35]	1846	0.802	0.792	3.904	2.864	1.247	0.585
	[0.45,0.55]	1634	0.744	0.735	3.533	2.120	1.209	0.589
	[0.65,0.75]	722	0.690	0.676	3.235	1.790	1.196	0.561
[2.143e14,3.751e14]	[0.25,0.35]	564	0.959	0.941	3.728	2.636	1.212	0.544
	[0.45,0.55]	341	0.897	0.876	3.367	2.140	1.201	0.531
	[0.65,0.75]	138	0.831	0.806	3.084	1.616	1.189	0.526

Table 2.4: Projected best-fit NFW parameters, together with the average radius of every sample and the expected concentration. The reduced chi-square and the probability give us an idea of the goodness of fit.

Preprints (www.preprints.org) | NOT PEER-REVIEWED | Posted: 22 March 2023 doi:10.20944/preprints202303.0387.v1

2.5 Analytical NFW profiles

In order to better understand the nature of our halos we create pure NFW profiles. So far, regarding the parametric modeling of MICE halos, our estimates of R_{200} are in good agreement with their corresponding overall virial radii, but we have some issues with the concentration estimates. Assuming that the NFW profile is a good approximation for MICE density profiles, the construction of analytical profiles will help us understand the effect of mass resolution on the concentration parameter.

Since we want to compare these analytical density profiles to the MICE density profiles, we have build a catalogue with the estimates of the virial radius and the expected concentration of every halo in our samples (Table 2.3) so we can simulate and stack their corresponding pure NFW profiles. Once known R_{200} and c_{200}, we can build the analytical profiles by dividing the theoretical NFW into 50 bins, and assigning to each bin the density value correspondent to its radius. Next we "fill" that bin with particles until we reach the assigned density or the density limit, i.e. the highest possible value, given the particle mass, without exceeding the assigned density. Every particle is given a random angular position (θ, ϕ)[2], an aspect that might not be relevant for the 3D profiles, but that will be essential for the subsequent calculation of the projected profiles. Halos from each of our samples are thus simulated with four different particle masses: 2.34×10^{11} (MICE mass resolution), 2.34×10^{10}, 2.34×10^{9} and 5.0×10^{8} h^{-1} $\mathbf{M}_{\odot}$.

After stacking all the pure NFW 3D profiles from each sample, we make use again of eq. 2.4 to fit the resulting profiles. A comparison of all our MICE samples with their corresponding analytical NFW samples, with the same mass resolution (m_p=2.34×10^{11}), is shown in Table 2.6. Fig. 2.12 shows the stacked analytical NFW projected profiles from the sample $M_{200} \in [2.143e14, 3.751e14]$ at z$\in$ [0.65, 0.75], for the four different mass resolutions. The lowest resolution projected profile, when compared with those with higher resolutions, presents a flatter core, and increasing mass resolution by a factor of ten raises density by the same factor (an impact similar to that observed for the 3D profiles).

[2] Remember that the third spherical coordinate is determined by the radius of the bin.

Preprints (www.preprints.org) | NOT PEER-REVIEWED | Posted: 22 March 2023 doi:10.20944/preprints202303.0387.v1

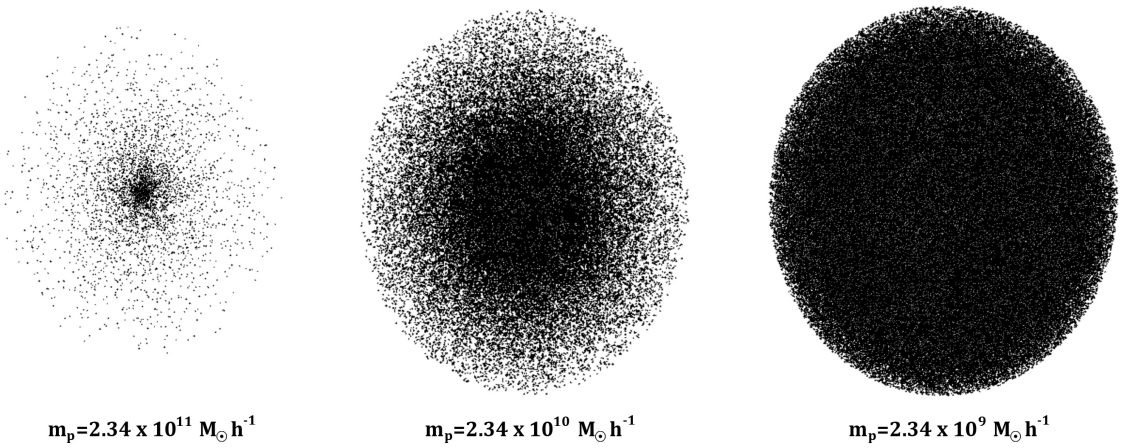

Figure 2.10: A sample halo simulated three times with an increasing mass resolution.

Particle mass(h^{-1} $\mathbf{M}_\odot$)	**No. of particles within** $\mathbf{R}_{200}$
2.34×10^{11}	$\sim$ 1600
2.34×10^{10}	$\sim$ 1.6e4
2.34×10^{9}	$\sim$ 1.6e5
5.0×10^{8}	$\sim$ 7.4e5

Table 2.5: Number of particles within the virial radius for the different mass resolutions. These numbers correspond to MICE most massive halos.

As it can be seen in Table 2.5, the number of particles within R_{200} is greater than one thousand, but only for the largest halos. Most of MICE halos do not reach this minimum value, therefore biasing the estimation of concentration.

The fit to the analytical NFW stacked profiles has been performed making use of MICE-like errors. We have assigned to every bin of the analytical profiles, based on their radial or transverse distance, an error of the magnitude of MICE errors at the same distance. In this way, not only we get a better fit to the analytical profiles, but we also ensure a fair comparison between them and MICE profiles. An example of this is shown in Fig. 2.11. All the fitting curves shown in Fig. 2.12 have been performed using MICE-like errors, but we have opted to superimpose them

Preprints (www.preprints.org) | NOT PEER-REVIEWED | Posted: 22 March 2023 doi:10.20944/preprints202303.0387.v1

to the profiles with Poisson error bars in order to visualize how well they fit them.

If we attend to the results shown in Tables 2.6 and 2.7, it becomes clear that concentrations of the analytical projected NFW profiles are closer to the input values than those of the spherical (3D) ones, and that the concentration ratio shows the same trend both for MICE and analytical NFW halos. MICE halos exhibit both a relatively high value of the softening length and low mass resolution, characteristics that tend to subtract density from the innermost part of the profile; but we should expect the stacked projected density profiles to have a concentration higher than their 3D counterparts, due to projection effects. This is precisely what we observe, since the stacking of MICE projected profiles produces a transfer of density from the outer layers of the halo to its inner core, this being consistent for all the mass samples at every redshift, and in agreement with the behavior of the projected pure NFW profiles with a random angular distribution of particles. We may therefore conclude that MICE average density profiles are spherical, or at least that their projection effects are, regarding NFW concentration, similar to those affecting the pure NFW profiles. We have also detected that a choice of mass resolution like that of MICE results in about a 40% decrease in concentration for the 3D profiles, and about a 25% decrease for the projected profiles. MICE mass resolution is too low to obtain a good estimate of the concentration, and improving mass resolution by just a factor of 10 would render a better estimate of the concentration; this last conclusion is in agreement with the previous claim of Neto et al. related to the minimum number of particles (>1000) within $R_{200.}$ It is also worth taking into account that the NFW profile is a good approximation of the density profile of a dark matter halo in equilibrium, so we expect (and find) the estimates of the concentrations obtained from the pure NFW halos to be systematically higher (for all the samples) than those obtained from MICE data, since our samples combine relaxed with unrelaxed halos. The aforementioned discrepancies between best-fit and input concentrations (40% for 3D profiles, and 25% for projected profiles) thus become lower boundaries of the effect of MICE mass resolution on concentration estimates.

Preprints (www.preprints.org) | NOT PEER-REVIEWED | Posted: 22 March 2023 doi:10.20944/preprints202303.0387.v1

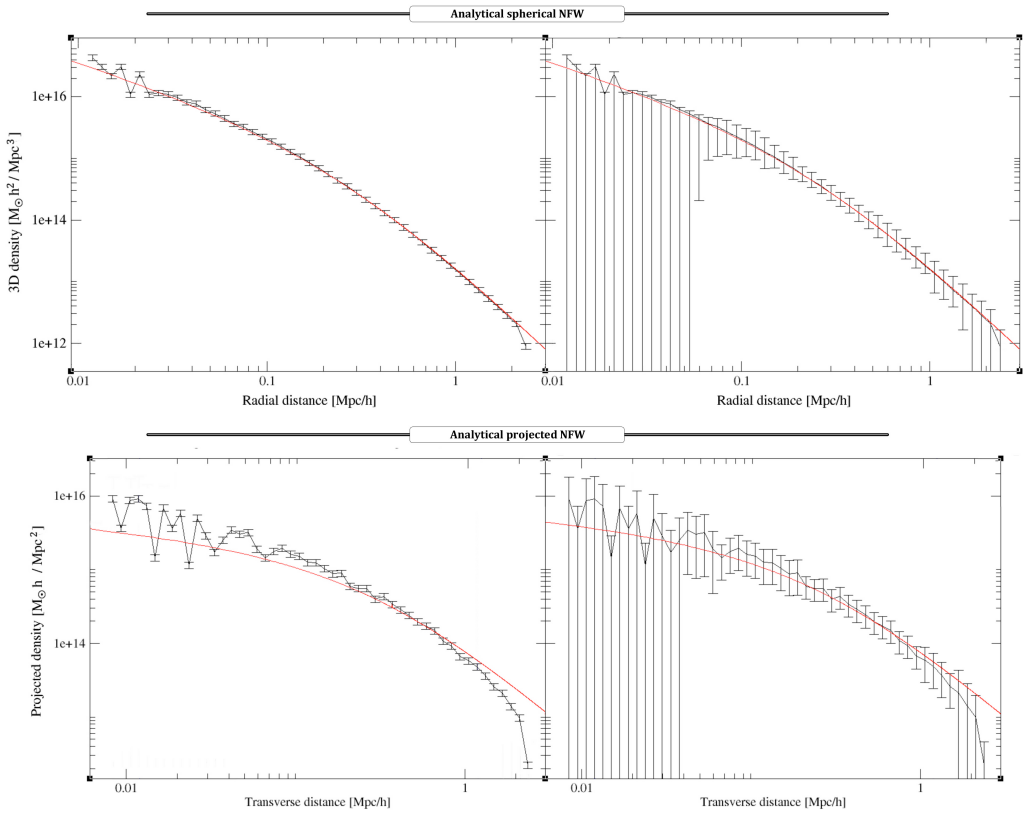

Figure 2.11: A comparison between the analytical (3D and projected) NFW profiles with Poisson error bars and the same profiles with MICE-like error bars. These profiles correspond to the sample M4 at z$\in$ $[0.65, 0.75]$, and to the lowest mass resolution (MICE mass resolution).

Preprints (www.preprints.org) | NOT PEER-REVIEWED | Posted: 22 March 2023 doi:10.20944/preprints202303.0387.v1

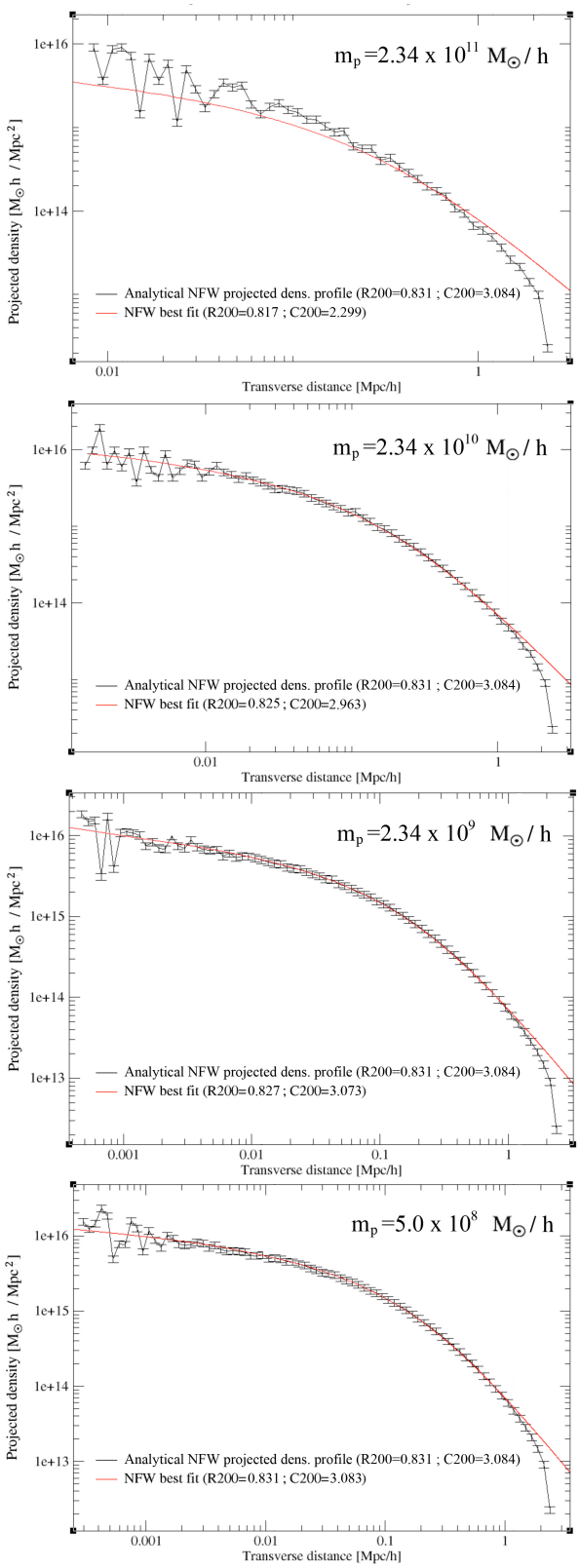

Figure 2.12: Pure NFW projected density profiles for four different mas resolutions. Best-fit NFW parameters get closer to the input values as resolution improves, but it can be easily seen that just increasing mass resolution by an order of magnitude is enough to have a good estimation of the input values.

$\mathbf{M_{200}}$ (h^{-1} $\mathbf{M_\odot}$)	**Redshift**	**Halos**	Input $\mathbf{R_{200}}$ **(Mpc/h)**	NFW 3D $\mathbf{R_{200,fit}}$ **(Mpc/h)**	NFW 2D $\mathbf{R_{200,fit}}$ **(Mpc/h)**	Input $\mathbf{c_{200}}$	NFW 3D $\mathbf{c_{200,fit}}$	NFW 2D $\mathbf{c_{200,fit}}$
M1	[0.25,0.35]	12685	0.559	0.552	0.549	4.285	2.522	3.152
	[0.45,0.55]	15740	0.523	0.520	0.516	3.869	2.300	2.905
	[0.65,0.75]	11023	0.488	0.484	0.480	3.538	2.090	2.675
M2	[0.25,0.35]	5128	0.668	0.664	0.659	4.092	2.519	3.033
	[0.45,0.55]	5641	0.619	0.616	0.608	3.705	2.257	2.713
	[0.65,0.75]	3370	0.575	0.572	0.569	3.391	2.077	2.499
M3	[0.25,0.35]	1846	0.802	0.799	0.794	3.904	2.440	2.823
	[0.45,0.55]	1634	0.744	0.739	0.733	3.533	2.236	2.571
	[0.65,0.75]	722	0.690	0.683	0.678	3.235	1.897	2.225
M4	[0.25,0.35]	564	0.959	0.951	0.947	3.728	2.550	2.871
	[0.45,0.55]	341	0.897	0.891	0.888	3.367	2.258	2.576
	[0.65,0.75]	138	0.831	0.826	0.817	3.084	2.039	2.308

Table 2.6: Comparison of the input values with the best-fit NFW parameters for both the 3D and the projected density profiles. The input values of the virial radii come from the average virial radius of each MICE sample, whereas the input concentration values are the expected values according to eq. 2.8. These are the estimates from the fit of the analytical profiles with a mass resolution equal to that of MICE simulation.

		Concentrations ratio: $C_{200,2D}/C_{200,3D}$				
M_{200} (h^{-1} $M_\odot$)	**Redshift**	**MICE m_p=2.34×10^{11}**	**NFW m_p=2.34×10^{11}**	**NFW m_p=2.34×10^{10}**	**NFW m_p=2.34×10^{9}**	**NFW m_p=5×10^{8}**
M1	[0.25,0.35]	1.229	1.250	1.248	1.245	1.228
	[0.45,0.55]	1.226	1.263	1.255	1.212	1.205
	[0.65,0.75]	1.098	1.280	1.279	1.277	1.259
M2	[0.25,0.35]	1.261	1.204	1.199	1.195	1.186
	[0.45,0.55]	1.252	1.202	1.198	1.194	1.181
	[0.65,0.75]	1.127	1.203	1.199	1.195	1.184
M3	[0.25,0.35]	1.280	1.157	1.149	1.142	1.134
	[0.45,0.55]	1.206	1.150	1.146	1.146	1.131
	[0.65,0.75]	1.290	1.173	1.169	1.167	1.143
M4	[0.25,0.35]	1.207	1.126	1.122	1.122	1.115
	[0.45,0.55]	1.257	1.141	1.133	1.123	1.107
	[0.65,0.75]	1.198	1.132	1.119	1.126	1.108

Table 2.7: Ratio of the concentration of the projected density profiles to that of the 3D density profiles. Third column corresponds to the ratio for MICE halos, and the next columns to the ratio of the analytical NFW profiles with four different particle masses.

Preprints (www.preprints.org) | NOT PEER-REVIEWED | Posted: 22 March 2023 doi:10.20944/preprints202303.0387.v1

2.6 Modeling the flat core of the halo

We have now a better understanding of how mass resolution modifies the innermost region of the density profiles, and we can even quantify it. But flattening appears also as a result of the softeningh length, and we can assert that it is the most relevant factor to that condition.

One way of modeling the effect of the softening on the profile consist in convolving the expected NFW profile with a Gaussian filter function

$$\begin{aligned} \widetilde{\rho}_{NFW}\left(\overrightarrow{r}\right) &= \int\int\int \rho_{NFW}\left(\overrightarrow{r_1}\right) \frac{1}{\left(\sigma\sqrt{2\pi}\right)^3} \exp\left(-\frac{(\overrightarrow{r}-\overrightarrow{r_1})^2}{2\sigma^2} d^3r_1\right) \\ &= \frac{1}{r\sigma\sqrt{2\pi}} \exp\left(-\frac{r^2}{2\sigma^2}\right) \int_0^{R_{200}} dr_1(r_1)\rho_{NFW}(r_1) \exp\left(-\frac{r_1^2}{2\sigma^2}\right) \; F(rr_1), \end{aligned} \tag{2.12}$$

where

$$F(rr_1) = \left[\exp\left(\frac{rr_1}{\sigma^2}\right) - \exp\left(-\frac{rr_1}{\sigma^2}\right)\right] \tag{2.13}$$

This solution has been adopted in earlier works such as that by Smith et al. [160], assigning to σ a value of 2.5 times the softening length. The central region of the MICE profiles centered at the minimum of potential is flatter than that of the expected NFW profiles, but clearly shallower than the core of the MICE profiles centered at the center of mass (see Fig. 2.13). Lets see if the aforementioned convolution is a convenient way of modeling MICE density profiles.

The result of applying the gaussian kernel to the expected NFW density profiles is shown in Fig. 2.14. The resultant profiles do not seem to be a good approximation for our 3D profiles, at least when we compare the former with the MICE profiles whose center is the minimum of potential. A comparison with the MICE profiles centered at the center of mass is shown in Fig. 2.15. In this case the gaussian smoothing technique gives better statistical results (assuming $\sigma = 2l_{soft}$), and allows us to model, to some extent, the flattening issue. Nonetheless, if we take into account the error bars of the two types of density profiles, centered at the minimum of potential and at the center of mass, the smoothed expected NFW profile lies within the error bars of both, although the fitting is statistically more relevant for the latter. Some examples are shown below.

Preprints (www.preprints.org) | NOT PEER-REVIEWED | Posted: 22 March 2023 doi:10.20944/preprints202303.0387.v1

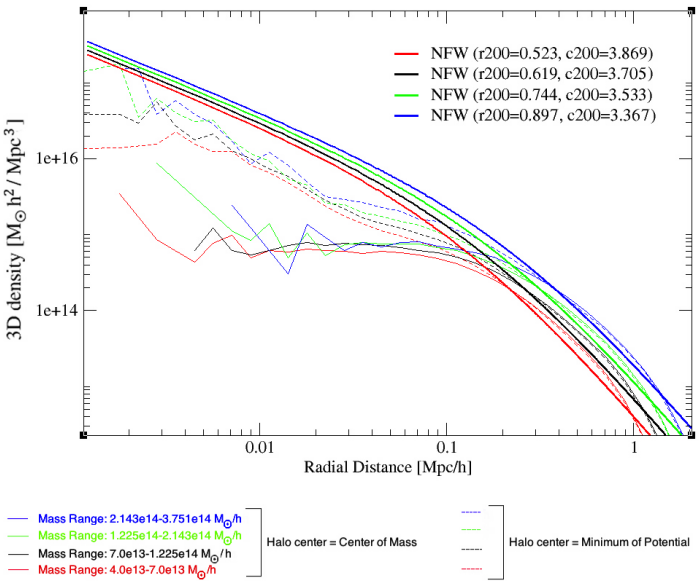

Figure 2.13: Radial density profiles of MICE halos centered at the minimum of potential (dashed lines), MICE halos centered at the center of mass (thin solid lines), compared with their corresponding expected NFW profiles (thick solid lines).

Preprints (www.preprints.org) | NOT PEER-REVIEWED | Posted: 22 March 2023 doi:10.20944/preprints202303.0387.v1

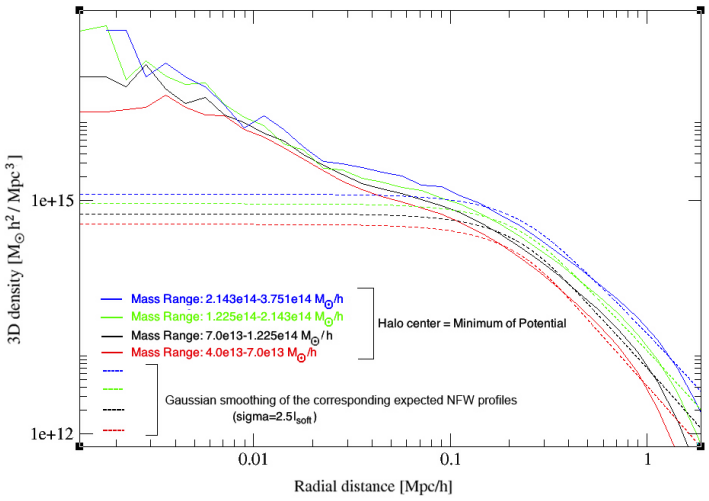

Figure 2.14: Comparison of MICE stacked 3D density profiles, centered at the minimum of potential, to those resultant from the convolution of the expected NFW profiles with the gaussian kernel.

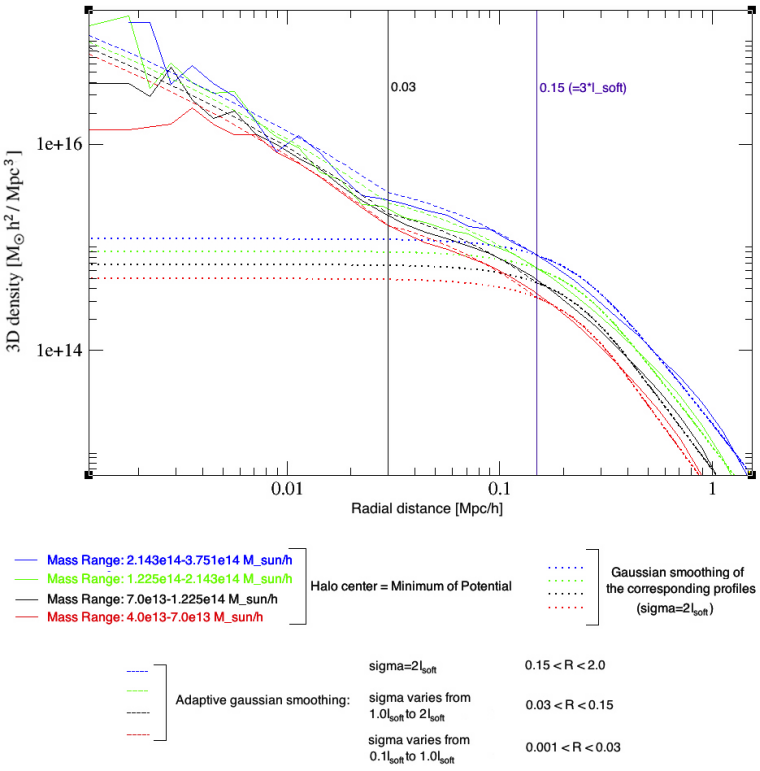

Figure 2.16: Modeling of the core of MICE stacked 3D density profiles with the adaptive gaussian smoothing.

Preprints (www.preprints.org) | NOT PEER-REVIEWED | Posted: 22 March 2023 doi:10.20944/preprints202303.0387.v1

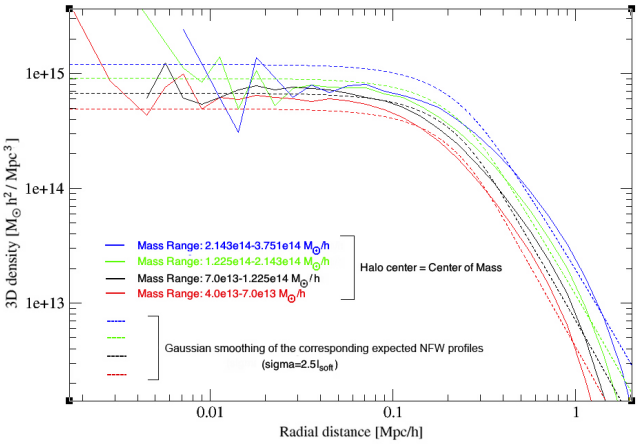

Figure 2.15: Comparison of MICE stacked 3D density profiles, centered at the center of mass, to those resultant from the convolution of the expected NFW profiles with the gaussian kernel.

The innermost region of MICE 3D profiles can be relatively well-modeled by the gaussian filter (Fig. 2.17) with $\sigma = 2l_{soft}$, because it better fits MICE data. But we have also been able to model it using an ad-hoc gaussian kernel (adaptive gaussian smoothing): a piecewise function where the value of σ varies linealry from $0.1l_{soft}$ to $2l_{soft}$ through two intervals, and remains constant ($\sigma = 2l_{soft}$) in the third and last interval (see Fig. 2.16). This adaptive smoothing fits very well the innermost regions of the profiles. Both ways of modeling the core of the 3D density profiles yield a similar reduced chi square, $\chi^2_r \in [1.78, 2.57]$, depending on the mass and redshift bins (most massive samples yield lower values of χ^2_r).

Preprints (www.preprints.org) | NOT PEER-REVIEWED | Posted: 22 March 2023 doi:10.20944/preprints202303.0387.v1

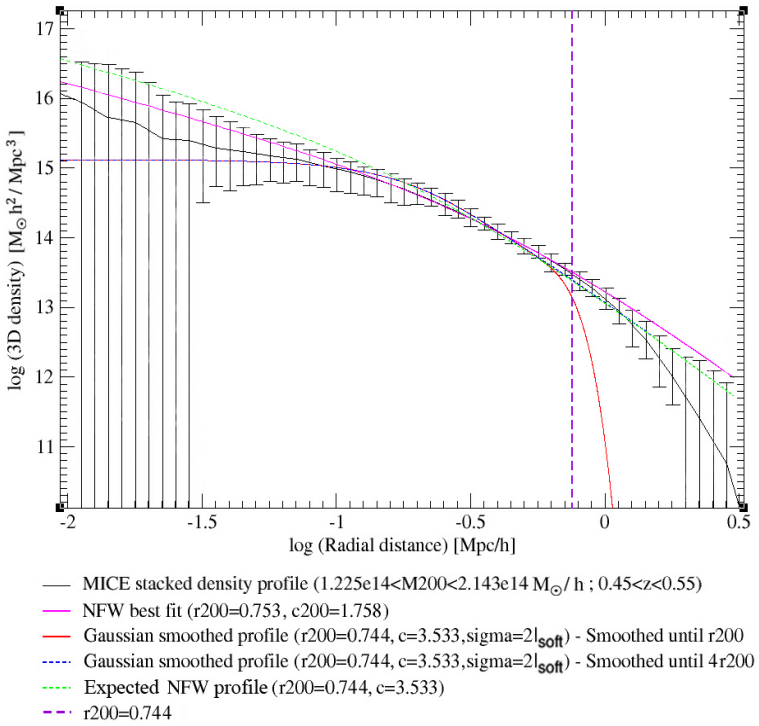

Figure 2.17: Modeling of the core of a 3D density profile with a gaussian kernel ($\sigma = 2l_{soft}$).The resultant smoothed profile lies within the error bars and it better fits our data when extending the smoothing from R_{200} to $4R_{200}$. In this way the smoothed profile resembles closely, at the outer regions of the profile, the expected NFW profile.

Despite the logical interest in modeling the flattening of the central region of the 3D profiles, since our goal is the mass calibration of MICE halos, we are more interested in modeling that same feature for the projected profiles. MICE projected profiles present a core flatter than that of their 3D counterparts, which is an advantage when it comes to modeling. In order to use the gaussian kernel for this purpose we need to smooth the expected NFW density profile and then integrate it along the line of sight

$$\Sigma\left(R\right) = 2\int_0^\infty \widetilde{\rho}_{NFW}\left(r = \sqrt{R^2 + \chi^2}\right) d\chi \ . \tag{2.14}$$

Preprints (www.preprints.org) | NOT PEER-REVIEWED | Posted: 22 March 2023 doi:10.20944/preprints202303.0387.v1

A modeling of the projected density profile of the mass sample [1.225e14,2.143e14] at z$\in$ $[0.45, 0.55]$ is shown in Fig. 2.18. We find for this sample, as well as for the rest of the samples we have defined, that the convolution of the gaussian filter function with the expected NFW profiles results in a very good approximation to MICE projected profiles. In the literature, the smoothing is usually applied up to r=R_{200}, but MICE halos do not display a steep drop in density at the outer region of the profile, as many other from different simulations do, so we have decided to extend the smoothing up until r=$4R_{200}$. In this way, the resultant smoothed density profile shows a better fit to our data throughout the profile.

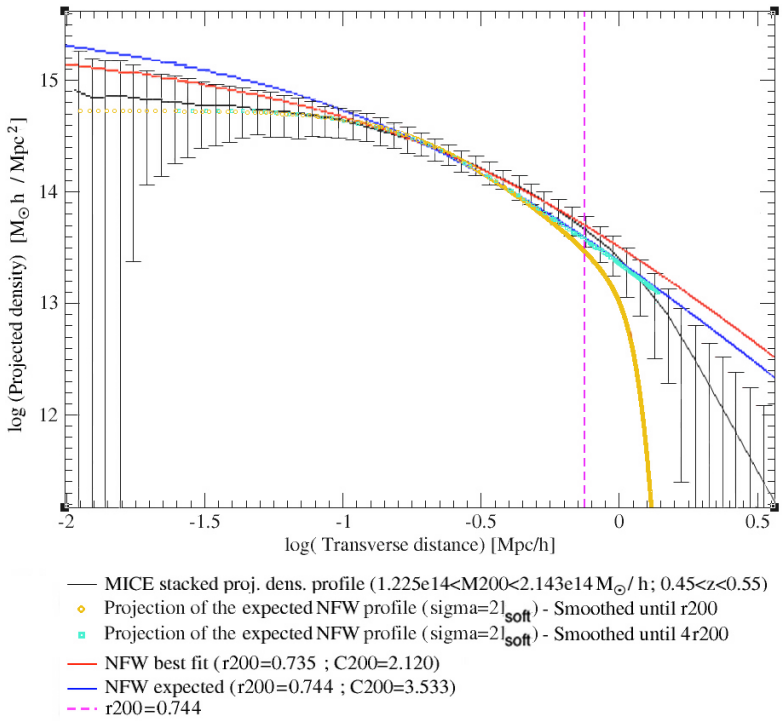

Figure 2.18: Modeling of the core of a projected density profile with a gaussian kernel ($\sigma = 2l_{soft}$).

The goodness of fit between the smoothed expected NFW profiles and MICE projected density profiles is again influenced by the sample mass, the greater the mass, the lower is the value of the reduced chi-square. The values of χ^2_r thus obtained lie in the interval $[1.23, 1.77]$, and the

Preprints (www.preprints.org) | NOT PEER-REVIEWED | Posted: 22 March 2023 doi:10.20944/preprints202303.0387.v1

corresponding values of Q (eq. 2.6) are in the interval $[0.5, 0.685]$, hence allowing us to reliably model our stacked projected density profiles.

2.7 Conclusions

The NFW universal density profile is frequently used in many works on very different subjects (mass calibration and primordial non-gaussianity, among others), and has proven to be a very good overall description of the density profiles of dark matter halos from numerical simulations. We have therefore based our analysis on the assumption that NFW profile is a good representation of MICE profiles.

We have made use of twelve different samples (four mass ranges, every one at three different redshift ranges), which have been chosen in order to be representative of the whole simulation. We have positioned the center of our halos in the minimum of potential and have made no distinction between relaxed and unrelaxed halos.

In the case of the 3D profiles, the best-fit NFW virial radii (R_{200}) are very close to the averaged values of R_{200} from each sample, overestimating it only by 1%. Regarding the concentration, the best-fit NFW results underestimate the expected values by up to 43-57%, depending on the redshift. Our data suggest that selecting the halos by their degree of relaxedness could substantially improve concentration estimates (up to a 30% for the most relaxed halos), as claimed by Jeeson-Daniel et al. [94].

Regarding the projected profiles, the best-fit NFW virial radii are in good agreement both with the averaged values of R_{200} and the estimates from the spherical profiles. Best-fit NFW concentrations underestimate again the expected values, but there is an increase of about 20-25% as compared to the estimates from the 3D profiles, due to projection effects.

In order to distinguish between the effects of mass resolution and those of the softening length, we have mimicked our twelve halo samples, populating them with analytical NFW halos. Actually, we have replicated our data sets four times, each one with a different mass resolution: 2.34×10^{11} (MICE mass resolution), 2.34×10^{10}, 2.34×10^{9} and 5.0×10^{8} h^{-1} $\mathbf{M}_{\odot}$. For each halo we have defined two input values (R_{200}, c_{200}): the first comes from our halo catalogue, and the second

 doi:10.20944/preprints202303.0387.v1

is the expected concentration. The best-fit NFW estimates of the virial radii obtained from both the stacked 3D and projected profiles are very similar to each other and to the average R_{200} of each sample, and relatively independent of mass resolution. On the other hand, the best-fit NFW concentrations are clearly resolution-dependent, and drop 40% and 25% for the 3D and the projected profiles, respectively. Considering that the NFW density profile is a good description of a dark matter halo in equilibrium, and that our samples combine relaxed with unrelaxed halos, we understand those percentages as lower boundaries of the decrease in concentration associated with low mass resolution.

Finally, in order to find a way of modeling the whole density profile without needing to consider all the possible effects (mass resolution, softening length, degree of relaxedness, ...) we have convolved a gaussian filter with the expected NFW density profile of each sample. We find that MICE projected density profiles are statistically well approximated by the profiles resultant from the convolution. This fact would be of much interest in the subsequent mass calibration process.

 doi:10.20944/preprints202303.0387.v1

Chapter 3

The Shape of MICE Dark Matter Halos

"*Painting dissolves the forms at its command, or tends to; it melts them into color. Drawing, on the other hand, goes about resolving forms, giving edge and essence to things. To see shapes clearly, one outlines them–whether on paper or in the mind. Therefore, Michelangelo, a profoundly cultivated man, called drawing the basis of all knowledge whatsoever.*"

Sight and Insight, Alexander Eliot

The properties of dark matter halos, particularly their density profile and shape, have been extensively studied, since they have been argued to be sensitive to the key properties of the dark matter. Numerical simulations are a fundamental tool to study the features of the dark matter halos, exploring for instance the effects of the mass assembly history, environment and the nature of dark matter itself (e.g., Bullock [27]; Bett et al. [22]; Macciò et al. [117]; Hahn et al. [73]; Spergel & Steinhardt [161]; Yoshida et al. [187]; Avila-Reese et al. [8]; Strigari, Kaplinghat & Bullock [167]; Wang & White [181]).

The top-hat spherical collapse model (Gunn & Gott [71]; Fillmore & Goldreich [57]), as most of the first analytical models of the formation of dark matter halos, considered symmetric configurations. However, works like those by Frenk et al. [61]; Dubinski & Carlberg [46]; Warren

Preprints (www.preprints.org) | NOT PEER-REVIEWED | Posted: 22 March 2023 doi:10.20944/preprints202303.0387.v1

et al. [183]; Cole & Lacey [33]; Thomas et al. [35] found important deviations from spherical symmetry by measuring the shape of halos in numerical N-body simulations evolved in a fully cosmological context. These authors consistently obtained that after virialization, dark matter halos are triaxial with more oblate shapes in the outskirtsand more prolate shapes towards the center. Current high resolution N-body simulations have provided similar conclusions (Jing & Suto [96]; Bailin & Steinmetz [12]; Kasun & Evrard [101]; Hopkins, Bahcall & Bode [87]; Bett et al. [22]; Hayashi, Navarro & Springel [74]; Kuhlen, Diemand & Madau [104]; Stadel et al. [166]; Diemand & Moore [42]).

Additional studies based on numerical simulations have also shown that the mass assembly history and environment of a halo may play a crucial role in determining its shape. Tormen [174] and Colberg et al. [32] suggested that the anisotropic infall of matter into cluster-sized halos was largely responsible for their orientations, shape and dynamics at different epochs. As infall is governed by the surrounding large scale structure, we anticipate significant correlations between the halo shapes and their environment, although we can find evidence both against and in support of such trends in the literature (Lemson & Kauffmann [110]; Avila-Reese et al. [7]; Faltenbacher et al. [53]; Altay, Colberg & Croft [3]; Basilakos et al. [14]; Gottlöber & Turchaninov [68]; Patiri et al. [135]; Aragón-Calvo et al. [5]; Hahn et al. [72]; Macciò et al. [117]; Ragone-Figueroa et al. [142]).

The observational determination of the shapes of halos is arduous. Constraints on these shapes have been established, in external galaxies, using the intrinsic shape of galactic disks (Fasano et al. [55]), the morphology and kinematics of the HI layer (Olling [134]; Becquaert & Combes [17]; Swaters, Sancisi & van der Hulst [168]), the temperature profile, morphology of X-ray isophotes (Buote & Canizares [29]; Buote et al. [30]), gravitational lensing (Hoekstra, Yee & Gladders [86]) and the spatial distribution of galaxies within groups (Robotham, Phillipps & De Propris [148]). All of these studies agree that halos tend to be nearly oblate, and have their smallest axis pointing perpendicular to the symmetry plane defined by the stellar constituent. However, most of these constrains belong to the inner regions of galaxy-scale halos.

From the theoretical point of view, there is a gap in our knowledge about the way in which dark matter halos acquire their shape, and in particular, on the impact of the dynamics of the

Preprints (www.preprints.org) | NOT PEER-REVIEWED | Posted: 22 March 2023 doi:10.20944/preprints202303.0387.v1

large scale structure in the non-linear regime (Lee, Jing & Suto [108]; Betancort-Rijo & Trujillo [21]; Rossi, Sheth & Tormen [149]; Salvador-Solé et al. [151]). Indeed, most of the works cited above are restricted to the present day correlations with the environment, and do not consider the moment when shapes have been established or how they relate to the past history of a particular object.

3.1 Halo shape determination

One way of quantifying the shape of halos is to approximate them by ellipsoids, which are characterised by three axes, a, b, c, with a≥ b≥ c. For our purposes is better to describe them in terms of ratios, p ≡ c/b, q ≡ b/a, and s≡ c/a, which is a common alternative. Ellipsoids are usually divided into three classes, each one with their corresponding ratio ranges: oblate ellipsoids have a≈ b > c leading to axial ratios of s ≈ p < q, prolate ellipsoids have a > b ≈ c leading to axial ratios of s ≈ q < p, and triaxial ellipsoids are in between oblate and prolate with a > b > c.

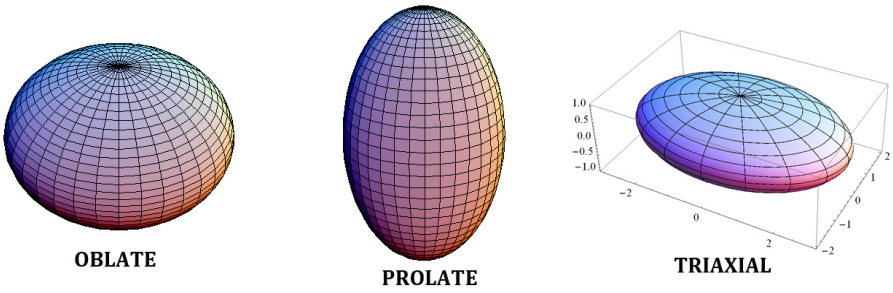

Figure 3.1: Morphological classification of dark matter halos in terms of their axes ratios.

We use the MICE simulations (see section 2.1), and in order to determine shapes of halos we have opted for a method based on the determination of the inertia tensor. One of the drawbacks of these methods is its quadratic relation with distance, which assigns the largest weight to particles that reside far away from the center, an issue made challenging by the presence of substructures in the outskirts of the halos. The bias thus introduced can be alleviated by normalizing each coordinate with some measure of distance. In our case the elliptical distance in the eigenvector

Preprints (www.preprints.org) | NOT PEER-REVIEWED | Posted: 22 March 2023 doi:10.20944/preprints202303.0387.v1

coordinate system from the centre to the nth particle.

$$I_{ij} \equiv \sum_n \frac{x_{i,n}\ x_{j,n}}{r_n^2} \tag{3.1}$$

$$r_n = \sqrt{x_n^2 + y_n^2/q^2 + z_n^2/s^2} \tag{3.2}$$

We have followed here the iterative scheme proposed by Allgood et al. [2], keeping the largest axis length constant. The number n comes from the number of particles located inside a sphere of radius R_{200} which is reshaped iteratively using the eigenvalues. The axis ratios are the ratios of the square-roots of the eigenvalues $\left(\lambda_a \leq \lambda_b \leq \lambda_c \text{ with } a = \sqrt{\lambda_a},\ b = \sqrt{\lambda_b},\ c = \sqrt{\lambda_c}\right)$of the inertia tensor, and the directions of the principal axes are given by the corresponding eigenvectors.

The iterative method consist in determining **I** with s=1 and q=1, including all particles within R_{200}. Subsequently, we calculate new values for s and q, thus reshaping the volume of analysis along the eigenvectors proportionally to the eigenvalues. When deforming the volume of analysis we keep the longest axis equal to R_{200}. After the deformation of the original spherical region, **I** is calculated once again, but now making use of the newly determined s and q, and only considering the particles within the new ellipsoidal region. The iterative process is repeated until convergence is achieved, i.e. until the variance in both axial ratios, s and q, is less than a given tolerance defined as (Schneider et al. [153])

$$\max\left[\frac{(q'-q)^2}{q^2}, \frac{(s'-s)^2}{s^2}\right] < 5 \times 10^{-3}. \tag{3.3}$$

We have also made use of the concept of triaxiality, characterizing it by means of the triaxiality parameter

$$T \equiv \frac{a^2 - b^2}{a^2 - c^2} = \frac{1 - q^2}{1 - s^2}\ . \tag{3.4}$$

An ellipsoid is considered oblate if $0<T<1/3$, triaxial with $1/3<T<2/3$, and prolate if $2/3<T<1$.

Preprints (www.preprints.org) | NOT PEER-REVIEWED | Posted: 22 March 2023 doi:10.20944/preprints202303.0387.v1

3.2 The shapes

This kind of analysis is usually performed with halos from simulations with high mass resolution (e.g. 6.885×10^6 in Schneider et al. [153]), or halos "extracted" from low mass resolution simulations and then resimulated with a higher resolution. They are also selected in order to conform an homogeneous population, with selection criteria such as: dynamic equilibrium or number of particles within R_{200}. Therefore, MICE simulation is not the best choice if we want to extract solid conclusions about the shape of dark matter halos. However, as our analysis shows, it is a useful tool if we want a statistical estimation of the average shape of the different samples, and also of the evolution in redshift of the shape.

The number of particles within R_{200} ranges from 150 to 4000, so we only deem reliable the statistics from the two most massive halo samples (M3 and M4). Nonetheless, we present the results for all the mass samples in order to get a bigger picture. Table 3.1 shows the redshift distribution of halos from the different samples.

		Number of halos			
	Redshift	M1	M2	M3	M4
Z1	[0.0,0.1]	996	472	200	75
Z2	[0.1,0.2]	5298	2402	929	331
Z3	[0.2,0.3]	10529	4411	1678	472
Z4	[0.3,0.4]	14533	5548	1889	551
Z5	[0.4,0.5]	15850	5909	1790	401
Z6	[0.5,0.6]	14895	5066	1445	265
Z7	[0.6,0.7]	12510	3851	987	162
Z8	[0.7,0.8]	9476	2772	568	76
Z9	[0.8,0.9]	6780	1656	305	42
Z10	[0.9,0.993]	4095	901	142	8

Table 3.1: Number of halos per mass and redshift. Mass samples are defined in Table 2.2

Preprints (www.preprints.org) | NOT PEER-REVIEWED | Posted: 22 March 2023 doi:10.20944/preprints202303.0387.v1

Figs. 3.2, 3.3 and 3.4 show the percentage of prolate, triaxial and oblate halos for all the mass samples (M1, M2, M3, M4) in terms of their redshift. We find a clear trend regarding the triaxiality: the percentage of prolate halos grows with the mass; a trend that reverses for the triaxial and oblate cases. In the last two redshift bins the population of the sample M4 is very small, hence producing non-reliable results.

We also find that for a given mass sample, the lower the redshift, the higher is the percentage of triaxial halos; this can be clearly seen in Fig. 3.5. Again, high-redshift bins are vey biased, particularly for the most massive samples (M3 and M4), but the trend is very clear. Fig. 3.5 also shows that most of the halos are ellipsoidal (prolate or oblate), since the percentage of triaxial halos is never higher than 47% in any sample, and that the number of ellipsoidal halos grows with the mass of the sample.

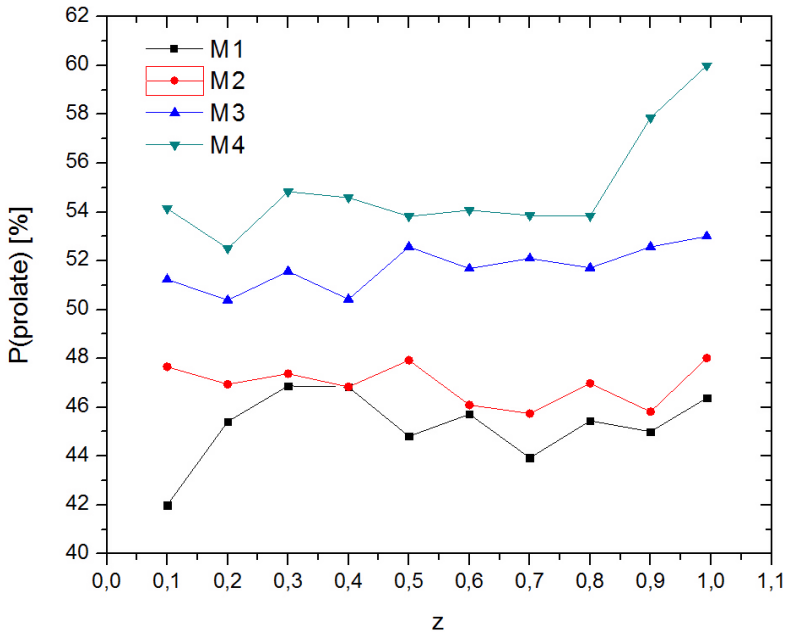

Figure 3.2: Percentage of prolate halos in terms of redshift for all the mass samples.

Preprints (www.preprints.org) | NOT PEER-REVIEWED | Posted: 22 March 2023 doi:10.20944/preprints202303.0387.v1

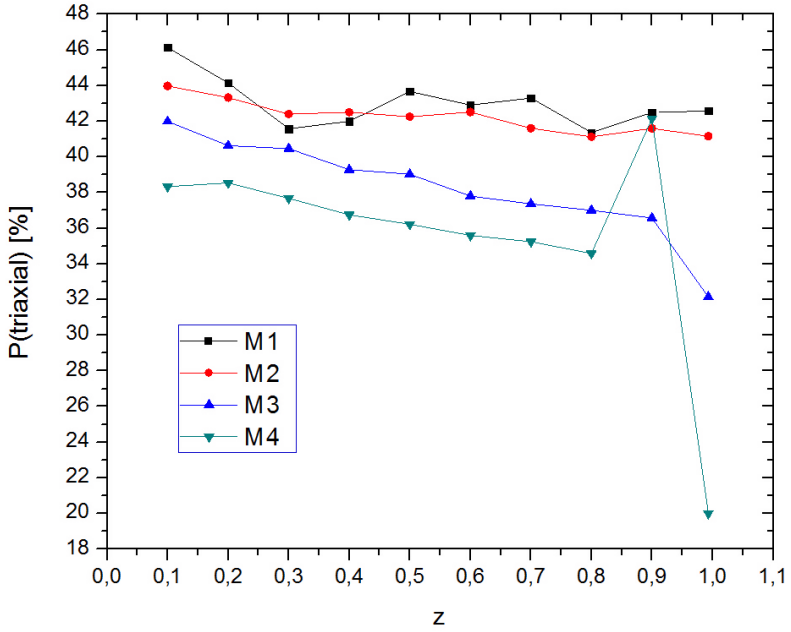

Figure 3.3: Percentage of triaxial halos in terms of redshift for all the mass samples.

3.3 Conclusions

Despite the low mass resolution of the MICE simulation, our analysis shows that a statistical trend exists. The shape statistics here illustrated is in very good agreement with e.g. Allgood et al. [2], Shaw et al. [159], and Muñoz-Cuartas et al. [125], showing that prolateness dominates over all epochs, that most massive halos are more prolate, and that for a given mass low-redshift halos are more triaxial.

Our goals in this chapter cannot be very ambitious, but the results have proved very useful in our posterior analysis of the effects of correlated structure in the mass calibration (see §5).

Preprints (www.preprints.org) | NOT PEER-REVIEWED | Posted: 22 March 2023 doi:10.20944/preprints202303.0387.v1

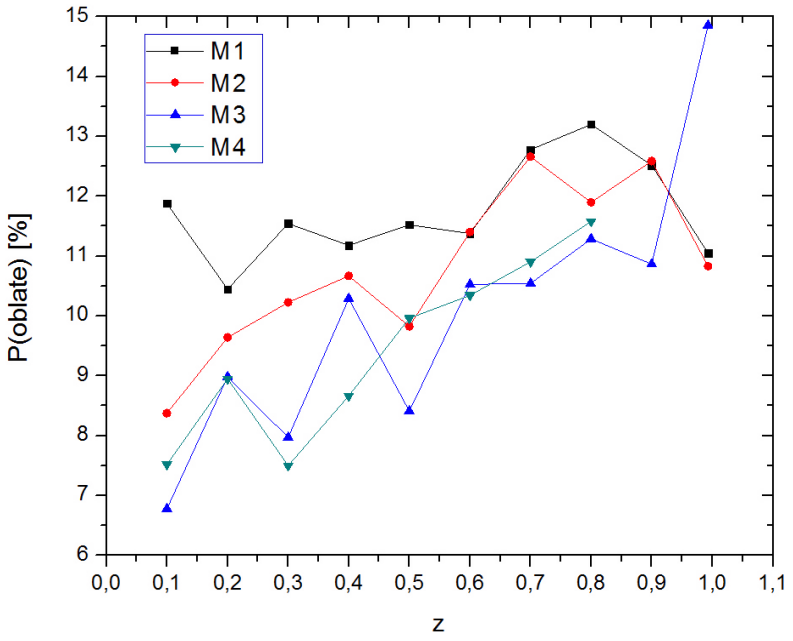

Figure 3.4: Percentage of oblate halos in terms of redshift for all the mass samples.

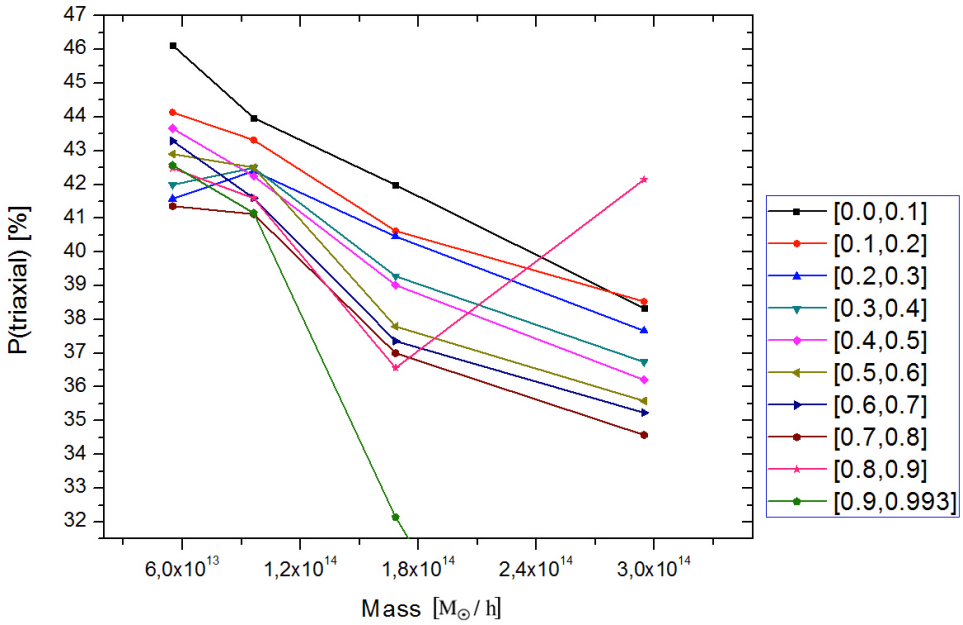

Figure 3.5: Evolution in redshift of the percentage of triaxial halos for every mass sample.

 doi:10.20944/preprints202303.0387.v1

Chapter 4

All Sky Shear and Flexion Maps

"Nature uses only the longest threads to weave her patterns, so that each small piece of her fabric reveals the organization of the entire tapestry."

Richard P. Feynman

4.1 Flexion Maps

Flexion is a gravitational lensing effect that goes with the third-order derivative of the deflection potential. It is, therefore, a weak effect that arises when shear and convergence vary significantly over the scale of the observed image. The lens equation, considered linear in previous chapters, must be expanded in this case to second order (Munshi et al. [126]) :

$$\beta_i \simeq A_{ij}\theta_j + \frac{1}{2}D_{ijk}\theta_j\theta_k \tag{4.1}$$

with

$$D_{ijk} = \partial_k A_{ij}. \tag{4.2}$$

The distortions thus described by flexion consist on the bending of the galaxy image. Measurements of gravitational flexion are very useful in the detection and characterization of

Preprints (www.preprints.org) | NOT PEER-REVIEWED | Posted: 22 March 2023 doi:10.20944/preprints202303.0387.v1

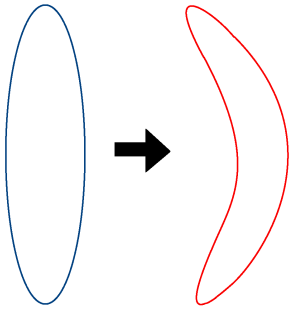

Figure 4.1: Flexion effect in a galaxy image.

the profiles of substructures within clusters of galaxies [112, 111, 132, 133] . Besides, Lasky and Fluke [107] have found that first and second flexion are sensible to the type of density profile and the concentration of the NFW profile respectively. It is therefore interesting to build all sky flexion maps in order to allow forthcoming flexion and joint shear-flexion analysis [51, 180] of the MICE simulations. As the Born approximation results to be a good approximation for flexion calculation [152], MICE lensing maps can be used to build all sky flexion maps.

4.1.1 All-sky formalism for flexion

Spherical harmonics form a complete set of orthonormal functions, and then, a vector space analogous to unit basis vectors. On the unit sphere, any square-integrable function can thus be expanded as a linear combination of these:

$$f(\theta,\varphi) = \sum_{l=0}^{\infty} \sum_{m=-l}^{l} f_l^m Y_l^m(\theta,\varphi). \tag{4.3}$$

We have to deal with spin-weighted (s) objects so the appropriate basis is, in this case, a similar set of functions defined on the sphere, called spin-weighted spherical harmonics ${}_sY_{lm}(\theta,\varphi)$, defined as [90]

$${}_sY_{lm}(\theta,\varphi) = \sqrt{\frac{(2l+1)}{4\pi}} D^l_{-s,m}(\varphi,\theta,0) \tag{4.4}$$

where D is the Wigner-D function, a rotation matrix

Preprints (www.preprints.org) | NOT PEER-REVIEWED | Posted: 22 March 2023 doi:10.20944/preprints202303.0387.v1

$$D^{l}_{-s,m}(\varphi,\theta,\psi)=\sqrt{\frac{4\pi}{(2l+1)}}({}_{s}Y_{lm}(\theta,\varphi))e^{-is\psi} \tag{4.5}$$

representing rotations by the Euler angles (φ,θ,ψ).

First and second flexion can be expressed in terms of convergence (κ) and shear (γ) [9] [1]

$$\mathcal{F}=|\mathcal{F}|\,e^{i\phi}=\frac{1}{2}\eth\bar{\eth}\eth\psi=\eth\kappa=\bar{\eth}\gamma, \tag{4.6}$$

$$\mathcal{G}=|\mathcal{G}|\,e^{i3\phi}=\frac{1}{2}\eth\eth\eth\psi=\eth\gamma, \tag{4.7}$$

where $\eth$ is a complex derivative operator defined, for a flat sky, as

$$\eth\ {}_{s}f(x,y)=-(\partial_x+i\partial_y){}_{s}f(x,y)\ . \tag{4.8}$$

Thus defined, ∂ can be interpreted as a spin-raising operator, and its complex conjugate

$$\bar{\eth}\ {}_{s}f(x,y)=-(\partial_x-i\partial_y){}_{s}f(x,y)\ ,$$

as a spin-lowering operator. The two-dimensional Laplacian can be easily defined as the application of one after the other,

$$\eth\bar{\eth}=\bar{\eth}\eth\ . \tag{4.9}$$

Since we are working on a two-dimensional sphere (full-sky), these operators need to be redefined in order to raise and lower the angular spin-s field ${}_{s}f(\theta,\varphi)$ [31]

$$\begin{aligned}\eth\ {}_{s}f(\theta,\varphi) &= -(\partial_\theta+i\csc\theta\partial_\varphi-s\cot\theta){}_{s}f(\theta,\varphi)\\ &= -\sin^{s}\theta(\partial_\theta+i\csc\theta\partial_\varphi)\sin^{-s}\theta\,{}_{s}f(\theta,\varphi)\ ,\end{aligned} \tag{4.10}$$

$$\begin{aligned}\bar{\eth}\ {}_{s}f(\theta,\varphi) &= -(\partial_\theta-i\csc\theta\partial_\varphi+s\cot\theta){}_{s}f(\theta,\varphi)\\ &= -\sin^{-s}\theta(\partial_\theta-i\csc\theta\partial_\varphi)\sin^{s}\theta\,{}_{s}f(\theta,\varphi)\ .\end{aligned} \tag{4.11}$$

[1] In the next two equations ϕ represents the position angle determining the direction of the vector or spin-3 component. And ψ is the gravitational potential.

Preprints (www.preprints.org) | NOT PEER-REVIEWED | Posted: 22 March 2023 doi:10.20944/preprints202303.0387.v1

Making use of the latter we can find the expressions for first and second flexions in a 2D spherical full-sky

$$\mathcal{F}(\mathbf{r}) = \mathcal{F}(r,\theta,\varphi) = -\frac{1}{6}\left(\bar{\eth}\eth\eth + \eth\bar{\eth}\eth + \eth\eth\bar{\eth}\right)\phi(r,\theta,\varphi) \ , \tag{4.12}$$

$$\mathcal{G}(\mathbf{r}) = \mathcal{G}(r,\theta,\varphi) = -\frac{1}{2}\eth\eth\eth\phi(r,\theta,\varphi) \ . \tag{4.13}$$

and then expand them in terms of the spherical harmonics (spin-0 spherical harmonics, since gravitational potential is a scalar)

$$\mathcal{F} = -\frac{1}{6}\left(\bar{\eth}\eth\eth + \eth\bar{\eth}\eth + \eth\eth\bar{\eth}\right)\phi_{lm}\ {}_0Y_{lm} \ , \tag{4.14}$$

$$\mathcal{G} = -\frac{1}{2}\eth\eth\eth\phi_{lm}\ {}_0Y_{lm} \ . \tag{4.15}$$

Defining now some useful properties of these raising and lowering operators

$$\eth\ {}_sY_{lm} = [(l-s)(l+s+1)]^{\frac{1}{2}}\ {}_{s+1}Y_{lm} \ , \tag{4.16}$$

$$\bar{\eth}\ {}_sY_{lm} = -[(l+s)(l-s+1)]^{\frac{1}{2}}\ {}_{s-1}Y_{lm} \ , \tag{4.17}$$

$$\bar{\eth}\eth\ {}_sY_{lm} = -(l-s)(l+s+1)\ {}_sY_{lm} \ , \tag{4.18}$$

$$\eth\bar{\eth}\ {}_sY_{lm} = -(l+s)(l-s+1)\ {}_sY_{lm} \ , \tag{4.19}$$

we can rewrite equations 4.14 and 4.15 as

$$\mathcal{F} = \frac{1}{6}\left[l\,(l+1)\right]^{\frac{1}{2}}\left\{\left[(l-1)\,(l+2)\right] + 2\left[l\,(l+1)\right]\right\}\phi_{lm}\ {}_1Y_{lm} \ , \tag{4.20}$$

$$\mathcal{G} = \frac{1}{2}\left[(l-2)\,(l-1)\,l\,(l+1)\,(l+2)\,(l+3)\right]^{\frac{1}{2}}\phi_{lm}\ {}_3Y_{lm} \ . \tag{4.21}$$

Considering we are planning to build the flexion maps from the preexistent MICE convergence maps, it is necessary to formulate both first ($\mathcal{F}$) and second flexion ($\mathcal{G}$) in terms of the

Preprints (www.preprints.org) | NOT PEER-REVIEWED | Posted: 22 March 2023 doi:10.20944/preprints202303.0387.v1

convergence. Taking into account the relation between κ and the potential [31]

$$\kappa(\mathbf{r}) = \frac{1}{4}\left[\eth\overline{\eth} + \overline{\eth}\eth\right]\phi(\mathbf{r}) \ , \tag{4.22}$$

and then using the relations given in equations 4.16 to 4.19, we can write

$$\kappa = -\frac{1}{2}\sum_{l=1}^{\infty}\sum_{m=-l}^{l} l\,(l+1)\,\phi_{lm}\,{}_0Y_{lm} \ . \tag{4.23}$$

Defining the convergence coefficients as

$$\kappa_{lm} = -\frac{1}{2} l\,(l+1)\,\phi_{lm} \tag{4.24}$$

the desired relations appear straightforward

$$\mathcal{F}_{lm} = -\frac{1}{3}\frac{\kappa_{lm}}{\left[l\,(l+1)\right]^{\frac{1}{2}}}\left\{\left[(l-1)\,(l+2)\right] + 2\left[l\,(l+1)\right]\right\} \ , \tag{4.25}$$

$$\mathcal{G}_{lm} = -\kappa_{lm}\left[\frac{(l-2)\,(l-1)\,(l+2)\,(l+3)}{l(l+1)}\right]^{\frac{1}{2}} \ . \tag{4.26}$$

4.1.2 Generating the flexion maps

To obtain the first and second flexion maps we are using the convergence Healpix maps built from MICE simulations ($\Omega_M = 0.25, \Omega_\Lambda = 0.75, \sigma_8 = 0.8, n_S = 0.95, h = 0.7$). In this case a light-cone simulation with 2048^3 particles in a box of side L=3072 Mpc/h, and with all sources fixed at z=0.993. We are making use of three different healpix resolutions[2] in order to test pixelization effects and determine which one is the most appropriate for ulterior analyses.

[2] Healpix pixel size is the square root of its uniform surface area, and it's given by the expression pixel_size=$\sqrt{\frac{3}{\pi}}\frac{3600}{Nside}$.

Preprints (www.preprints.org) | NOT PEER-REVIEWED | Posted: 22 March 2023 doi:10.20944/preprints202303.0387.v1

Nside	Pixel size [arcmins]
1024	3.4355
2048	1.7177
8192	0.4294

Table 4.1: Flexion maps resolution

Convergence coefficients can be obtained using Healpix *anafast* routine, designed to extract them out of the map. Once obtained, we can convert those into first and second flexion coefficients making use of equations 4.25 and 4.26 respectively. What we need next is the appropriate spherical harmonic basis in each case, ${}_1Y_{lm}$ for the $\mathcal{F}_{lm}$'s and ${}_3Y_{lm}$ for the $\mathcal{G}_{lm}$'s, in order to calculate flexion values in every pixel p. This can be done using the Healpix *alm2map_spin* routine, which produces maps of arbitrary spin s and -s given their fourier coefficients. A complex map S of spin s can be expressed as a linear combination of the spin weighted harmonics ${}_sY_{lm}$

$$ {}_sS(p) = \sum_{lm} {}_sa_{lm}\ {}_sY_{lm}(p) \tag{4.27} $$

for l$\geq |m|$, l$\geq |s|$,such that ${}_sS^* =_{-s} S$.

The outputs of this routine are two real maps ${}_sS^+$ and ${}_sS^-$ defined respectively as

$$ {}_{|s|}S^+ = \left({}_{|s|}S +_{-|s|} S\right)/2 \tag{4.28} $$

$$ {}_{|s|}S^- = \left({}_{|s|}S -_{-|s|} S\right)/(2i)\ . \tag{4.29} $$

So defined, ${}_1S^+$ and ${}_1S^-$ are the two components of the first flexion $\mathcal{F}$ map, and similarly ${}_3S^+$ and ${}_3S^-$ the two components of the second flexion $\mathcal{G}$ map[3].

Finally, using the Healpix *write_TQU* routine is possible to generate a map incorporating convergence, as T (temperature), and both first (second) flexion components, ${}_1S^+$ and ${}_1S^-$ (${}_3S^+$ and ${}_3S^-$), as polarization parameters (Q,U).

[3] If we were working with CMB temperature ${}_2S^+$ and ${}_2S^-$ would match Stokes parameters Q and U. Whereas, if s=0, ${}_0S^+ = T$ (temperature) and ${}_0S^- = 0$.

Preprints (www.preprints.org) | NOT PEER-REVIEWED | Posted: 22 March 2023 doi:10.20944/preprints202303.0387.v1

4.1.3 Validation

In order to test the reliability of the generated maps we have checked the resulting power spectra. Defining the power spectrum of a field as

$$C_f(l) = \sum_{m=-l}^{l} a_{f,lm}\, a^*_{f,lm} / \ (2l+1)\,, \tag{4.30}$$

and according to equations 4.25 and 4.26, one can find the subsequent relation between convergence and first and second flexion power spectra,

$$C_{\mathcal{F}}\,(l) = \frac{1}{9}\left[\frac{9l^4+18l^3-3l^2-12l+4}{l^2+l}\right] C\kappa\,(l) \tag{4.31}$$

$$C_{\mathcal{G}}\,(l) = \left[\frac{l^4+2l^3-7l^2-8l+12}{l^2+l}\right] C\kappa\,(l)\,. \tag{4.32}$$

From the first flexion map we have extracted the Cl's of convergence (T), and the two components ${}_1S^+$ and ${}_1S^-$ (Q,U). Figure 4.2 shows the validity of eq. 4.31 and therefore of our flexion maps (regarding the validity of the convergence maps see section 5.1).

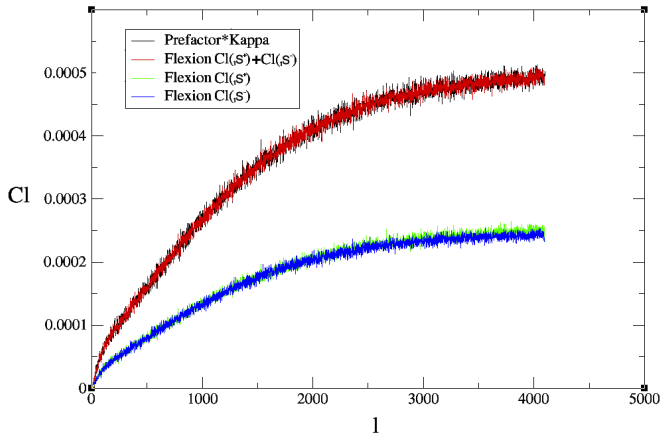

Figure 4.2: Validation of the relation between convergence and first flexion power spectra. Values calculated from eq. 4.31 (black) are in good agreement with the Cl's extracted from the generated map (red). The expression for the prefactor is $\frac{1}{9}\left[\frac{9l^4+18l^3-3l^2-12l+4}{l^2+l}\right]$.

Preprints (www.preprints.org) | NOT PEER-REVIEWED | Posted: 22 March 2023 doi:10.20944/preprints202303.0387.v1

The prefactors in equations 4.31 and 4.32 can be roughly reduced to l^2, as used by [9]. This concordance is quite good, except for the lowest multipoles.

First and second flexion prefactors appear identical for almost all the multipoles (figure 4.3), hence their power spectra are also identical at the scales of interest: small scales.

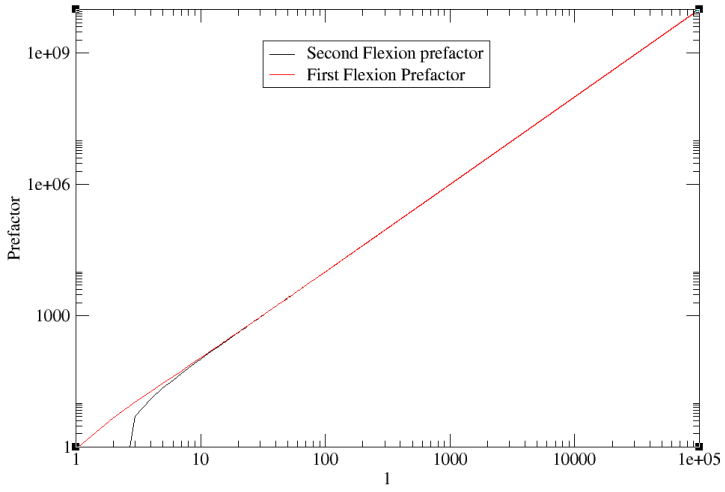

Figure 4.3: The power spectra of first and second flexion are equal for multipoles greater than l∼10.

In figure 4.4 we have compared the power spectra of first and second flexion. In order to study the pixelization effects we have also built flexion maps with a lower resolution (Nside=1024). The power spectrum analysis have been performed using a maximum multipole l_{max}=6143, although from l∼ 4096 (2Nside) on the PS values are not accurate.

Preprints (www.preprints.org) | NOT PEER-REVIEWED | Posted: 22 March 2023 doi:10.20944/preprints202303.0387.v1

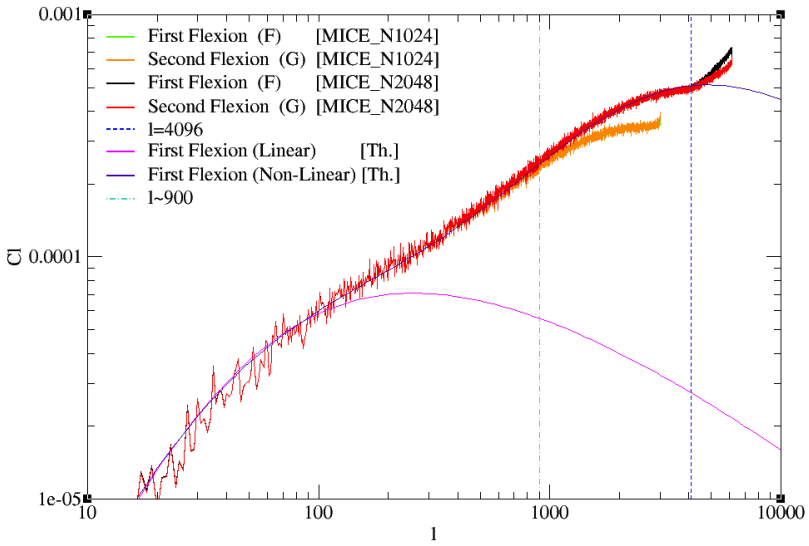

Figure 4.4: In red and black we show the two deconvolved power spectra corresponding to $\mathcal{F}$ and $\mathcal{G}$ respectively. Theoretical $\mathcal{F}$ linear and non-linear power spectra are shown in blue and violet.

Summarizing, we have successfully built three first and second flexion all-sky maps. First couple of maps (Nside=1024) have a very low pixel resolution, and they are not reliable at small scales, hence not useful for probing flexion regime (arcsecs). Next couple of flexion maps (Nside=2048) allow us to extend the analysis to almost the region where flexion power peaks, but they still have not enough resolution to be reliable. Finally, the maps with highest pixel resolution (Nside=8192) offer, a priori, the best alternative for the study of flexion, but at very small scales we find another issue, this time related with the shot noise (related to the mass resolution of the simulations). We find evidence of this fact when comparing the flexion power spectra from two different simulations, obtained from the same pixel resolution healpix maps. In Fig. 4.5 we show a comparison of the first flexion power spectra from MICE and Grand Challenge[4] simulations, the latter providing one order of magnitude better mass resolution. The simulation parameters for Grand Challenge are the same that those for MICE, except for the number of particles, thus permiting a fair comparison between the two spectra.

[4] Ω_m=0.25, Ω_Λ=0.75, Ω_b=0.044, n_S =0.95, σ_8=0.8 and h=0.7. Box size=3072 Mpc/h. Number of particles=4096^3.Particle mass=2.927x10^{10} $M_\odot$/h. Softening length=50 Kpc/h.

Preprints (www.preprints.org) | NOT PEER-REVIEWED | Posted: 22 March 2023 doi:10.20944/preprints202303.0387.v1

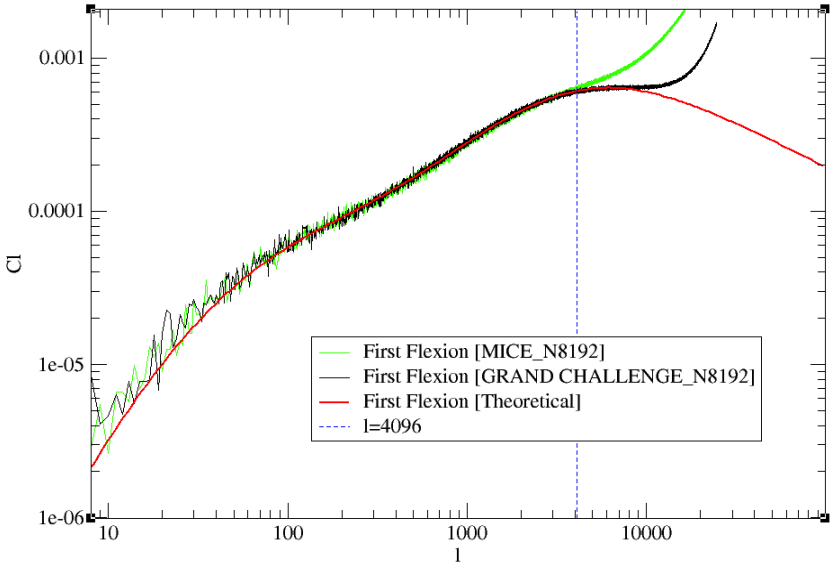

Figure 4.5: First flexion power spectra from MICE and Grand Challenge simulations. Both spectra were extracted from their respective healpix maps with Nside=8192.

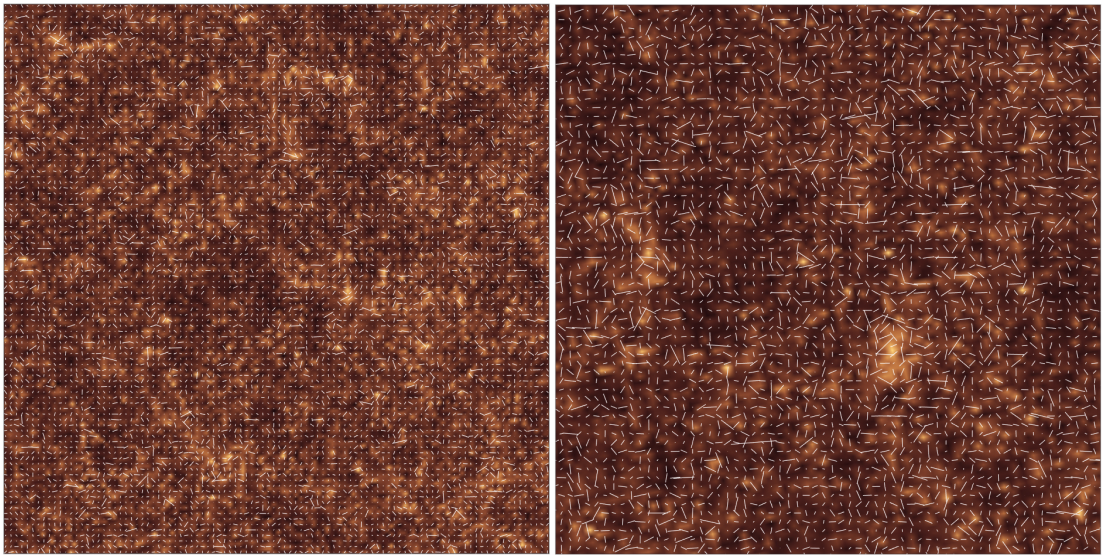

Figure 4.6: Two snapshots of the all-sky flexion maps of different angular sizes. The white lines represent the flexion magnitude and direction and they "point to" overdensities.

Preprints (www.preprints.org) | NOT PEER-REVIEWED | Posted: 22 March 2023 doi:10.20944/preprints202303.0387.v1

4.2 Shear Maps

All-sky simulations have an important role to play in reducing systematics [4], calibrating halo masses, performing joint analyses using magnification, shear and/or flexion [150], etcetera; being specially useful for studying large scale structure, since we are allowed to analyze a wider dynamical range of the dark matter density field [170]. Let's recall that twelve years ago, the first cosmic shear results were based on areas of just several square degrees [10, 100, 178, 185].

We are interested here in building reliable all-sky shear maps from the correspondent convergence maps generated from MICE simulations. For this purpose, and taking as reference the work by [58], we have built a projected density map of the lightcone output with sources located at z$\sim$1, and used the relation between convergence and shear in fourier space to generate the shear map. This is just an example to prove the validity of the new scripts, but the final pipeline enable us to generate shear maps with sources up to whatever of the MICE shell maps redshift, which means an asset for photometric surveys, and allows us to develop mock catalogs with angular shear information.

4.2.1 All-sky formalism for shear

As seen before in eq. 1.3, we can decompose the lensing potential into multipole moments

$$\phi(\theta,\varphi) = \sum_{l=0}^{\infty} \sum_{m=-l}^{l} \phi_l^m Y_l^m(\theta,\varphi). \tag{4.33}$$

The lensing potential is related to the convergence through eq 4.22, and to the shear through [31]

$$\gamma_1(\mathbf{r}) = \frac{1}{4}\left[\eth\eth + \overline{\eth}\overline{\eth}\right]\phi(\mathbf{r}), \tag{4.34}$$

$$\gamma_2(\mathbf{r}) = -\frac{i}{4}\left[\eth\eth - \overline{\eth}\overline{\eth}\right]\phi(\mathbf{r}) \tag{4.35}$$

Preprints (www.preprints.org) | NOT PEER-REVIEWED | Posted: 22 March 2023 doi:10.20944/preprints202303.0387.v1

which allow us, making use of the spin raising and lowering operators (eqs. 4.16, 4.17), to obtain the spherical harmonic expansion of the shear in terms of the lensing potential (Hu [88])

$$\gamma = \gamma_1 + i\gamma_2 = \frac{1}{2}\sum_{l=2}^{\infty}\sum_{m=-l}^{l}\sqrt{\frac{(l+2)!}{(l-2)!}}\phi_l^m \ {}_{\pm 2}Y_l^m. \tag{4.36}$$

We want to build the all-sky shear maps from the corresponding convergence maps, so we are interested in the relation between shear and convergence coefficients. We already know the expression for the convergence coefficients in terms of the lensing potential (eq. 4.24), whereas for the shear this relation can be expressed as

$$\gamma_{lm} = \frac{1}{2}\sqrt{\frac{(l+2)!}{(l-2)!}}\phi_l^m. \tag{4.37}$$

Combining both we find the desired relation

$$\gamma_{lm} = -\sqrt{\frac{(l+2)!}{(l-2)!}}\frac{\kappa_{lm}}{l(l+1)}. \tag{4.38}$$

4.2.2 Generating the shear maps

The methodology used to generate the shear maps is analogous to that described in section 3.1.2. We make use of the same lightcone simulation, and have all sources fixed at z=0.993. We extract the convergence coefficients with *anafast* and convert them into shear coefficients using eq.4.38. Since shear is a spin-2 field, the spherical harmonic basis will be in this case ${}_2Y_{lm}$. Making use of the aforementioned routine *alm2map_spin*, we obtain two real maps ${}_2S^+$ and ${}_2S^-$ (see eqs. 4.28 and 4.29), analogous to the Stokes parameters Q and U, which are the two components of the shear map. Finally, using the Healpix *write_TQU* routine is possible to generate a map incorporating convergence, as T (temperature), and both shear components, ${}_2S^+$ and ${}_2S^-$, as polarization parameters (Q,U).

Preprints (www.preprints.org) | NOT PEER-REVIEWED | Posted: 22 March 2023 doi:10.20944/preprints202303.0387.v1

4.2.3 Validation

Considering the Fourier transform of the convergence

$$\widehat{\kappa}\left(\mathbf{l}\right)=\int d^{2}\theta\ \exp\left[i\mathbf{l}\boldsymbol{\theta}\right]\kappa\left(\boldsymbol{\theta}\right) \tag{4.39}$$

then we can write

$$\langle\widehat{\kappa}\left(\mathbf{l}\right)\widehat{\kappa}^{*}\left(\mathbf{l}'\right)\rangle=\left(2\pi\right)^{2}\delta\left(\mathbf{l}-\mathbf{l}'\right)P_{\kappa}\left(l\right) \tag{4.40}$$

where $P_{\kappa}\left(l\right)$ is the power spectrum of the convergence. On the other hand, the relation between shear and convergence can be expressed as (Schneider [154])

$$\gamma\left(\boldsymbol{\theta}\right)=\frac{1}{\pi}\int_{\mathbb{R}^{2}}d^{2}\theta'\ D\left(\boldsymbol{\theta}-\boldsymbol{\theta}'\right)\ \kappa\left(\boldsymbol{\theta}'\right), \tag{4.41}$$

with

$$D\left(\boldsymbol{\theta}\right)=\frac{\theta_{1}^{2}-\theta_{2}^{2}+2i\theta_{1}\theta_{2}}{\left|\boldsymbol{\theta}\right|^{4}}=\frac{-1}{\left(\theta_{1}-i\theta_{2}\right)^{2}}\ . \tag{4.42}$$

In Fourier space eq. 4.41 can be rewritten as

$$\widehat{\gamma}\left(\mathbf{l}\right)=\frac{1}{\pi}\ \widehat{D}\left(\mathbf{l}\right)\ \widehat{\kappa}\left(\mathbf{l}\right)\quad\text{for }\mathbf{l}\neq\mathbf{0}\ , \tag{4.43}$$

where the Fourier transform of D is

$$\widehat{D}\left(\mathbf{l}\right)=\pi\frac{l_{1}^{2}-l_{2}^{2}+2il_{1}l_{2}}{\left|\mathbf{l}\right|^{2}}. \tag{4.44}$$

The Fourier transform of the shear is then

$$\widehat{\gamma}\left(\mathbf{l}\right)=\left(\frac{l_{1}^{2}-l_{2}^{2}+2il_{1}l_{2}}{\left|\mathbf{l}\right|^{2}}\right)\widehat{\kappa}\left(\mathbf{l}\right)=e^{i2\beta}\ \widehat{\kappa}\left(\mathbf{l}\right), \tag{4.45}$$

where β is the polar angle of the vector $\mathbf{l}$. This relation (eq. 4.45) implies that

$$\langle\widehat{\gamma}\left(\mathbf{l}\right)\widehat{\gamma}^{*}\left(\mathbf{l}'\right)\rangle=\left(2\pi\right)^{2}\delta\left(\mathbf{l}-\mathbf{l}'\right)P_{\kappa}\left(l\right). \tag{4.46}$$

Preprints (www.preprints.org) | NOT PEER-REVIEWED | Posted: 22 March 2023 doi:10.20944/preprints202303.0387.v1

Hence, we can conclude that the power spectrum of the shear is the same as that of the convergence.

Translating this result into the context of our maps, we can now validate the generated shear map, since we expect its power spectrum to be the same as that of the convergence map (regarding the validity of the convergence maps see section 5.1). Fig. 4.7 shows the good agreement between both spectra, which only differ at low multipoles. Additionally, we show also a visual check of the validity of the shear map (Fig. 4.8), where, as expected, E-mode shear is tangential to overdensities (lighter areas) and "points to" underdensities (darker areas).

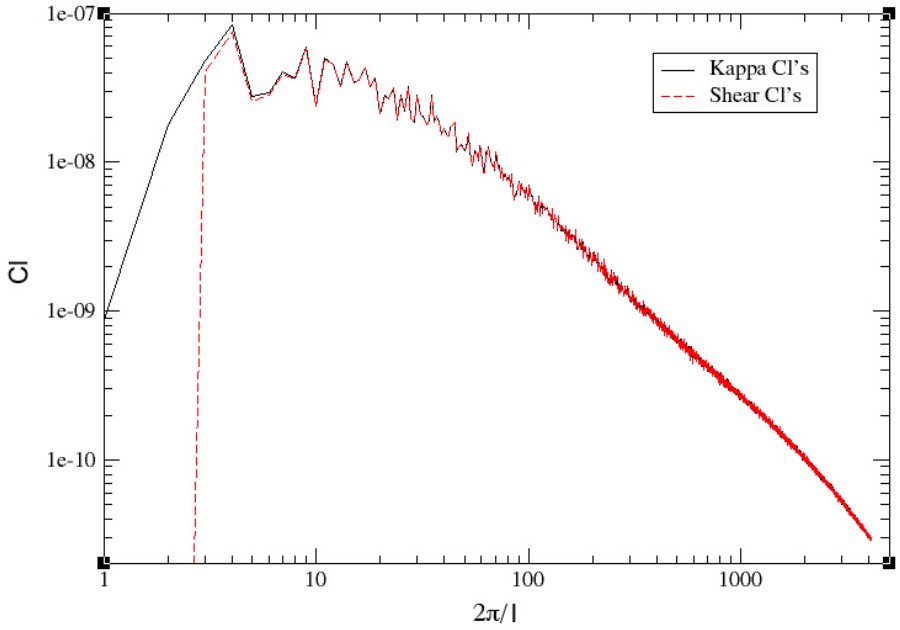

Figure 4.7: Comparison of convergence and shear power spectra from the Healpix maps. At $l \leq 2$ the power spectrum of the shear differs by definiton from that of the convergence (eq. 4.38)

 doi:10.20944/preprints202303.0387.v1

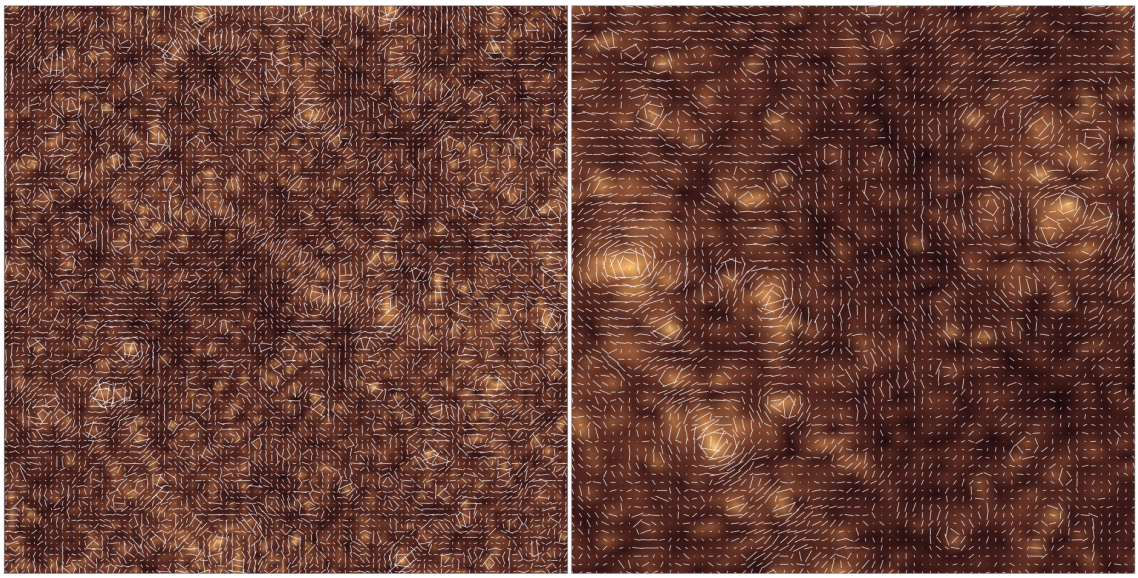

Figure 4.8: Two snapshots of the all-sky shear maps of different angular sizes. The white lines represent the shear magnitude and direction, and they are tangential to overdensities.

 doi:10.20944/preprints202303.0387.v1

Chapter 5

Weak Lensing Mass Calibration with All Sky Convergence Maps

"GRAVITATION, n. The tendency of all bodies to approach one another with a strength proportional to the quantity of matter they contain — the quantity of matter they contain being ascertained by the strength of their tendency to approach one another."

The Devil's Dictionary, Ambrose Bierce

The measurement of the mass in galaxy clusters is one of the hot topics in current research in Cosmology. It has indeed a wide variety of applications, such as constraining the equation of state of dark energy and the amplitude of mass fluctuations, the study of non-gaussianities, or the validation of cosmological and cluster formation models, among others. Gravitational lensing is by definition sensitive to the total mass, and is therefore one of the most promising methods to measure the mass profile independent of the dynamical state of the clusters. Many previous weak lensing analyses have focused on individual clusters (for example, Hoekstra [80]; Pedersen & Dahle [137]; Abate et al. [1]; Okabe et al. [131]). However, the measurement of the matter distribution of individual clusters can be quite noisy. Stacking the signal from many

Preprints (www.preprints.org) | NOT PEER-REVIEWED | Posted: 22 March 2023 doi:10.20944/preprints202303.0387.v1

clusters can mitigate this issue, since it allow us to average out the shape noise and the signal due to correlated structures. Such a statistical approach is thus advantageous if one is to compare the observations to theoretical predictions, which also average over a large number of halos in simulations.

5.1 All-Sky Convergence Maps

One way to map the dark matter structure, and consequently the mass distribution in a cluster, is to make use of a basic lensing quantity: convergence. This quantity is related to shear, the lensing observable, but also to surface-mass density, which is the line-of-sight projection of a three-dimensional matter density. A common approximation in the theory of weak lensing is the Born-approximation, in which one integrates the gravitational tidal field (weighted suitably for lensing) along a fiducial straight ray instead of the actual photon geodesic. This is a good approximation in the weak lensing regime, when the deflection of light is small (Hilbert et al. [78], Dodelson et al. [45], Shapiro and Cooray [158], Refregier [146], Fosalba et al. [58], Das & Bode [38], Teyssier et al. [171]). Under this assumption, the convergence is just a weighted projected surface density, this weight consisting of a geometric weighting function that involves relative distances, and can be expressed as

$$\kappa\left(\theta\right) = \frac{3H_0^2\Omega_m}{2c^2}\int dr\ \delta\left(r,\overrightarrow{\theta}\right)\frac{\left(r_s - r\right)r}{r_s\ a} \tag{5.1}$$

where δ is the three-dimensional matter density at radial distance r and angular position $\overrightarrow{\theta}$, and r_s is the radial position of the lensing sources.

Our weak lensing mass reconstruction makes use of the convergence maps generated by Fosalba et al. [58]. Those maps were built by just adding the onion slices from MICE simulation with the appropriate lensing weight. Equation 5.1 can be discretized, thus transforming an integral along the line of sight to a summation of matter density shells

$$\kappa\left(i\right) = \frac{3H_0^2\Omega_m}{2c^2}\sum_j \delta\left(i,j\right)\frac{\left(r_s - r_j\right)r_j}{r_s\ a_j}dr_j, \tag{5.2}$$

Preprints (www.preprints.org) | NOT PEER-REVIEWED | Posted: 22 March 2023 doi:10.20944/preprints202303.0387.v1

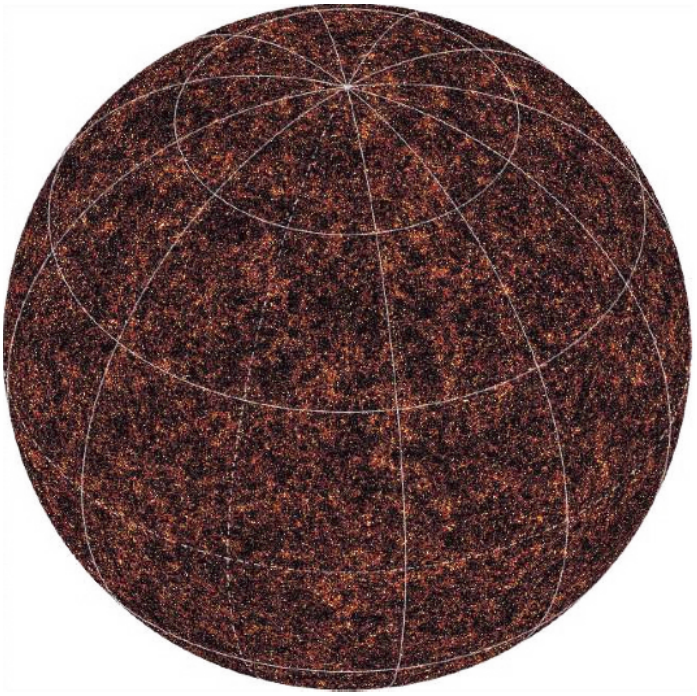

Figure 5.1: All-sky convergence map with sources at $z_s = 1$ (from Fosalba et al. [58]).

where i indicates a pixel position in the sky and j a radial bin (at distance r_j of width dr_j). The matter density contrast can then be written as

$$\delta(i,j) = \frac{\rho(i,j)}{\overline{\rho}} - 1 \tag{5.3}$$

where $\overline{\rho} = \langle \rho(i,j) \rangle$, and, indicating the number of particles in pixel i from slice j by N_{ij}, pixel density can be computed as

$$\rho(i,j) = \frac{N_{ij}}{dV_j} = \frac{N_{ij}}{\Delta\Omega\, r_j^2\, dr_j} \tag{5.4}$$

where $\Delta\Omega$ is the area of each pixel.

Considering the definition of convergence in eq. 5.1 we can write the angular power spectrum of the convergence as

$$C_l(\kappa) = \frac{9H_0^4\Omega_m^2}{4c^4} \int dr\; P(k,z)\, \frac{(r_s - r)^2}{r_s^2 a^2} \tag{5.5}$$

where P(k,z) is the 3D density power spectrum in the simulation at redshift z (corresponding to

Preprints (www.preprints.org) | NOT PEER-REVIEWED | Posted: 22 March 2023 doi:10.20944/preprints202303.0387.v1

the radial coordinate r = r(z) in the integral) evaluated at k = l/r in the small angle approximation, valid for l >10 within a few percent accuracy (see e.g.,Vale & White [177]). In terms of discrete shells, the power spectrum translates into:

$$C_l(\kappa) = \frac{9H_0^4\Omega_m^2}{4c^4} \sum_j dr_j P(l/r_j, z_j) \frac{(r_s - r_j)^2}{r_s^2 a_j^2} \tag{5.6}$$

Fig.5.2 shows a comparison of the predicted angular power spectrum (eq. 5.6) to the power spectrum directly measured from the convergence maps. The power spectrum has been binned in adjacent multipoles with bin-width $\Delta l = 20$. The errorbars indicate the scatter of power within a bin.

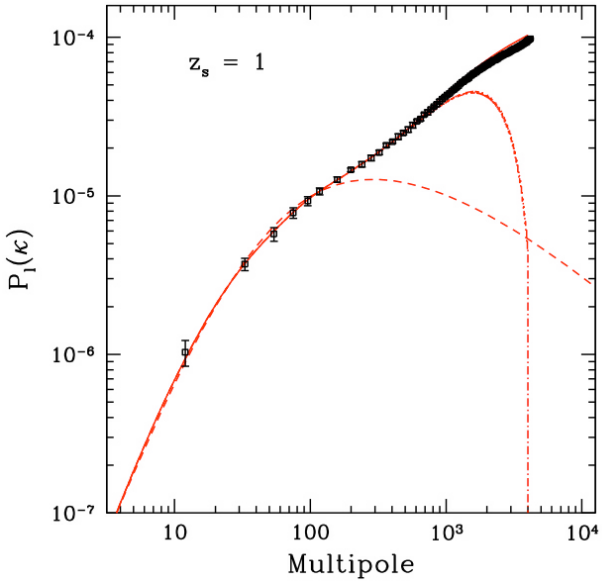

Figure 5.2: Angular power spectrum from the convergence maps (symbols with errorbars) as compared to linear theory (dashed line) and predictions from the full measured 3D power spectrum in eq. 5.5 (solid red line). The dot-dashed line uses the same prediction with the 3D power spectrum measured only using a 20483 particle-mesh (PM) grid. (Fosalba et al. [58])

All-sky convergence maps are created in the HEALPIX format with different Nside values (different pixel resolutions). For simplicity we will use a fixed source redshift $z_s = 1.0$ throughout our analysis.

Preprints (www.preprints.org) | NOT PEER-REVIEWED | Posted: 22 March 2023 doi:10.20944/preprints202303.0387.v1

5.2 Line-of-Sight Information: Uncorrelated Structure

In our effort to optimize the weak lensing mass estimates we have accounted for two different effects: those from uncorrelated and correlated structures. The first is addressed in this section, and the second in the next one.

The influence of uncorrelated structure on mas estimates can be answered for by constructing a filter to measure a known true profile. In our case we have assumed the smoothed NFW profiles (similar to Maturi et al. [123], and Dodelson [44]) studied in Section 2.6 as models for the spatial distribution of the signal, since they are a good approximation to MICE projected profiles

In order to assess how well we can recover the masses of the most massive halos (those that contribute the most to the convergence field (κ)) when there are no other halos in the same line-of-sight, we have designed a quite simple filter: we divide the projected halos into a central region (core), up to r_s, and an outer ring, from r_s to R_{200} (see Fig. 5.3).The projected angular distance (and therefore the projected density) is calculated using this expression:

$$\alpha = \text{acos}\left(\frac{(x_p x_h) + (y_p y_h) + (z_p z_h)}{\chi_p \chi_h}\right) \tag{5.7}$$

where (x_p, y_p, z_p) are the comoving coordinates of the particle, (x_h, y_h, z_h) are the comoving coordinates of the center of the halo, and χ_p and χ_h their corresponding comoving distances. However, for the sake of clarity, throughout this section we will be using r_s and R_{200} instead of α_s and α_{200} to denote the angular distances.

The estimate results from the sum of the signal of all the pixels within R_{200}, but we make this distinction because we expect our halos to mimic this configuration: a flat core that extends up to r_s, and an outer region (up to R_{200}) where the slope of the profile changes and density drops. This approach allows us not only to have an estimate of M_{200}, but also to differentiate the contribution of the core from that of the rest of the halo up to R_{200}, and to estimate whether their contributions are equal to those predicted by the corresponding smoothed NFW projected profile. For this filter, a pixel is considered to contribute to the core or the ring depending on whether its center is within r_s or between r_s and R_{200}.A halo is considered to lie in the line-of-sight of one of those halos if the projected separation between their centers is less than the sum

Preprints (www.preprints.org) | NOT PEER-REVIEWED | Posted: 22 March 2023 doi:10.20944/preprints202303.0387.v1

of their virial radii. This obviously requires knowledge of masses and positions of the line-of-sight halos.

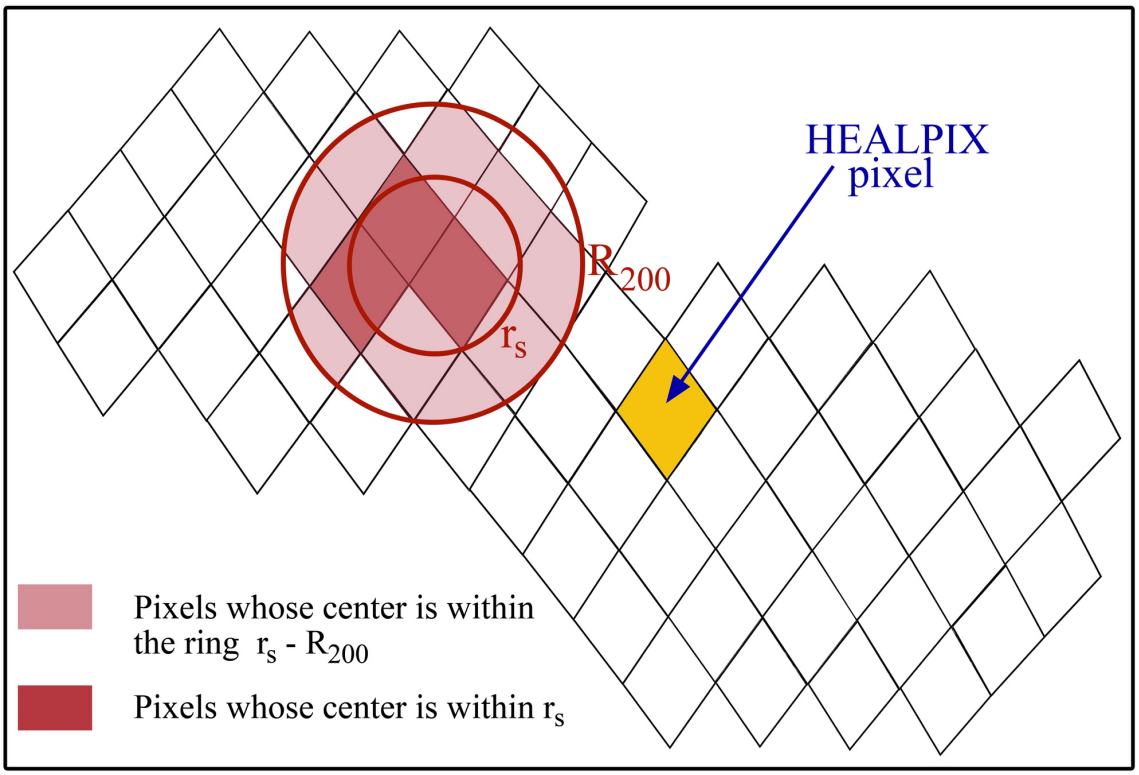

Figure 5.3: Setup of the filter. In red the filter used to study the effects of uncorrelated structure: we assume the smoothed NFW profile as true. We consider only those pixels whose center lies within the core or the ring.

To this end, and in order to mimic the set of line-of-sight halos that can be found in optical data, we have constructed two additional convergence maps that only show the contributions to the convergence field from halos with masses $M_{200} \geq 1.225 \times 10^{14}\ h^{-1}\ \mathbf{M}_{\odot}$ and $M_{200} \geq 2.143 \times 10^{14}\ h^{-1}\ \mathbf{M}_{\odot}$ respectively. The second mass threshold practically ensures that for each target halo the signal measured is purely from that halo, since there are only a few halos more massive than $3.751 \times 10^{14}\ h^{-1}\ \mathbf{M}_{\odot}$(the upper limit of the interval we have been studying), and we are working with an all-sky simulation; but this is not the case for the signal from the halos above the first mass threshold, which we expect to be affected by signal from the most massive halos. In Fig.5.4 we show three snapshots of the same field in the sky; the central and right

Preprints (www.preprints.org) | NOT PEER-REVIEWED | Posted: 22 March 2023 doi:10.20944/preprints202303.0387.v1

panels correspond to the additional convergence maps we have constructed, whereas the left panel corresponds to the convergence map with all the dark matter. As a measure for the mass enclosed within a pixel we use

$$\begin{aligned} M(i) &= [1+\delta\,(i,j)]\;\overline{\rho}\;dV_i \\ &= \left[1+\left(\frac{2}{3}\frac{c^2}{H_0^2\Omega_m}\kappa\,(i)\,\frac{r_s\;a_j}{(r_s-r_j)\,r_j\;dr_j}\right)\frac{N_j}{N_{pix}}m_p\right] \end{aligned} \tag{5.8}$$

where N_j is the number of particles in the slice j where the halo-lens is, N_{pix} is the number of pixels the sphere is divided into (all pixels have equal area), and m_p is the particle mass. This equation has been derived from eqs. 5.2, 5.3 and 5.4.

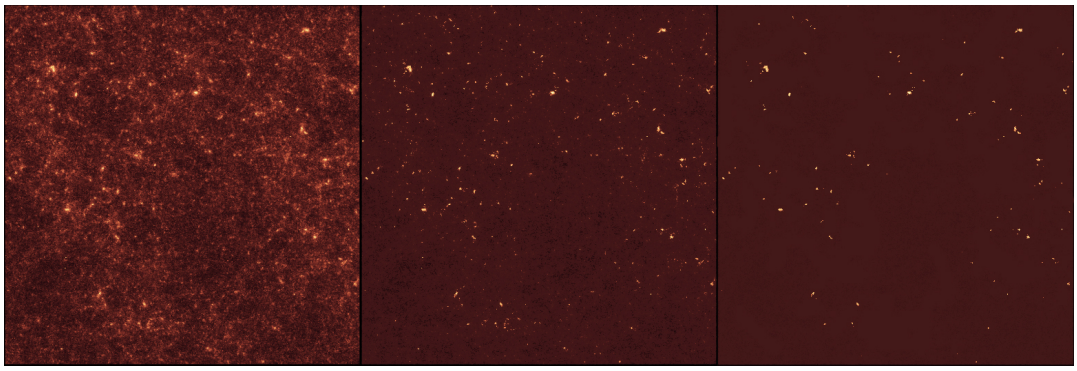

Figure 5.4: Convergence maps from different mass cuts. From left to right: all the particles, halos more massive than M_{200} =1.225×10^{14} h^{-1} $\mathbf{M}_{\odot}$, and halos more masive than M_{200} =2.143×10^{14} h^{-1} $\mathbf{M}_{\odot}$. The scale is between -4.276e-02 and 3.7e-01.

As a means to test our mass estimator, we have applied this filter to the convergence maps, and anlyzed the result for three different redshift bins: $[0.25, 0.35]\,, [0.45, 0.55]\,, [0.65, 0.75]$. The recovered mass of the halo can be expressed as

$$M_{recov} = \sum_i M(i) = \left[\sum_j M_{core}(j)\right] + \left[\sum_k M_{ring}(k)\right] \tag{5.9}$$

where j is the number of pixels whose center is within r_s, k is the number of pixels whose center is within the ring $r_s - R_{200}$, and $i = j + k$ is the total number of pixels used to recover the halo mass.

Preprints (www.preprints.org) | NOT PEER-REVIEWED | Posted: 22 March 2023 doi:10.20944/preprints202303.0387.v1

5.2.1 Intrinsic scatter

The results from the calibration are shown in Figs. 5.5 and 5.6 for the samples M3≡M_{200} $\in \left[1.225 \times 10^{14}, 2.143 \times 10^{14}\right]\ h^{-1}\ \mathbf{M}_{\odot}$ and M4≡M_{200} $\in \left[2.143 \times 10^{14}, 3.751 \times 10^{14}\right]\ h^{-1}\ \mathbf{M}_{\odot}$ respectively.

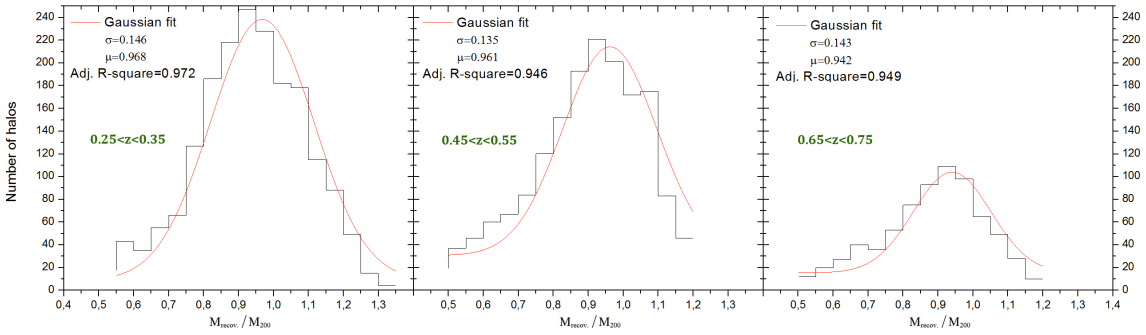

Figure 5.5: Scatter in mass estimates from κ with respect to the virial mass M_{200} for the sets of 1846, 1634 and 722 halos of M3 at the three different redshift bins. Line-of-sight projection has not been taken into account. These plots correspond to the convergence maps with a healpix resolution of Nside=8192, and we have only considered those pixels whose center is within R_{200}.

The scatters for the three halo sets of the first mass sample are quite similar $\sim 14\%$, while those of the second mass sample vary from 8 to 12%. Among other effects, the aforementioned contamination from the most massive halos is considered to contribute to the higher scatter observed in the first sample. These results obey to the fact that even correcting for the projection effects of all line-of-sight structure perfectly, we still have to cope with an "inherent scatter" related to the way we recover the mass. The enclosed mass within R_{200} may differ from M_{200} due to the variability of the halo profiles within one sample, and also due to the fact that density in the outer regions of MICE profiles does not rapidly decrease after R_{200}; thereby the signal from those regions contaminates the calibration. These two disrupting agents appear probably as a consequence of the correlated structure, since MICE halos are not isolated but embedded in greater structures.

As can be noted from Figs. 5.5 and 5.6, the mean of the distribution is consistently lower than 1, so we decided to include all the pixels within R_{200}. So far we have only considered those

Preprints (www.preprints.org) | NOT PEER-REVIEWED | Posted: 22 March 2023 doi:10.20944/preprints202303.0387.v1

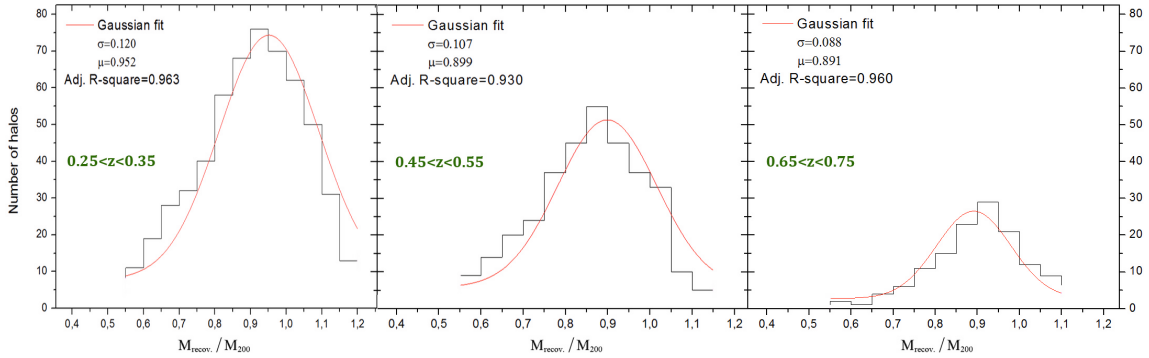

Figure 5.6: Scatter in mass estimates from κ with respect to the virial mass M_{200} for the sets of 564, 341 and 138 halos of M4 at the three different redshift bins. Line-of-sight projection has not been taken into account. These plots correspond to the convergence maps with a healpix resolution of Nside=8192, and we have only considered those pixels whose center is within R_{200}.

pixels whose center lies inside the filter, but if we include those partially within R_{200} (although its center is outside R_{200}) we find that the mean shifts to larger values closer to 1. The results from this new calibration are shown in Figs. 5.7 and 5.8. The scatters are similar to their corresponding counterparts resultant from the first calibration, but the distributions seem no longer biased, being now centered around the point where the recovered mass is almost equal to the virial mass.

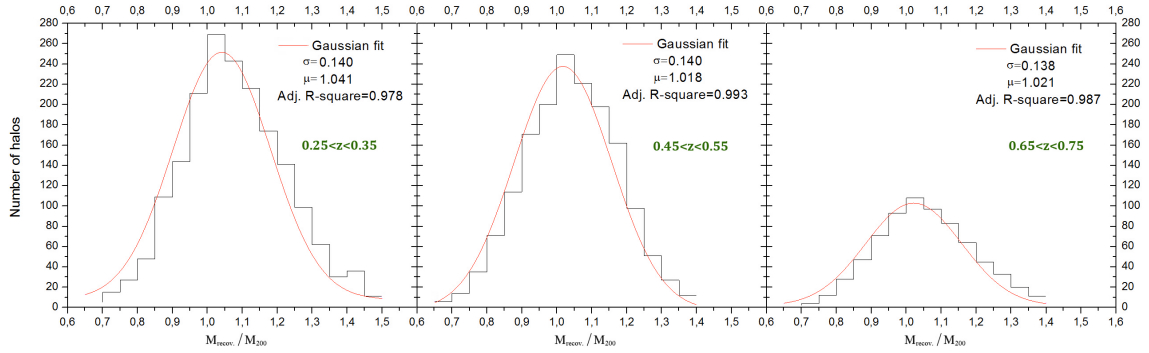

Figure 5.7: Scatter in mass estimates from κ with respect to the virial mass M_{200} for the three different sets of halos of the sample M3. These plots are the counterparts of those in Fig. 5.5, and correspond to the convergence maps with a healpix resolution of Nside=8192. Here we have considered all the pixels overlapped by the filter.

Preprints (www.preprints.org) | NOT PEER-REVIEWED | Posted: 22 March 2023 doi:10.20944/preprints202303.0387.v1

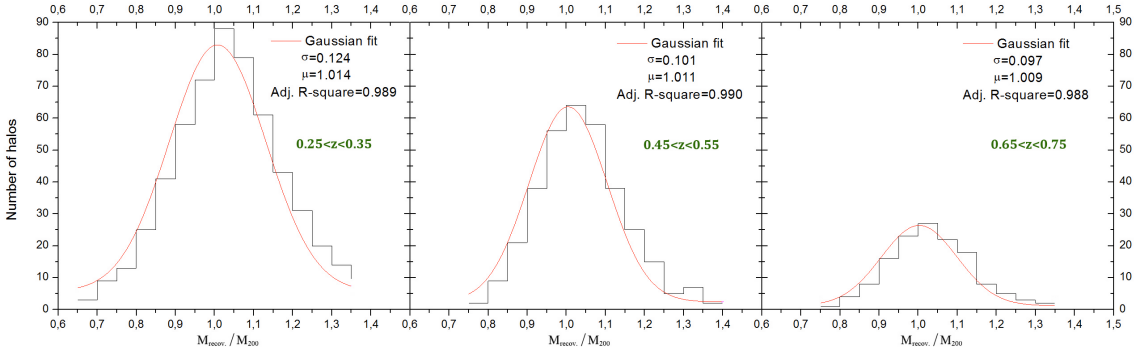

Figure 5.8: Scatter in mass estimates from κ with respect to the virial mass M_{200} for the three different sets of halos of the sample M4. These plots are the counterparts of those in Fig. 5.6 and correspond to the convergence maps with a healpix resolution of Nside=8192. Here we have considered all the pixels overlapped by the filter.

Modeling pixelization effects

This way of recovering the mass of the halos seems therefore dependent of the size of the pixel. In order to visualize this dependence we have performed the same calibrations (again considering all the pixels within R_{200} and not only those whose center is within the virial radius), but now making use of convergence maps with a healpix resolution of Nside=4096 (pixel area=0.859 arcmins). The results of the calibration with these maps (Figs. 5.9 and 5.10) show that the scatter is typically higher and the mean of each distribution is consistently greater than those from the maps with a healpix resolution of Nside=8192 (pixel area=0.429 arcmins) shown in Figs. 5.7 and 5.8. Therefore, we can conclude that the pixelization introduces additional statistical effects: scatter and bias. The scatter increase is of the order of 5-10% (although we find a case where the scatter shows almost no variation, and another one where the scatter increase is around 25%), while the increase of the mean of the distribution is of the order of the few percent.

Let us now check if we find the same trend when we consider only those pixels whose center is within the virial radius in the convergence maps with resolution Nside=4096. When we compare the results shown in Figs. 5.11 and 5.12 with those shown in Figs. 5.5 and 5.6, respectively, we find the same additional scatter and bias due to the pixelization.

Preprints (www.preprints.org) | NOT PEER-REVIEWED | Posted: 22 March 2023 doi:10.20944/preprints202303.0387.v1

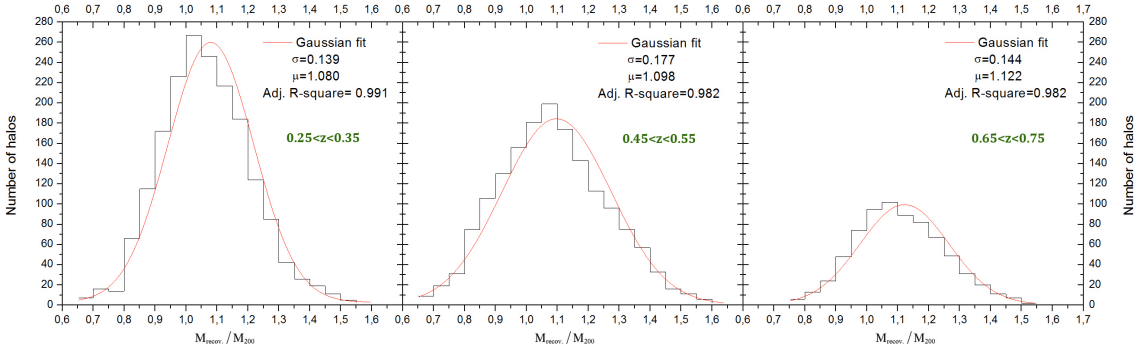

Figure 5.9: Scatter in mass estimates from κ with respect to the virial mass M_{200} for the three different sets of halos of the sample M3. These plots correspond to the convergence maps with a healpix resolution of Nside=4096, and we have considered all the pixels overlapped by the filter.

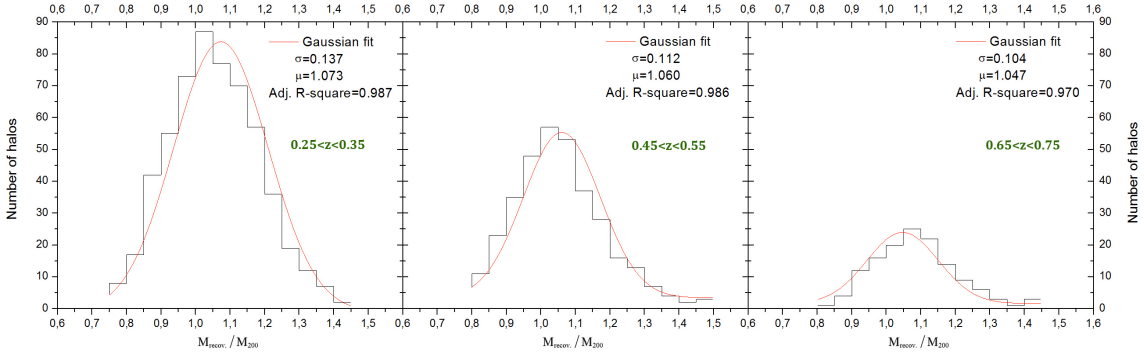

Figure 5.10: Scatter in mass estimates from κ with respect to the virial mass M_{200} for the three different sets of halos of the sample M4. These plots correspond to the convergence maps with a healpix resolution of Nside=4096, and we have considered all the pixels overlapped by the filter.

It is then clear that the contribution of the outer pixels (those whose center do not lie within R_{200} but are overlapped by the filter) is significant, and also that there is a bias associated with the resolution of the Healpix map. In order to model the impact of the pixelization in our mass calibration we have designed a weight function for the outer pixels . We chose for this purpose an linear function of the form

$$f(x) = a + b(x - R_{200}) \tag{5.10}$$

where x is the distance between the center of the pixel and the center of the halo. The values of a and b for pixels at $x > R_{200}$ have been calculated by fitting the data of the sample M4 with

Preprints (www.preprints.org) | NOT PEER-REVIEWED | Posted: 22 March 2023 doi:10.20944/preprints202303.0387.v1

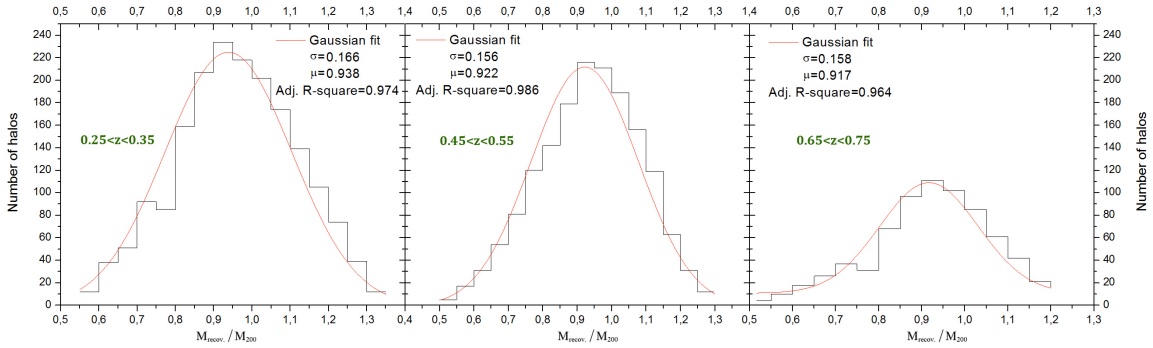

Figure 5.11: Scatter in mass estimates from κ with respect to the virial mass M_{200} for the three different sets of halos of the sample M3. These plots correspond to the convergence maps with a healpix resolution of Nside=4096, and we have only considered those pixels whose center is within R_{200}.

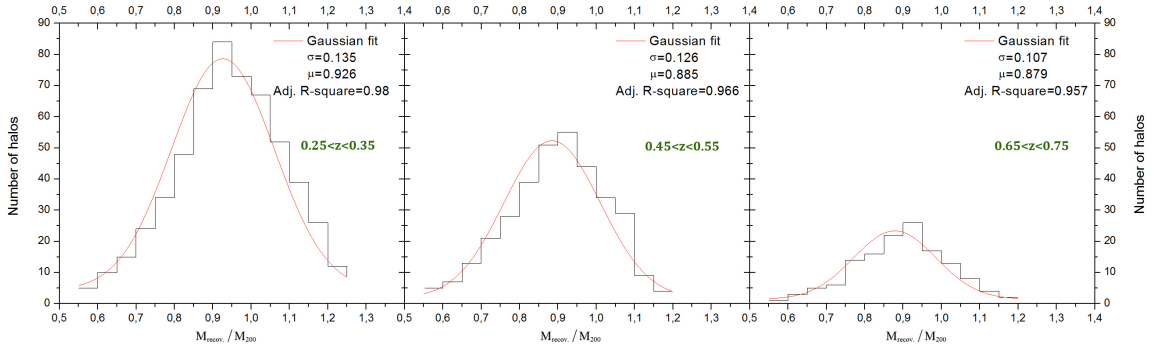

Figure 5.12: Scatter in mass estimates from κ with respect to the virial mass M_{200} for the three different sets of halos of the sample M4. These plots correspond to the convergence maps with a healpix resolution of Nside=4096, and we have only considered those pixels whose center is within R_{200}.

the convergence map of Nside=4096 in order to obtain an unbiased distribution (i.e. $\mu = 1$). The best-fit values of eq. 5.10 for each redshift are given in Table 5.1.

If we consider the average best-fit values of a and b, and use the weight function in the mass calibration, we find that the mean value of the distribution is now even closer to 1.0, and the scatter is similar to that in Figs. 5.9 and 5.10, or even decreases.

Preprints (www.preprints.org) | NOT PEER-REVIEWED | Posted: 22 March 2023 doi:10.20944/preprints202303.0387.v1

$\mathbf{M_{200}}$ (h^{-1} $\mathbf{M_\odot}$)	**Redshift**	**a**	**b**
M4	[0.25,0.35]	0.499±0.0019	-1.656±0.009
	[0.45,0.55]	0.504±0.0020	-1.677±0.010
	[0.65,0.75]	0.501±0.0023	-1.671±0.014

Table 5.1: Best fit parameters of the linear weight function. The y-intercept (a) is independent of the redshift, although this is not the case for the slope (b).

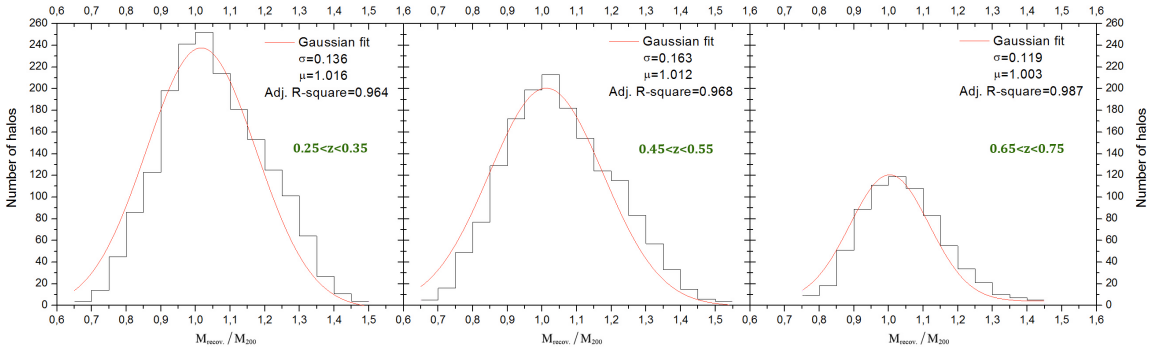

Figure 5.13: New estimates of the scatter in mass for the three different sets of halos of the sample M3. We are applying the weight function to the mass calibration. Convergence maps with Nside=4096.

Final Results

When we apply the weight function to the map with Nside=8192, whose resolution increases by a factor of 2 with respect to that with Nside=4096, we find that the slope (b) should be multiplied by the same factor. Figs. 5.15 and 5.16 show how the weight function affects the mass calibration with the highest resolution maps. Comparing these figures with Figs. 5.7 and 5.8, we observe that the bias decreases, i.e. the mean of the distribution is closer to 1.0, and again, as in the case of maps with Nside=4096, the scatter remains almost constant or even decreases.

Table 5.2 summarizes the results of this section. The weight function entails a significant improvement on the statistical indicators, and it allows us to perform our analysis in different resolution maps. We can generalize the weight function writing it as

$$f\,(x) = 0.501 - \frac{1.668}{4096}\ Nside\ \ (x - R_{200}) \tag{5.11}$$

and then minimize the impact of the pixelization in our calibration.

Preprints (www.preprints.org) | NOT PEER-REVIEWED | Posted: 22 March 2023 doi:10.20944/preprints202303.0387.v1

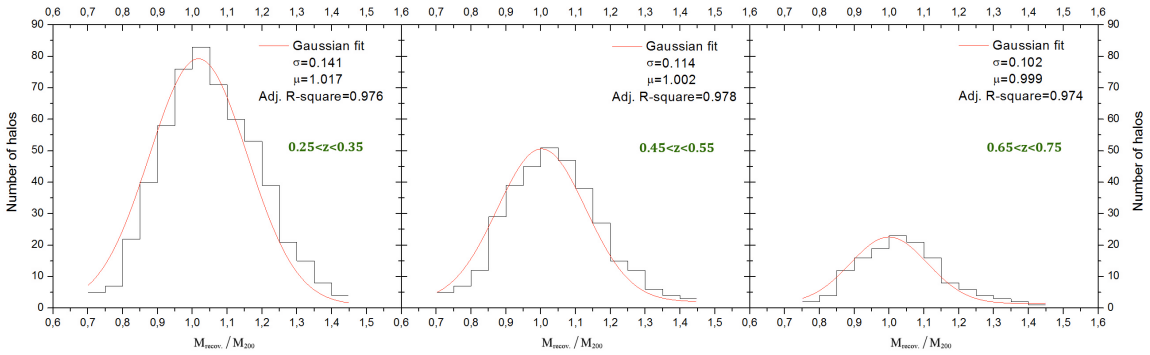

Figure 5.14: New estimates of the scatter in mass for the three different sets of halos of the sample M4. We are applying the weight function to the mass calibration. Convergence maps with Nside=4096.

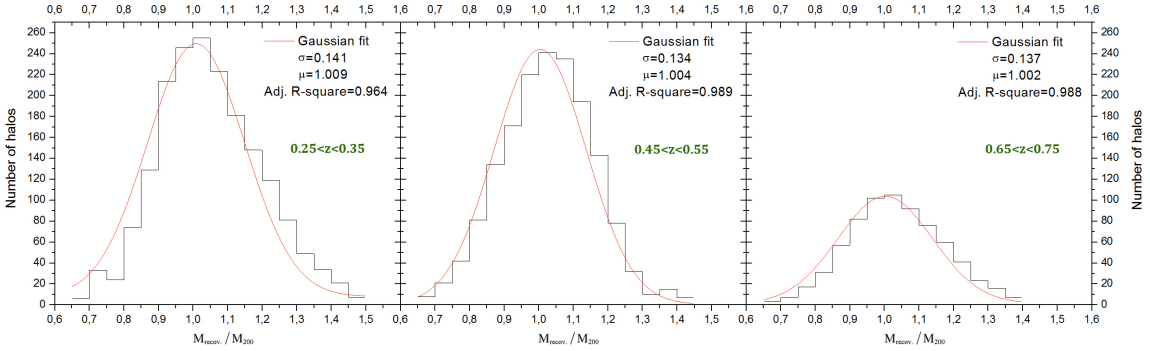

Figure 5.15: New estimates of the scatter in mass for the three different sets of halos of the sample M3. We are applying the weight function to the mass calibration. Convergence maps with Nside=8192.

5.2.2 Core versus radius contribution

We have also distinguished between the contributions of the core of the halo and the ring (ranging from r_s to R_{200}) to the convergence signal. It becomes clear, considering the results shown in Figs. 5.17 and 5.18, that the core of the density profiles introduces a greater scatter than the ring, an outcome that agrees with the fact that we are using an NFW-optimized filter, which assigns too much weight to the innermost regions of the halo (Gruen et al. [69]), thus making the mass recovery more sensitive to the variability of the profiles. Scatter in mass estimates of the core is systematically greater than that in mass estimates of the ring, although, for the core, the mean value of the distribution is generally closer to one than that observed in the case of the ring.

Preprints (www.preprints.org) | NOT PEER-REVIEWED | Posted: 22 March 2023 doi:10.20944/preprints202303.0387.v1

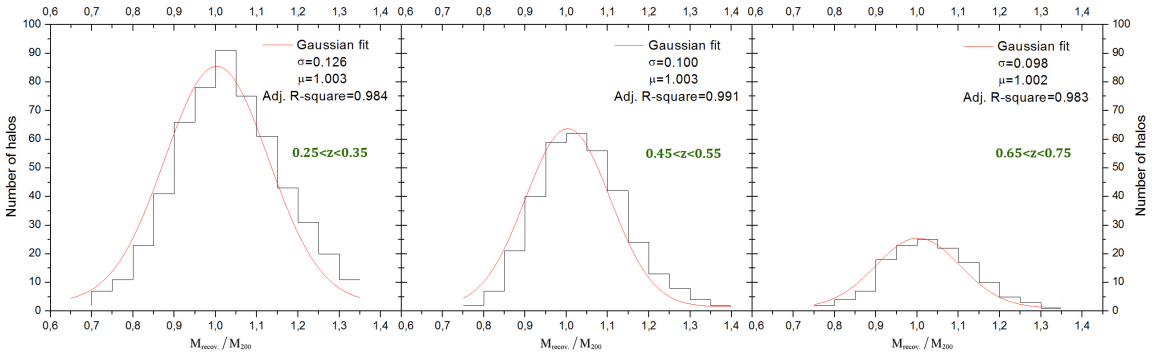

Figure 5.16: New estimates of the scatter in mass for the three different sets of halos of the sample M4. We are applying the weight function to the mass calibration. Convergence maps with Nside=8192.

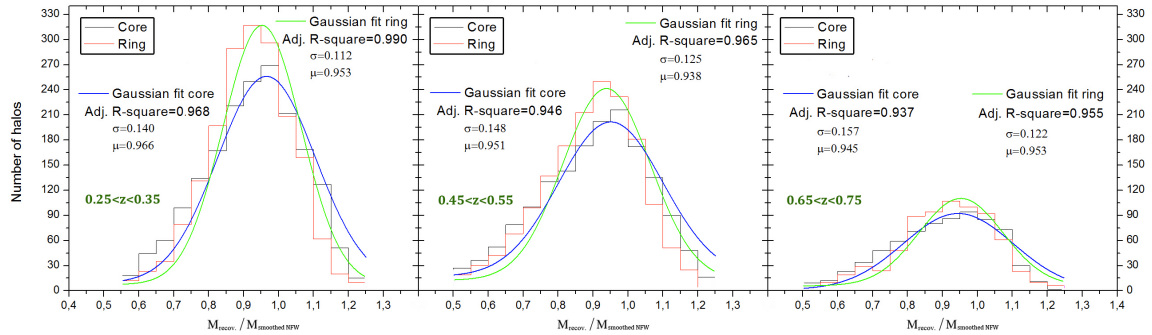

Figure 5.17: Scatter in mass estimates from κ_{core} and κ_{ring} with respect to the masses M_{core} and M_{ring}, caculated from the corresponding smoothed NFW profiles, for the sets of 1846, 1634 and 722 halos of sample M3.

Preprints (www.preprints.org) | NOT PEER-REVIEWED | Posted: 22 March 2023 doi:10.20944/preprints202303.0387.v1

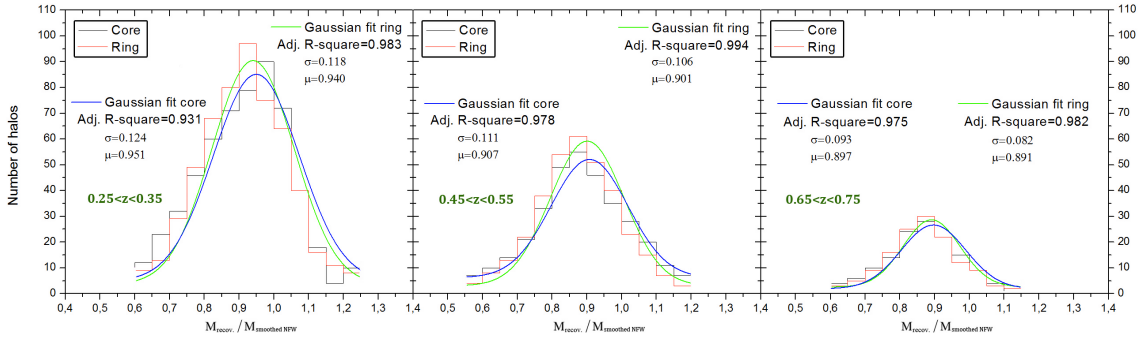

Figure 5.18: Scatter in mass estimates from κ_{core} and κ_{ring} with respect to the masses M_{core} and M_{ring}, caculated from the corresponding smoothed NFW profiles, for the sets of 564, 341 and 138 halos of sample M4.

		Nside=8192		Nside=8192		Nside=4096		Nside=4096	
		Weighted pixels		All pixels (no w.)		Weighted pixels		All pixels (no w.)	
$\mathbf{M_{200}}$ (h^{-1} $\mathbf{M_\odot}$)	**Redshift**	$\boldsymbol{\sigma}$	μ	σ	μ	$\boldsymbol{\sigma}$	$\boldsymbol{\mu}$	σ	μ
M3	[0.25,0.35]	0.141	1.009	0.140	1.041	0.136	1.016	0.139	1.080
	[0.45,0.55]	0.134	1.004	0.140	1.018	0.163	1.012	0.177	1.098
	[0.65,0.75]	0.137	1.002	0.138	1.021	0.119	1.003	0.144	1.122
M4	[0.25,0.35]	0.126	1.003	0.124	1.014	0.141	1.017	0.137	1.073
	[0.45,0.55]	0.100	1.003	0.101	1.011	0.114	1.002	0.112	1.060
	[0.65,0.75]	0.098	1.002	0.097	1.009	0.102	0.999	0.104	1.047

Table 5.2: Scatter and mean of the distributions resultant from the mass calibration. As we are only considering halos with masses above some specific mass thresholds (two different cases), these values represent the intrinsic scatter and bias of the samples M3 and M4.

 doi:10.20944/preprints202303.0387.v1

5.3 The Vicinity: Correlated Structure

Individual halos do not follow spherical NFW profiles. It is true that the average profile of a certain sample of dark matter halos, derived from simulations or weak lensing, is consistent with the NFW profile (Mandelbaum et al. [118], Johnston et al. [97]) although some works claim for small deviations in the core (Merritt et al. [124]) and in the outer regions. The fact that halos are aspherical (Warren et al. [183]) can lead to an overestimation of their masses if they are aligned with the line of sight, and an underestimation if aligned perpendicular to it. Additionally, dark matter halos contain substructure and are affected by correlated structure outside the virial radius, thus inducing variance in the profiles. All this effects can be grouped under the term *correlated structures*.

Our goal is not an "optimal filter" designed to minimize the variance between mass estimates and true M_{200}, but to analyze the influence of LOS orientation of the halos, and their shape variability, in lensing mass estimation. In order to do that we have made use of the previous study of dark matter halo shapes (see §5), investigating the correlation between the orientation of the halo with respect to the LOS ($\cos\theta$) and the deviation of its recovered mass from the true mass ($\mathrm{M}_{recov}/\mathrm{M}_{200}$). The correlation coefficient can be expressed as

$$r = \frac{\frac{1}{N_T}\sum_{i=1}^{N_T}\left(b_{M_i} - \overline{b_M}\right)\left(\cos\theta_i - \overline{\cos\theta}\right)}{\sigma_b\ \sigma_\theta} \tag{5.12}$$

where $b_M = M_{recov}/M_{200}$, N_T is the total number of halos in the sample, and

$$\sigma_b = \sqrt{\frac{1}{N_T}\sum_{i=1}^{N_T}\left(b_{M_i} - \overline{b_M}\right)^2} \tag{5.13}$$

$$\sigma_\theta = \sqrt{\frac{1}{N_T}\sum_{i=1}^{N_T}\left(\cos\theta_i - \overline{\cos\theta}\right)^2} \tag{5.14}$$

In Table 5.3 we show the correlation coefficients for the two halo mass samples of our interest at three different redshifts. These results reveal that there is a high correlation between the angle of the halo's major axis (θ) with respect to the LOS and the ratio of the estimated mass to the

$\mathbf{M_{200}}$ (h^{-1} $\mathbf{M_\odot}$)	Redshift	Halos	Correlation Coefficient
M3	[0.25,0.35]	1846	0.678
	[0.45,0.55]	1634	0.703
	[0.65,0.75]	722	0.721
M4	[0.25,0.35]	564	0.725
	[0.45,0.55]	341	0.742
	[0.65,0.75]	138	0.764

Table 5.3: Correlation coefficient between the halo orientation and the recovered mass. At a given redshift, the more massive halos tend to be more ellipsoidal, and therefore we find a greater correlation. For a given mass sample, halos at higher redshift are more ellipsoidal, thus showing a similar trend.

true mass (≡virial mass). Attending to the values of the correlation coefficients we can easily conclude that, at a given redshift, the higher the mass the higher the correlation, and, for a given mass sample, the higher the redshift the higher the correlation. These trends are in agreement with the results obtained by Muñoz-Cuartas et al. [125], since they find that, at a given redshift, the most massive halos are more ellipsoidal, and, for a given mass, low redshift halos are more triaxial. Therefore, the correlation coefficients show that the ratio of the estimated mass to the true mass depends on the shape of the halo, and also that this dependence is higher when the halo population tends to be ellipsoidal (which is consistent with what one would expect). Fig. 5.19 illustrates the reason why the smaller the value of θ the greater the correlation. If the halos tend to be triaxial (all its axes are similar in length) then the orientation of the halo with respect to the LOS loses importance, and since $\left(\cos\theta_i - \overline{\cos\theta}\right)$ follows a normal distribution in each sample, the correlation gives us an idea of the average shape of the sample.

Considering this correlation coefficient we can quantify the contribution of the relative position of the halo and the LOS to the scatter in the mass calibration. We have done that by defining a new mass ratio

$$\widetilde{b}_{M_i} = b_{M_i} - r\frac{\sigma_b}{\sigma_\theta}\left(\cos\theta_i - \overline{\cos\theta}\right) \tag{5.15}$$

whose variance can be therefore estimated as

$$\sigma^2_{\widetilde{b}} = \left(1 - r^2\right)\ \sigma^2_b\ . \tag{5.16}$$

Preprints (www.preprints.org) | NOT PEER-REVIEWED | Posted: 22 March 2023 doi:10.20944/preprints202303.0387.v1

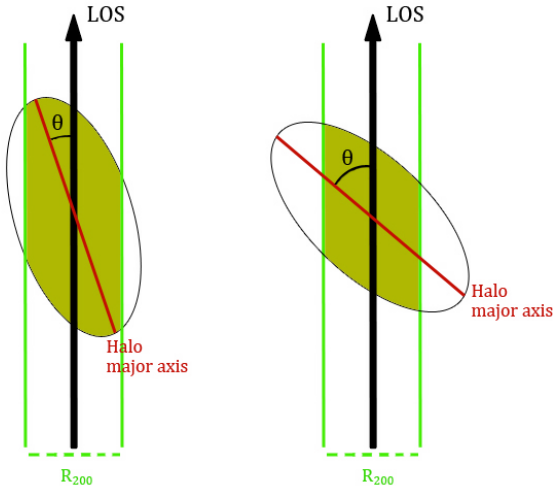

Figure 5.19: For an ellipsoidal halo, the smaller the value of the angle between LOS and its major axis, the greater is the correlation between its recovered mass and its orientation.

M_{200} (h^{-1} $M_\odot$)	Redshift	Halos	Scatter	Corrected scatter (% of the contribution)
M3	[0.25,0.35]	1846	0.141	0.103 (∼27%)
	[0.45,0.55]	1634	0.134	0.109 (∼29%)
	[0.65,0.75]	722	0.137	0.095 (∼31%)
M4	[0.25,0.35]	564	0.126	0.087 (∼31%)
	[0.45,0.55]	341	0.100	0.067 (∼33%)
	[0.65,0.75]	138	0.098	0.064 (∼35%)

Table 5.4: Upper limit of the contribution of the halo orientation to the scatter in the mass calibration. The scatter corresponds to that of the convergence maps with Nside=8192 when the weight function is applied.

In Table 5.4 we show the contribution to this scatter for the two mass samples. This contribution is around 30%, and we can interpret it as an intrinsic source of scatter that can only be corrected by means of its statistical distribution. It also seems that the contribution increases with mass and redshift, as well as the correlation coefficient in Table 5.3.

5.4 Projection effects

So far we have shown that the mass calibration is affected by an intrinsic scatter associated with the orientation of the halos, the variability of their density profiles and pixelization. We have

Preprints (www.preprints.org) | NOT PEER-REVIEWED | Posted: 22 March 2023 doi:10.20944/preprints202303.0387.v1

been able to model the effects of the latter using a weight function, and we have also quantified different contributions to the scatter.

In this section we present the scatter and bias in the mass calibration due to projection effects, i.e. that induced by all the dark matter in the LOS between the observer and the source. To measure the projection effects we use the convergence maps that include all the mass between sources and the observer, as it happens in a real observation, and compare the results with the ones in previous section where we use the convergence maps where only the particles within the halo sample under consideration where included (e.g. see Fig. 5.4). Since our sources are fixed at $z_s = 0.993$, we have divided the sky in 10 shells of width $\Delta_z = 0.1$. Table 5.5 shows the different sets of halos for each mass sample and at each redshift, although we will restrict our analysis to the two most massive samples: M3 and M4, which are the ones we studied in previous sections (e.g. Table.5.4).

		Number of halos			
	Redshift	M1	M2	M3	M4
Z1	[0.0,0.1]	996	472	200	75
Z2	[0.1,0.2]	5298	2402	929	331
Z3	[0.2,0.3]	10529	4411	1678	472
Z4	[0.3,0.4]	14533	5548	1889	551
Z5	[0.4,0.5]	15850	5909	1790	401
Z6	[0.5,0.6]	14895	5066	1445	265
Z7	[0.6,0.7]	12510	3851	987	162
Z8	[0.7,0.8]	9476	2772	568	76
Z9	[0.8,0.9]	6780	1656	305	42
Z10	[0.9,0.993]	4095	901	142	8

Table 5.5: Number of halos per mass and redshift. Mass samples are defined in Table 2.2

For the sake of comparison, we have used our weight function method on the convergence

Preprints (www.preprints.org) | NOT PEER-REVIEWED | Posted: 22 March 2023 doi:10.20944/preprints202303.0387.v1

map with Nside=8192. Table 5.6 summarizes the obtained results, showing that, as one would expect, the projection effects significantly increase the scatter and induce a bias.

		Nside=8192	
		Weighted pixels	
$\mathbf{M_{200}}$ (h^{-1} $\mathbf{M_\odot}$)	**Redshift**	$\boldsymbol{\sigma}$	μ
M3	[0.0,0.1]	0.192	1.073
	[0.1,0.2]	0.189	1.061
	[0.2,0.3]	0.187	1.110
	[0.3,0.4]	0.188	1.082
	[0.4,0.5]	0.187	1.106
	[0.5,0.6]	0.183	1.077
	[0.6,0.7]	0.186	1.095
	[0.7,0.8]	0.193	1.089
	[0.8,0.9]	0.198	1.118
	[0.9,0.993]	0.201	0.991
M4	[0.0,0.1]	0.156	1.075
	[0.1,0.2]	0.150	1.069
	[0.2,0.3]	0.147	1.041
	[0.3,0.4]	0.132	1.037
	[0.4,0.5]	0.131	1.082
	[0.5,0.6]	0.133	1.076
	[0.6,0.7]	0.129	1.093
	[0.7,0.8]	0.134	1.105
	[0.8,0.9]	0.136	0.992
	[0.9,0.993]	0.140	0.976

Table 5.6: Scatter and mean of the distributions obtained from the mass calibration of the 20 different sets of halos. The scatter increases around a 40-70% with respect to the intrinsic scatter.

 doi:10.20944/preprints202303.0387.v1

We can infer from these results that the projection effects cause a $40-70\%$ increase in the scatter of the recovered mass for both samples (with respect to their corrected intrinsic scatter), and induces a $\sim$10% bias with respect to the intrinsic bias (see Table 5.2).

5.5 Conclusions

We find that the weak lensing masses recovered through our method have an irreducible scatter of $10-14\%$, and a non-negligible bias of $\sim$1%. Possible sources of bias are the triaxiality of the halo, the substructure, and the variability of the profiles within one sample. The effects of the pixelization have been modeled in order to minimize the bias, a fact that could be masking other systematic contributions, but has allowed us to reduce the bias to a 1%, instead of the more typical values (5-10%) that can be found in the literature (see e.g. Becker & Kravtsov [16]). Those, on the other hand, are the values we obtained previous to the implementation of the weight function method (see Table 5.2).

We also find that the scatter in the recovered masses does depend on the orientation of the halo, and we estimate the contribution of this effect to the scatter to be typically of $\sim$30%.

Our analysis of the projection effects concludes that all the dark matter between observer and source introduces an additional scatter of 40-70% of the intrinsic scatter. The dominant source of scatter is the intrinsic scatter, the one due to correlated structure, and the orientation and shape of the halos, although in some cases the scatter associated with the projection effects is comparable.

The mass calibration seems to be quite sensitive to the choice of the pixels included, particularly in the case of MICE halos whose density does not drop rapidly after R_{200}.

Chapter 6

Conclusions and Future Work

"*Let chaos storm!*

Let cloud shapes swarm!

I wait for form."

Ten Mills, Robert Frost

6.1 Summary

In this thesis, we have developed a suite of analysis tools to use all-sky lightcone Nbody simulations to calibrate halo masses using weak-lensing observables.This suite of tools include the main methodology steps that go from dark-matter halo characterization, down to the intrinsic statistical bias and scatter in projected mass maps.

In particular, we studied the density profiles of MICE halos with M_{200} ranging from 4×10^{13} to 3.751×10^{14} h^{-1} $\mathbf{M}_{\odot}$ at different redshifts, and fitted them to the NFW model. To better characterize the density profiles and account for some of their inherent issues (mass resolution and softening length) we constructed twelve analytical NFW halo samples (four mass samples, each one at three different redshift bins) that would mimic those from MICE, and modeled the combined effect of the softening length and mass resolution by convoluting MICE density profiles with a Gaussian kernel. The pure NFW halo samples were simulated with four different mass

Preprints (www.preprints.org) | NOT PEER-REVIEWED | Posted: 22 March 2023 doi:10.20944/preprints202303.0387.v1

resolutions, the lowest being equal to that of MICE in order to ensure a fair comparison. Additionally, we also studied the influence of the degree of relaxedness of the halo on the concentration estimates.

We developed two new tools for the lensing analysis of all-sky simulations: shear and flexion maps. Both were constructed from the all-sky convergence maps generated by Fosalba et al. [58], and both have been validated. The former has already been used for the generation of mock galaxy catalogs. The pipelines that generate the all-sky shear and flexion maps were designed to make the most out of HEALPIX functionality and flexibility.

We analysed the morphology of MICE halos, characterizing their triaxiality at R_{200} and calculating their orientation with respect to the line-of-sight (LOS). We used the triaxility parameter defined by Franx, Illingworth & de Zeeuw [59] and, for the sake of comparison, we applied a methodology similar to that used by Allgood et al. [2] and Shaw et al.[159].

Lastly, we perform a mass calibration of halos with virial masses larger than $1.225\times\ 10^{14}$ h^{-1} $\mathbf{M}_{\odot}$, and placing the sources at a fixed redshift $z_s = 0.993$. We built two new all-sky convergence maps from two different mass cuts: M_{200}=1.225×10^{14} h^{-1} $\mathbf{M}_{\odot}$ and M_{200}=2.143×10^{14} h^{-1} $\mathbf{M}_{\odot}$. The new convergence maps were used to estimate the scatter in mass measurements due to uncorrelated structure (i.e, mass distributed along the line of sight), whereas the effect of correlated structure (i.e, environmental effects) was studied through the correlation between the orientation of the halo with respect to the LOS and the deviation of its recovered mass from the true mass, and also through the relation between halo shapes and the scatter in their recovered masses.

6.2 Halo Density Profiles

The dependence of Weak Lensing mass measurements on the assumption of a model for the density profile is, at the moment, unavoidable, thus being a matter of continuous controversy. Simulations and observational studies seek for common patterns and trends, and have already listed a variety of significant sources of error. But it is precisely the great number of problems involved in weak lensing mass estimation what makes detailed studies of density profiles derived

from cosmological simulations, making use of different approaches, indispensable in estimating the bias and scatter of the weak lensing mass measurements.

We find that MICE halos are, on average, NFW halos. They are not suitable to study substructure or the evolution of the inner slope of the density profile, but the best-fit NFW radii are in good agreement with their corresponding sample average radii, and the associated statistical errors are comparable to those found in the literature (e.g Hoekstra et al. [82]). The best-fit NFW concentrations are, on the other hand, a factor of 2 smaller than previously reported simulation fits, according to the mass-concentration relation we assume. The degree of relaxedness of the halo seems to be key when trying to recover the expected concentration (as Jeeson-Daniel et al. [94] point out), but we find that it is the combination of both mass resolution and degree of equilibrium of the halo that produces such difference in the concentration estimate. By creating a sample of pure (Monte-Carlo simulated) NFW halos with different mass resolutions we are effectively constructing a sample of halos in equilibrium, and since the samples with MICE mass resolution account for most of the variation in concentration, we find that by correcting for this bias our concentrations estimates would be within the statistical uncertainty of the fits.

Regarding the effect of the softening length, the use of a Gaussian kernel to smooth the core of the profile results in a good modeling of our projected profiles. Again the bias and scatter in concentration makes it difficult to constrain the value of the concentration, but the smoothing of an NFW density profile with the theoretical concentration and the best-fit NFW radius is the best approximation to our projected halos. MICE thus becomes a useful tool for Weak lensing analysis, and the results from any other research assuming the NFW profile as the correct mass model can be straightforwardly compared to our results.

6.3 Morphology of Halos

The statistical analysis of the shapes of MICE halos is in good agreement with the related literature, all that taking into account that the mass resolution of the simulation is far from the optimal one. Schneider et al. [153] show that a limited resolution can vary the shape of a halo, and that the error in the shape determinations is potentially degenerate with the misalignment

of halo inner and outer shapes used to constrain Brightest Cluster Galaxy alignments in some works.

That is the reason why we determine the shapes of the halos at R_{200}, so we can include as much particles as possible in the analysis. The results might therefore be understood as a statistical trend that positions MICE among other ΛCDM simulations that show a tendency to prolateness, and also as a first-order characterization of the shape of individual halos that helped us to estimate the effect of correlated structure in the weak lensing mass measurements.

6.4 All-Sky shear and flexion maps

One of the current limitations of the lensing analyses of simulations is that they are usually done on a small patch of the sky, thus loosing part of the shear information from adjacent structures. It is therefore of the essence, in order to get rid of this systematic, to make use of all-sky shear (or any other lensing observable) maps. The all sky shear and flexion maps have been constructed from the all-sky convergence maps, and allow for the combined visualization of convergence and shear/flexion. MICE mass resolution allows for the construction of all-sky shear maps useful to study the weak lensing regime. As for flexion, MICE mass resolution is not good enough to allow for the study of the regime where flexion becomes significant, since it is a gravitational lensing effect that goes with the third-order derivative of the deflection potential; a weak effect that arises when shear and convergence vary significantly over the scale of the observed image. That is the reason why we constructed the flexion maps from the Grand Challenge simulation, whose mass resolution is almost an order of magnitude higher than that of MICE.

The applications of these maps are extensive in studying different lensing regimes and purge some of the systematics associated with them. Mock galaxy catalogs have already been built based on these maps. Moreover, the combination of shear and flexion measurements stands out as a new procedure with many potential applications to cosmology, such as primordial non-Gaussianities (e.g. Fedeli et al. [56]), mass reconstruction (e.g. Pires et al. [140], Er et al. [51]), our shear-flexion coupling effects (e.g. Viola et al.[180]).

 doi:10.20944/preprints202303.0387.v1

6.5 Mass calibration

We find that a simulation with a mass resolution and a softening length like those of MICE, if accompanied by a thorough characterization of the associated problems, is valid for the study of the scatter of the weak lensing mass measurements. For example, the Large-aperture Synoptic Survey Telescope (LSST) will find of the order of 100,000 shear-selected clusters (Tyson et al. [176]), whereas the Dark Energy Survey (DES collaboration [172]) expects to build a catalog of 300 million galaxies. With such massive surveys systematics are becoming important, and the study of large data sets like the one this thesis presents are key in characterizing these and other effects. We have been able to study the scatter in mass measurements due to uncorrelated and correlated structure, as well as the scatter from due to projection effects. We find an irreducible scatter (intrinsic) of $10 - 14\%$, with a contribution of correlated structure around 30% of the intrinsic scatter, and also a scatter due to projection effects around 40-70% of the intrinsic scatter. Hence, the dominant source of scatter is the intrinsic scatter, although in some cases is comparable to that associated with the projection effects.

One would expect that as sample sizes increase, the accuracy of the lensing mass estimates improves accordingly, and our results confirm that the great number of halos used in the mass calibration has led to improved and solid statistics, as it can be seen when we compared them to those from works with similar methodologies (e.g. Becker & Kravtsov [16], de Putter & White [40]). The size of our halo sample, and the fact that we are using an all-sky simulation that includes halos with masses down to $4.68{\times}10^{13}$ h^{-1} $\mathbf{M}_{\odot}$ allows us to better estimate and reduce the effects of cosmic noise (noise introduced by the uncorrelated structure). Hoekstra et al.[81] point out that taking into account the cosmic noise is particularly important for studies that aim to constrain the density profile or estimate masses through weak lensing measurements, as it significantly contributes to the uncertainties. In this sense, our estimation of the cosmic noise contribution to scatter in mass measurements might be very useful in observational studies.

6.6 Future Work

Below I list possible developments that would benefit or extend the analyses presented in this Thesis.

6.6.1 MICE Grand Challenge Data Release

Now that all the needed data from the MICE Grand Challenge simulation is available, and the methodology developed throughout this Thesis has been tested and shows significant improvements in the determination of the cosmic noise, the most obvious future project is to repeat the analysis in §5 with this high-resolution Nbody simulation. As of the scatter due to uncorrelated structure, MICE Grand Challenge mass resolution (eight times the MICE mass resolution) should be able to provide a slightly better characterization, but the most significant improvement would be a better estimation of the scatter induced by the correlated structure, as halos of a given mass will be much better sampled. A direct comparison of the results from previous MICE and MICE Grand Challenge simulations[1] would be of great importance to understand the effects of mass resolution through all the process and other systematics, since they both model the same ΛCDM cosmology.

6.6.2 Shear-selection

In order to take full advantage of the all-sky shear maps, another interesting direction would be the creation of shear-selected halo samples and try to recover the density profiles and the masses. Combining the halo samples and the associated mock galaxy catalog with shear information, some of the systematics found in present observational studies could be reproduced.

6.6.3 Recover the Cosmology

A straightforward extension of this Thesis, which have not been done due to lack of time, is to use the calibrated weak-lensing masses to constrain cosmological parameters. Another way to recover cosmological parameters is the so-called "peak function", in analogy to the cluster mass

[1] www.ice.cat/mice

 doi:10.20944/preprints202303.0387.v1

function. This peak function measures the abundance of peaks as a function of convergence and redshift. Dietrich & Hartlap [43] found that the peak statistics gives constraints on Ω_m and σ_8 that are competitive with those expected from a cosmic-shear study, or even better. We plan to explore this cosmological application in future work.

Bibliography

[1] Abate, A., Wittman, D., Margoniner, V. E., Bridle, S. L., Gee, P., Tyson, J. A., and Dell'Antonio, I. P. Shear-selected Clusters from the Deep Lens Survey. III. Masses from Weak Lensing. *ApJ 702* (Sept. 2009), 603–613.

[2] Allgood, B., Flores, R. A., Primack, J. R., Kravtsov, A. V., Wechsler, R. H., Faltenbacher, A., and Bullock, J. S. The shape of dark matter haloes: dependence on mass, redshift, radius and formation. *MNRAS 367* (Apr. 2006), 1781–1796.

[3] Altay, G., Colberg, J. M., and Croft, R. A. C. The influence of large-scale structures on halo shapes and alignments. *MNRAS 370* (Aug. 2006), 1422–1428.

[4] Amara, A., and Réfrégier, A. Systematic bias in cosmic shear: extending the Fisher matrix. *MNRAS 391* (Nov. 2008), 228–236.

[5] Aragón-Calvo, M. A., van de Weygaert, R., Jones, B. J. T., and van der Hulst, J. M. Spin Alignment of Dark Matter Halos in Filaments and Walls. *ApJL 655* (Jan. 2007), L5–L8.

[6] Astier, P., and Pain, R. Observational Evidence of the Accelerated Expansion of the Universe. *ArXiv e-prints. astro-ph.CO/1204.5493* (Apr. 2012).

[7] Avila-Reese, V., Colín, P., Gottlöber, S., Firmani, C., and Maulbetsch, C. The Dependence on Environment of Cold Dark Matter Halo Properties. *ApJ 634* (Nov. 2005), 51–69.

[8] Avila-Reese, V., Colín, P., Valenzuela, O., D'Onghia, E., and Firmani, C. Formation and Structure of Halos in a Warm Dark Matter Cosmology. *ApJ 559* (Oct. 2001), 516–530.

[9] Bacon, D. J., Goldberg, D. M., Rowe, B. T. P., and Taylor, A. N. Weak gravitational flexion. *MNRAS 365* (Jan. 2006), 414–428.

[10] Bacon, D. J., Refregier, A. R., and Ellis, R. S. Detection of weak gravitational lensing by large-scale structure. *MNRAS 318* (Oct. 2000), 625–640.

[11] Bagla, J. S. TreePM: A Code for Cosmological N-Body Simulations. *Journal of Astrophysics and Astronomy 23* (Dec. 2002), 185–196.

[12] Bailin, J., and Steinmetz, M. Internal and External Alignment of the Shapes and Angular Momenta of ΛCDM Halos. *ApJ 627* (July 2005), 647–665.

[13] Bartelmann, M., and Schneider, P. Weak gravitational lensing. *PhR 340* (Jan. 2001), 291–472.

[14] Basilakos, S., Plionis, M., Yepes, G., Gottlöber, S., and Turchaninov, V. The shape-alignment relation in Λ cold dark matter cosmic structures. *MNRAS 365* (Jan. 2006), 539–547.

[15] Baushev, A. N. The universal density profile of the central region of dark matter haloes. *ArXiv e-prints 1205.4302* (May 2012).

[16] Becker, M. R., and Kravtsov, A. V. On the Accuracy of Weak-lensing Cluster Mass Reconstructions. *ApJ 740* (Oct. 2011), 25.

[17] Becquaert, J.-F., and Combes, F. The 3D geometry of Dark Matter Halos. *AA 325* (Sept. 1997), 41–56.

[18] Benjamin, J., Heymans, C., Semboloni, E., van Waerbeke, L., Hoekstra, H., Erben, T., Gladders, M. D., Hetterscheidt, M., Mellier, Y., and Yee, H. K. C. Cosmological constraints from the 100-deg^2 weak-lensing survey. *MNRAS 381* (Oct. 2007), 702–712.

[19] Bennett, C. L., Halpern, M., Hinshaw, G., Jarosik, N., Kogut, A., Limon, M., Meyer, S. S., Page, L., Spergel, D. N., Tucker, G. S., Wollack, E., Wright, E. L., Barnes, C., Greason, M. R., Hill, R. S., Komatsu, E., Nolta, M. R., Odegard, N., Peiris, H. V., Verde, L., and

Weiland, J. L. First-Year Wilkinson Microwave Anisotropy Probe (WMAP) Observations: Preliminary Maps and Basic Results. *ApJS 148* (Sept. 2003), 1–27.

[20] Bernardeau, F., Colombi, S., Gaztañaga, E., and Scoccimarro, R. Large-scale structure of the Universe and cosmological perturbation theory. *PhR 367* (Sept. 2002), 1–248.

[21] Betancort-Rijo, J. E., and Trujillo, I. An analytical framework to describe the orientation of dark matter halos and galaxies within the large-scale structure. *ArXiv e-prints. astro-ph.CO/0912.1051* (Dec. 2009).

[22] Bett, P., Eke, V., Frenk, C. S., Jenkins, A., Helly, J., and Navarro, J. The spin and shape of dark matter haloes in the Millennium simulation of a Λ cold dark matter universe. *MNRAS 376* (Mar. 2007), 215–232.

[23] Bonnet, H., Mellier, Y., and Fort, B. First detection of a gravitational weak shear at the periphery of CL 0024+1654. *ApJ Letters 427* (June 1994), L83–L86.

[24] Broadhurst, T., Takada, M., Umetsu, K., Kong, X., Arimoto, N., Chiba, M., and Futamase, T. The Surprisingly Steep Mass Profile of A1689, from a Lensing Analysis of Subaru Images. *ApJL 619* (Feb. 2005), L143–L146.

[25] Broadhurst, T., Umetsu, K., Medezinski, E., Oguri, M., and Rephaeli, Y. Comparison of Cluster Lensing Profiles with ΛCDM Predictions. *ApJL 685* (Sept. 2008), L9–L12.

[26] Brown, M. L., Taylor, A. N., Bacon, D. J., Gray, M. E., Dye, S., Meisenheimer, K., and Wolf, C. The shear power spectrum from the COMBO-17 survey. *MNRAS 341* (May 2003), 100–118.

[27] Bullock, J. S. Shapes of Dark Matter Halos. In *The Shapes of Galaxies and their Dark Halos* (Mar. 2002), P. Natarajan, Ed., pp. 109–113.

[28] Bullock, J. S., Kolatt, T. S., Sigad, Y., Somerville, R. S., Kravtsov, A. V., Klypin, A. A., Primack, J. R., and Dekel, A. Profiles of dark haloes: evolution, scatter and environment. *MNRAS 321* (Mar. 2001), 559–575.

[29] Buote, D. A., and Canizares, C. R. X-ray isophote shapes and the mass of NGC 3923. *MNRAS 298* (Aug. 1998), 811–823.

[30] Buote, D. A., Jeltema, T. E., Canizares, C. R., and Garmire, G. P. Chandra Evidence of a Flattened, Triaxial Dark Matter Halo in the Elliptical Galaxy NGC 720. *ApJ 577* (Sept. 2002), 183–196.

[31] Castro, P. G., Heavens, A. F., and Kitching, T. D. Weak lensing analysis in three dimensions. *PhRvD 72*, 2 (July 2005), 023516.

[32] Colberg, J. M., White, S. D. M., Jenkins, A., and Pearce, F. R. Linking cluster formation to large-scale structure. *MNRAS 308* (Sept. 1999), 593–598.

[33] Cole, S., and Lacey, C. The structure of dark matter haloes in hierarchical clustering models. *MNRAS 281* (July 1996), 716.

[34] Cole, S., Percival, W. J., Peacock, J. A., Norberg, P., Baugh, C. M., Frenk, C. S., Baldry, I., Bland-Hawthorn, J., Bridges, T., Cannon, R., Colless, M., Collins, C., Couch, W., Cross, N. J. G., Dalton, G., Eke, V. R., De Propris, R., Driver, S. P., Efstathiou, G., Ellis, R. S., Glazebrook, K., Jackson, C., Jenkins, A., Lahav, O., Lewis, I., Lumsden, S., Maddox, S., Madgwick, D., Peterson, B. A., Sutherland, W., and Taylor, K. The 2dF Galaxy Redshift Survey: power-spectrum analysis of the final data set and cosmological implications. *MNRAS 362* (Sept. 2005), 505–534.

[35] Consortium, V., :, Thomas, P. A., Colberg, J. M., Couchman, H. M. P., Efstathiou, G. P., Frenk, C. S., Jenkins, A. R., Nelson, A. H., Hutchings, R. M., Peacock, J. A., Pearce, F. R., and White, S. D. M. The structure of galaxy clusters in different cosmologies. *MNRAS 296* (Jan. 1998), 1061–1071.

[36] Cooray, A., and Sheth, R. Halo models of large scale structure. *PhysRep 372* (Dec. 2002), 1–129.

[37] Crocce, M., Fosalba, P., Castander, F. J., and Gaztañaga, E. Simulating the Universe with MICE: the abundance of massive clusters. *MNRAS 403* (Apr. 2010), 1353–1367.

 doi:10.20944/preprints202303.0387.v1

[38] Das, S., and Bode, P. A Large Sky Simulation of the Gravitational Lensing of the Cosmic Microwave Background. *ApJ 682* (July 2008), 1–13.

[39] Davis, M., Efstathiou, G., Frenk, C. S., and White, S. D. M. The evolution of large-scale structure in a universe dominated by cold dark matter. *ApJ 292* (May 1985), 371–394.

[40] de Putter, R., and White, M. Using weak lensing to find halo masses. *NewA 10* (Aug. 2005), 676–687.

[41] Diemand, J., Kuhlen, M., Madau, P., Zemp, M., Moore, B., Potter, D., and Stadel, J. Clumps and streams in the local dark matter distribution. *Nature 454* (Aug. 2008), 735–738.

[42] Diemand, J., and Moore, B. The Structure and Evolution of Cold Dark Matter Halos. *Advanced Science Letters 4* (Feb. 2011), 297–310.

[43] Dietrich, J. P., and Hartlap, J. Cosmology with the shear-peak statistics. *MNRAS 402* (Feb. 2010), 1049–1058.

[44] Dodelson, S. Cluster masses: Accounting for structure along the line of sight. *PhRvD 70*, 2 (July 2004), 023008.

[45] Dodelson, S., Kolb, E. W., Matarrese, S., Riotto, A., and Zhang, P. Second order geodesic corrections to cosmic shear. *PhRvD 72*, 10 (Nov. 2005), 103004.

[46] Dubinski, J., and Carlberg, R. G. The structure of cold dark matter halos. *ApJ 378* (Sept. 1991), 496–503.

[47] Duffy, A. R., Schaye, J., Kay, S. T., and Dalla Vecchia, C. Dark matter halo concentrations in the Wilkinson Microwave Anisotropy Probe year 5 cosmology. *MNRAS 390* (Oct. 2008), L64–L68.

[48] Dunkley, J., Komatsu, E., Nolta, M. R., Spergel, D. N., Larson, D., Hinshaw, G., Page, L., Bennett, C. L., Gold, B., Jarosik, N., Weiland, J. L., Halpern, M., Hill, R. S., Kogut, A., Limon, M., Meyer, S. S., Tucker, G. S., Wollack, E., and Wright, E. L. Five-Year

Wilkinson Microwave Anisotropy Probe Observations: Likelihoods and Parameters from the WMAP Data. *ApJS 180* (Feb. 2009), 306–329.

[49] Einasto, J. On the Construction of a Composite Model for the Galaxy and on the Determination of the System of Galactic Parameters. *Trudy Astrofizicheskogo Instituta Alma-Ata 5* (1965), 87–100.

[50] Eisenstein, D. J., Zehavi, I., Hogg, D. W., Scoccimarro, R., Blanton, M. R., Nichol, R. C., Scranton, R., Seo, H.-J., Tegmark, M., Zheng, Z., Anderson, S. F., Annis, J., Bahcall, N., Brinkmann, J., Burles, S., Castander, F. J., Connolly, A., Csabai, I., Doi, M., Fukugita, M., Frieman, J. A., Glazebrook, K., Gunn, J. E., Hendry, J. S., Hennessy, G., Ivezić, Z., Kent, S., Knapp, G. R., Lin, H., Loh, Y.-S., Lupton, R. H., Margon, B., McKay, T. A., Meiksin, A., Munn, J. A., Pope, A., Richmond, M. W., Schlegel, D., Schneider, D. P., Shimasaku, K., Stoughton, C., Strauss, M. A., SubbaRao, M., Szalay, A. S., Szapudi, I., Tucker, D. L., Yanny, B., and York, D. G. Detection of the Baryon Acoustic Peak in the Large-Scale Correlation Function of SDSS Luminous Red Galaxies. *ApJ 633* (Nov. 2005), 560–574.

[51] Er, X., Li, G., and Schneider, P. Mass reconstruction by gravitational shear and flexion. *ArXiv e-prints. astro-ph.CO/1008.3088* (Aug. 2010).

[52] Fahlman, G., Kaiser, N., Squires, G., and Woods, D. Dark matter in MS 1224 from distortion of background galaxies. *ApJ 437* (Dec. 1994), 56–62.

[53] Faltenbacher, A., Allgood, B., Gottlöber, S., Yepes, G., and Hoffman, Y. Imprints of mass accretion on properties of galaxy clusters. *MNRAS 362* (Sept. 2005), 1099–1108.

[54] Faltenbacher, A., Gottlöber, S., Kerscher, M., and Müller, V. Correlations in the orientations of galaxy clusters. *AA 395* (Nov. 2002), 1–9.

[55] Fasano, G., Amico, P., Bertola, F., Vio, R., and Zeilinger, W. W. The intrinsic shapes of galactic discs. *MNRAS 262* (May 1993), 109–118.

[56] Fedeli, C., Bartelmann, M., and Moscardini, L. Constraining primordial non-Gaussianity with cosmological weak lensing: shear and flexion. *JCAP 10* (Oct. 2012), 18.

[57] Fillmore, J. A., and Goldreich, P. Self-similar gravitational collapse in an expanding universe. *ApJ 281* (June 1984), 1–8.

[58] Fosalba, P., Gaztañaga, E., Castander, F. J., and Manera, M. The onion universe: all sky lightcone simulations in spherical shells. *MNRAS 391* (Nov. 2008), 435–446.

[59] Franx, M., Illingworth, G., and de Zeeuw, T. The ordered nature of elliptical galaxies - Implications for their intrinsic angular momenta and shapes. *ApJ 383* (Dec. 1991), 112–134.

[60] Frenk, C. S., White, S. D. M., Bode, P., Bond, J. R., Bryan, G. L., Cen, R., Couchman, H. M. P., Evrard, A. E., Gnedin, N., Jenkins, A., Khokhlov, A. M., Klypin, A., Navarro, J. F., Norman, M. L., Ostriker, J. P., Owen, J. M., Pearce, F. R., Pen, U.-L., Steinmetz, M., Thomas, P. A., Villumsen, J. V., Wadsley, J. W., Warren, M. S., Xu, G., and Yepes, G. The Santa Barbara Cluster Comparison Project: A Comparison of Cosmological Hydrodynamics Solutions. *ApJ 525* (Nov. 1999), 554–582.

[61] Frenk, C. S., White, S. D. M., Davis, M., and Efstathiou, G. The formation of dark halos in a universe dominated by cold dark matter. *ApJ 327* (Apr. 1988), 507–525.

[62] Fu, L., Semboloni, E., Hoekstra, H., Kilbinger, M., van Waerbeke, L., Tereno, I., Mellier, Y., Heymans, C., Coupon, J., Benabed, K., Benjamin, J., Bertin, E., Doré, O., Hudson, M. J., Ilbert, O., Maoli, R., Marmo, C., McCracken, H. J., and Ménard, B. Very weak lensing in the CFHTLS wide: cosmology from cosmic shear in the linear regime. *AA 479* (Feb. 2008), 9–25.

[63] Fukushige, T., and Makino, J. On the Origin of Cusps in Dark Matter Halos. *ApJL 477* (Mar. 1997), L9.

[64] Fukushige, T., and Makino, J. Structure of Dark Matter Halos from Hierarchical Clustering. *ApJ 557* (Aug. 2001), 533–545.

[65] Gao, L., Navarro, J. F., Cole, S., Frenk, C. S., White, S. D. M., Springel, V., Jenkins, A., and Neto, A. F. The redshift dependence of the structure of massive Λ cold dark matter haloes. *MNRAS 387* (June 2008), 536–544.

[66] Ghigna, S., Moore, B., Governato, F., Lake, G., Quinn, T., and Stadel, J. Density Profiles and Substructure of Dark Matter Halos: Converging Results at Ultra-High Numerical Resolution. *ApJ 544* (Dec. 2000), 616–628.

[67] Górski, K. M., Hivon, E., Banday, A. J., Wandelt, B. D., Hansen, F. K., Reinecke, M., and Bartelmann, M. HEALPix: A Framework for High-Resolution Discretization and Fast Analysis of Data Distributed on the Sphere. *ApJ 622* (Apr. 2005), 759–771.

[68] Gottlöber, S., and Turchaninov, V. Halo Shape and its Relation to Environment. In *EAS Publications Series* (2006), G. A. Mamon, F. Combes, C. Deffayet, and B. Fort, Eds., vol. 20 of *EAS Publications Series*, pp. 25–28.

[69] Gruen, D., Bernstein, G. M., Lam, T. Y., and Seitz, S. Optimizing weak lensing mass estimates for cluster profile uncertainty. *MNRAS 416* (Sept. 2011), 1392–1400.

[70] Gulkis, S., Lubin, P. M., Meyer, S. S., and Silverberg, R. F. The Cosmic Background Explorer. *SciAm 262* (Jan. 1990), 132–139.

[71] Gunn, J. E., and Gott, III, J. R. On the Infall of Matter Into Clusters of Galaxies and Some Effects on Their Evolution. *ApJ 176* (Aug. 1972), 1.

[72] Hahn, O., Carollo, C. M., Porciani, C., and Dekel, A. The evolution of dark matter halo properties in clusters, filaments, sheets and voids. *MNRAS 381* (Oct. 2007), 41–51.

[73] Hahn, O., Porciani, C., Carollo, C. M., and Dekel, A. Properties of dark matter haloes in clusters, filaments, sheets and voids. *MNRAS 375* (Feb. 2007), 489–499.

[74] Hayashi, E., Navarro, J. F., and Springel, V. The shape of the gravitational potential in cold dark matter haloes. *MNRAS 377* (May 2007), 50–62.

[75] Heitmann, K., Lukić, Z., Habib, S., and Ricker, P. M. Capturing Halos at High Redshifts. *ApJL 642* (May 2006), L85–L88.

[76] Hernquist, L., and Katz, N. TREESPH - A unification of SPH with the hierarchical tree method. *ApJS 70* (June 1989), 419–446.

[77] Heymans, C., White, M., Heavens, A., Vale, C., and van Waerbeke, L. Potential sources of contamination to weak lensing measurements: constraints from N-body simulations. *MNRAS 371* (Sept. 2006), 750–760.

[78] Hilbert, S., Hartlap, J., White, S. D. M., and Schneider, P. Ray-tracing through the Millennium Simulation: Born corrections and lens-lens coupling in cosmic shear and galaxy-galaxy lensing. *AAP 499* (May 2009), 31–43.

[79] Hirata, C. M., and Seljak, U. Intrinsic alignment-lensing interference as a contaminant of cosmic shear. *PhRvD 70*, 6 (Sept. 2004), 063526.

[80] Hoekstra, H. A comparison of weak-lensing masses and X-ray properties of galaxy clusters. *MNRAS 379* (July 2007), 317–330.

[81] Hoekstra, H., Bartelmann, M., Dahle, H., Israel, H., Limousin, M., and Meneghetti, M. Masses of Galaxy Clusters from Gravitational Lensing. *SSR 177* (Aug. 2013), 75–118.

[82] Hoekstra, H., Hartlap, J., Hilbert, S., and van Uitert, E. Effects of distant large-scale structure on the precision of weak lensing mass measurements. *MNRAS 412* (Apr. 2011), 2095–2103.

[83] Hoekstra, H., and Jain, B. Weak Gravitational Lensing and Its Cosmological Applications. *Annual Review of Nuclear and Particle Science 58* (Nov. 2008), 99–123.

[84] Hoekstra, H., Mellier, Y., van Waerbeke, L., Semboloni, E., Fu, L., Hudson, M. J., Parker, L. C., Tereno, I., and Benabed, K. First Cosmic Shear Results from the Canada-France-Hawaii Telescope Wide Synoptic Legacy Survey. *ApJ 647* (Aug. 2006), 116–127.

[85] Hoekstra, H., Yee, H. K. C., and Gladders, M. D. Constraints on Ω_m and σ_8 from Weak Lensing in Red-Sequence Cluster Survey Fields. *ApJ 577* (Oct. 2002), 595–603.

[86] Hoekstra, H., Yee, H. K. C., and Gladders, M. D. Properties of Galaxy Dark Matter Halos from Weak Lensing. *ApJ 606* (May 2004), 67–77.

[87] Hopkins, P. F., Bahcall, N. A., and Bode, P. Cluster Alignments and Ellipticities in ΛCDM Cosmology. *ApJ 618* (Jan. 2005), 1–15.

 doi:10.20944/preprints202303.0387.v1

[88] Hu, W. Weak lensing of the CMB: A harmonic approach. *PhRvD 62*, 4 (Aug. 2000), 043007.

[89] Hu, W., and White, M. Acoustic Signatures in the Cosmic Microwave Background. *ApJ 471* (Nov. 1996), 30.

[90] Hu, W., and White, M. CMB anisotropies: Total angular momentum method. *Phys. Rev. D 56* (July 1997), 596–615.

[91] Huff, E. M., Eifler, T., Hirata, C. M., Mandelbaum, R., Schlegel, D., and Seljak, U. Seeing in the dark – II. Cosmic shear in the Sloan Digital Sky Survey. *ArXiv e-prints. astro-ph.CO/1112.3143* (Dec. 2011).

[92] Jarosik, N., Bennett, C. L., Dunkley, J., Gold, B., Greason, M. R., Halpern, M., Hill, R. S., Hinshaw, G., Kogut, A., Komatsu, E., Larson, D., Limon, M., Meyer, S. S., Nolta, M. R., Odegard, N., Page, L., Smith, K. M., Spergel, D. N., Tucker, G. S., Weiland, J. L., Wollack, E., and Wright, E. L. Seven-year Wilkinson Microwave Anisotropy Probe (WMAP) Observations: Sky Maps, Systematic Errors, and Basic Results. *ApJS 192* (Feb. 2011), 14.

[93] Jarvis, M., Bernstein, G. M., Fischer, P., Smith, D., Jain, B., Tyson, J. A., and Wittman, D. Weak-Lensing Results from the 75 Square Degree Cerro Tololo Inter-American Observatory Survey. *AJ 125* (Mar. 2003), 1014–1032.

[94] Jeeson-Daniel, A., Dalla Vecchia, C., Haas, M. R., and Schaye, J. The correlation structure of dark matter halo properties. *MNRAS 415* (July 2011), L69–L73.

[95] Jenkins, A., Frenk, C. S., White, S. D. M., Colberg, J. M., Cole, S., Evrard, A. E., Couchman, H. M. P., and Yoshida, N. The mass function of dark matter haloes. *MNRAS 321* (Feb. 2001), 372–384.

[96] Jing, Y. P., and Suto, Y. Triaxial Modeling of Halo Density Profiles with High-Resolution N-Body Simulations. *ApJ 574* (Aug. 2002), 538–553.

[97] Johnston, D. E., Sheldon, E. S., Wechsler, R. H., Rozo, E., Koester, B. P., Frieman, J. A., McKay, T. A., Evrard, A. E., Becker, M. R., and Annis, J. Cross-correlation Weak Lensing of SDSS galaxy Clusters II: Cluster Density Profiles and the Mass–Richness Relation. *ArXiv e-prints: 0709.1159* (Sept. 2007).

[98] Jones, C., and Forman, W. The structure of clusters of galaxies observed with Einstein. *ApJ 276* (Jan. 1984), 38–55.

[99] Kaiser, N. Weak gravitational lensing of distant galaxies. *ApJ 388* (Apr. 1992), 272–286.

[100] Kaiser, N., Wilson, G., and Luppino, G. A. Large-Scale Cosmic Shear Measurements. *arXiv:astro-ph/0003338* (Mar. 2000).

[101] Kasun, S. F., and Evrard, A. E. Shapes and Alignments of Galaxy Cluster Halos. *ApJ 629* (Aug. 2005), 781–790.

[102] Knebe, A., Green, A., and Binney, J. Multi-level adaptive particle mesh (MLAPM): a c code for cosmological simulations. *MNRAS 325* (Aug. 2001), 845–864.

[103] Kowalski, M., Rubin, D., Aldering, G., Agostinho, R. J., Amadon, A., Amanullah, R., Balland, C., Barbary, K., Blanc, G., Challis, P. J., Conley, A., Connolly, N. V., Covarrubias, R., Dawson, K. S., Deustua, S. E., Ellis, R., Fabbro, S., Fadeyev, V., Fan, X., Farris, B., Folatelli, G., Frye, B. L., Garavini, G., Gates, E. L., Germany, L., Goldhaber, G., Goldman, B., Goobar, A., Groom, D. E., Haissinski, J., Hardin, D., Hook, I., Kent, S., Kim, A. G., Knop, R. A., Lidman, C., Linder, E. V., Mendez, J., Meyers, J., Miller, G. J., Moniez, M., Mourão, A. M., Newberg, H., Nobili, S., Nugent, P. E., Pain, R., Perdereau, O., Perlmutter, S., Phillips, M. M., Prasad, V., Quimby, R., Regnault, N., Rich, J., Rubenstein, E. P., Ruiz-Lapuente, P., Santos, F. D., Schaefer, B. E., Schommer, R. A., Smith, R. C., Soderberg, A. M., Spadafora, A. L., Strolger, L.-G., Strovink, M., Suntzeff, N. B., Suzuki, N., Thomas, R. C., Walton, N. A., Wang, L., Wood-Vasey, W. M., Yun, J. L., and Supernova Cosmology Project. Improved Cosmological Constraints from New, Old, and Combined Supernova Data Sets. *ApJ 686* (Oct. 2008), 749–778.

[104] Kuhlen, M., Diemand, J., and Madau, P. The Shapes, Orientation, and Alignment of Galactic Dark Matter Subhalos. *ApJ 671* (Dec. 2007), 1135–1146.

[105] Kuhn, Thomas S. *The structure of scientific revolutions*. University of Chicago Press, 1996.

[106] Larson, D., Dunkley, J., Hinshaw, G., Komatsu, E., Nolta, M. R., Bennett, C. L., Gold, B., Halpern, M., Hill, R. S., Jarosik, N., Kogut, A., Limon, M., Meyer, S. S., Odegard, N., Page, L., Smith, K. M., Spergel, D. N., Tucker, G. S., Weiland, J. L., Wollack, E., and Wright, E. L. Seven-year Wilkinson Microwave Anisotropy Probe (WMAP) Observations: Power Spectra and WMAP-derived Parameters. *ApJS 192* (Feb. 2011), 16.

[107] Lasky, P. D., and Fluke, C. J. Shape, shear and flexion: an analytic flexion formalism for realistic mass profiles. *MNRAS 396* (July 2009), 2257–2268.

[108] Lee, J., Jing, Y. P., and Suto, Y. An Analytic Model for the Axis Ratio Distribution of Dark Matter Halos from the Primordial Gaussian Density Field. *ApJ 632* (Oct. 2005), 706–712.

[109] Lee, J., and Pen, U.-L. The Nonlinear Evolution of Galaxy Intrinsic Alignments. *ApJ 681* (July 2008), 798–805.

[110] Lemson, G., and Kauffmann, G. Environmental influences on dark matter haloes and consequences for the galaxies within them. *MNRAS 302* (Jan. 1999), 111–117.

[111] Leonard, A., Goldberg, D. M., Haaga, J. L., and Massey, R. Gravitational Shear, Flexion, and Strong Lensing in Abell 1689. *ApJ 666* (Sept. 2007), 51–63.

[112] Leonard, A., King, L. J., and Wilkins, S. M. Detecting mass substructure in galaxy clusters: an aperture mass statistic for gravitational flexion. *MNRAS 395* (May 2009), 1438–1448.

[113] Li, B., Zhao, G.-B., Teyssier, R., and Koyama, K. ECOSMOG: an Efficient COde for Simulating MOdified Gravity. *JCAP 1* (Jan. 2012), 51.

[114] Lima, M., Jain, B., and Devlin, M. Lensing magnification: implications for counts of submillimetre galaxies and SZ clusters. *MNRAS 406* (Aug. 2010), 2352–2372.

[115] Lukić, Z., Heitmann, K., Habib, S., Bashinsky, S., and Ricker, P. M. The Halo Mass Function: High-Redshift Evolution and Universality. *ApJ 671* (Dec. 2007), 1160–1181.

[116] Macciò, A. V., Dutton, A. A., and van den Bosch, F. C. Concentration, spin and shape of dark matter haloes as a function of the cosmological model: WMAP1, WMAP3 and WMAP5 results. *MNRAS 391* (Dec. 2008), 1940–1954.

[117] Macciò, A. V., Dutton, A. A., van den Bosch, F. C., Moore, B., Potter, D., and Stadel, J. Concentration, spin and shape of dark matter haloes: scatter and the dependence on mass and environment. *MNRAS 378* (June 2007), 55–71.

[118] Mandelbaum, R., Hirata, C. M., Ishak, M., Seljak, U., and Brinkmann, J. Detection of large-scale intrinsic ellipticity-density correlation from the Sloan Digital Sky Survey and implications for weak lensing surveys. *MNRAS 367* (Apr. 2006), 611–626.

[119] Mandelbaum, R., Tasitsiomi, A., Seljak, U., Kravtsov, A. V., and Wechsler, R. H. Galaxy-galaxy lensing: dissipationless simulations versus the halo model. *MNRAS 362* (Oct. 2005), 1451–1462.

[120] Massey, R., Refregier, A., Bacon, D. J., Ellis, R., and Brown, M. L. An enlarged cosmic shear survey with the William Herschel Telescope. *MNRAS 359* (June 2005), 1277–1286.

[121] Mather, J. C. Bolometer noise: nonequilibrium thoery. *ApOpt 21* (Mar. 1982), 1125–1129.

[122] Mather, J. C., Cheng, E. S., Eplee, Jr., R. E., Isaacman, R. B., Meyer, S. S., Shafer, R. A., Weiss, R., Wright, E. L., Bennett, C. L., Boggess, N. W., Dwek, E., Gulkis, S., Hauser, M. G., Janssen, M., Kelsall, T., Lubin, P. M., Moseley, Jr., S. H., Murdock, T. L., Silverberg, R. F., Smoot, G. F., and Wilkinson, D. T. A preliminary measurement of the cosmic microwave background spectrum by the Cosmic Background Explorer (COBE) satellite. *ApJL 354* (May 1990), L37–L40.

[123] Maturi, M., Meneghetti, M., Bartelmann, M., Dolag, K., and Moscardini, L. An optimal filter for the detection of galaxy clusters through weak lensing. *AA 442* (Nov. 2005), 851–860.

[124] Merritt, D., Graham, A. W., Moore, B., Diemand, J., and Terzić, B. Empirical Models for Dark Matter Halos. I. Nonparametric Construction of Density Profiles and Comparison with Parametric Models. *AJ 132* (Dec. 2006), 2685–2700.

[125] Muñoz-Cuartas, J. C., Macciò, A. V., Gottlöber, S., and Dutton, A. A. The redshift evolution of Λ cold dark matter halo parameters: concentration, spin and shape. *MNRAS 411* (Feb. 2011), 584–594.

[126] Munshi, D., Valageas, P., van Waerbeke, L., and Heavens, A. Cosmology with weak lensing surveys. *PhR 462* (June 2008), 67–121.

[127] Navarro, J. F., Frenk, C. S., and White, S. D. M. A Universal Density Profile from Hierarchical Clustering. *ApJ 490* (Dec. 1997), 493.

[128] Navarro, J. F., Ludlow, A., Springel, V., Wang, J., Vogelsberger, M., White, S. D. M., Jenkins, A., Frenk, C. S., and Helmi, A. The diversity and similarity of simulated cold dark matter haloes. *MNRAS 402* (Feb. 2010), 21–34.

[129] Neto, A. F., Gao, L., Bett, P., Cole, S., Navarro, J. F., Frenk, C. S., White, S. D. M., Springel, V., and Jenkins, A. The statistics of Λ CDM halo concentrations. *MNRAS 381* (Nov. 2007), 1450–1462.

[130] Oguri, M., and Hamana, T. Detailed cluster lensing profiles at large radii and the impact on cluster weak lensing studies. *MNRAS 414* (July 2011), 1851–1861.

[131] Okabe, N., Okura, Y., and Futamase, T. Weak-lensing Mass Measurements of Substructures in Coma Cluster with Subaru/Suprime-cam. *ApJ 713* (Apr. 2010), 291–303.

[132] Okura, Y., Umetsu, K., and Futamase, T. A New Measure for Weak-Lensing Flexion. *ApJ 660* (May 2007), 995–1002.

[133] Okura, Y., Umetsu, K., and Futamase, T. A Method for Weak-Lensing Flexion Analysis by the HOLICs Moment Approach. *ApJ 680* (June 2008), 1–16.

[134] Olling, R. P. The Highly Flattened Dark Matter Halo of NGC 4244. *AJ 112* (Aug. 1996), 481.

 doi:10.20944/preprints202303.0387.v1

[135] Patiri, S. G., Cuesta, A. J., Prada, F., Betancort-Rijo, J., and Klypin, A. The Alignment of Dark Matter Halos with the Cosmic Web. *ApJL 652* (Dec. 2006), L75–L78.

[136] Peacock, J. A. *Cosmological Physics*. Cambridge University Press, January 1999.

[137] Pedersen, K., and Dahle, H. Calibration of the Mass-Temperature Relation for Clusters of Galaxies Using Weak Gravitational Lensing. *ApJ 667* (Sept. 2007), 26–34.

[138] Peebles, P. J. E. *The large-scale structure of the universe*. 1980.

[139] Perlmutter, S., Aldering, G., Goldhaber, G., Knop, R. A., Nugent, P., Castro, P. G., Deustua, S., Fabbro, S., Goobar, A., Groom, D. E., Hook, I. M., Kim, A. G., Kim, M. Y., Lee, J. C., Nunes, N. J., Pain, R., Pennypacker, C. R., Quimby, R., Lidman, C., Ellis, R. S., Irwin, M., McMahon, R. G., Ruiz-Lapuente, P., Walton, N., Schaefer, B., Boyle, B. J., Filippenko, A. V., Matheson, T., Fruchter, A. S., Panagia, N., Newberg, H. J. M., Couch, W. J., and Supernova Cosmology Project. Measurements of Omega and Lambda from 42 High-Redshift Supernovae. *ApJ 517* (June 1999), 565–586.

[140] Pires, S., and Amara, A. Weak Lensing Mass Reconstruction: Flexion Versus Shear. *ApJ 723* (Nov. 2010), 1507–1511.

[141] Primack, J. R., Seckel, D., and Sadoulet, B. Detection of cosmic dark matter. *Annual Review of Nuclear and Particle Science 38* (1988), 751–807.

[142] Ragone-Figueroa, C., Plionis, M., Merchán, M., Gottlöber, S., and Yepes, G. The relation between halo shape, velocity dispersion and formation time. *MNRAS 407* (Sept. 2010), 581–589.

[143] Reed, D., Gardner, J., Quinn, T., Stadel, J., Fardal, M., Lake, G., and Governato, F. Evolution of the mass function of dark matter haloes. *MNRAS 346* (Dec. 2003), 565–572.

[144] Reed, D., Governato, F., Verde, L., Gardner, J., Quinn, T., Stadel, J., Merritt, D., and Lake, G. Evolution of the density profiles of dark matter haloes. *MNRAS 357* (Feb. 2005), 82–96.

 doi:10.20944/preprints202303.0387.v1

[145] Reed, D. S., Bower, R., Frenk, C. S., Jenkins, A., and Theuns, T. The halo mass function from the dark ages through the present day. *MNRAS 374* (Jan. 2007), 2–15.

[146] Refregier, A. Weak Gravitational Lensing by Large-Scale Structure. *ARAA 41* (2003), 645–668.

[147] Riess, A. G., Filippenko, A. V., Challis, P., Clocchiatti, A., Diercks, A., Garnavich, P. M., Gilliland, R. L., Hogan, C. J., Jha, S., Kirshner, R. P., Leibundgut, B., Phillips, M. M., Reiss, D., Schmidt, B. P., Schommer, R. A., Smith, R. C., Spyromilio, J., Stubbs, C., Suntzeff, N. B., and Tonry, J. Observational Evidence from Supernovae for an Accelerating Universe and a Cosmological Constant. *AJ 116* (Sept. 1998), 1009–1038.

[148] Robotham, A., Phillipps, S., and De Propris, R. The Shapes of Galaxy Groups: Footballs or Frisbees? *ApJ 672* (Jan. 2008), 834–848.

[149] Rossi, G., Sheth, R. K., and Tormen, G. Modelling the shapes of the largest gravitationally bound objects. *MNRAS 416* (Sept. 2011), 248–261.

[150] Rozo, E., and Schmidt, F. Weak Lensing Mass Calibration with Shear and Magnification. *astro-ph.CO/1009.5735* (Sept. 2010).

[151] Salvador-Solé, E., Serra, S., Manrique, A., and González-Casado, G. Theoretical dark matter halo kinematics and triaxial shape. *MNRAS 424* (Aug. 2012), 3129–3144.

[152] Schäfer, B. M., Heisenberg, L., Kalovidouris, A. F., and Bacon, D. J. On the validity of the Born approximation for weak cosmic flexions. *MNRAS 420* (Feb. 2012), 455–467.

[153] Schneider, M. D., Frenk, C. S., and Cole, S. The shapes and alignments of dark matter halos. *JCAP 5* (May 2012), 30.

[154] Schneider, P. Weak Gravitational Lensing. *ArXiv Astrophysics e-prints. astro-ph/0509252* (Sept. 2005).

[155] Schrabback, T., Erben, T., Simon, P., Miralles, J.-M., Schneider, P., Heymans, C., Eifler, T., Fosbury, R. A. E., Freudling, W., Hetterscheidt, M., Hildebrandt, H., and Pirzkal, N.

 doi:10.20944/preprints202303.0387.v1

Cosmic shear analysis of archival HST/ACS data. I. Comparison of early ACS pure parallel data to the HST/GEMS survey. *AA 468* (June 2007), 823–847.

[156] Schrabback, T., Hartlap, J., Joachimi, B., Kilbinger, M., Simon, P., Benabed, K., Bradač, M., Eifler, T., Erben, T., Fassnacht, C. D., High, F. W., Hilbert, S., Hildebrandt, H., Hoekstra, H., Kuijken, K., Marshall, P. J., Mellier, Y., Morganson, E., Schneider, P., Semboloni, E., van Waerbeke, L., and Velander, M. Evidence of the accelerated expansion of the Universe from weak lensing tomography with COSMOS. *AA 516* (June 2010), A63.

[157] Semboloni, E., Mellier, Y., van Waerbeke, L., Hoekstra, H., Tereno, I., Benabed, K., Gwyn, S. D. J., Fu, L., Hudson, M. J., Maoli, R., and Parker, L. C. Cosmic shear analysis with CFHTLS deep data. *AA 452* (June 2006), 51–61.

[158] Shapiro, C., and Cooray, A. The Born and lens lens corrections to weak gravitational lensing angular power spectra. *JCAP 3* (Mar. 2006), 7.

[159] Shaw, L. D., Weller, J., Ostriker, J. P., and Bode, P. Statistics of Physical Properties of Dark Matter Clusters. *ApJ 646* (Aug. 2006), 815–833.

[160] Smith, R. E., Desjacques, V., and Marian, L. Nonlinear clustering in models with primordial non-Gaussianity: The halo model approach. *PhRvD 83*, 4 (Feb. 2011), 043526.

[161] Spergel, D. N., and Steinhardt, P. J. Observational Evidence for Self-Interacting Cold Dark Matter. *Physical Review Letters 84* (Apr. 2000), 3760–3763.

[162] Spergel, D. N., Verde, L., Peiris, H. V., Komatsu, E., Nolta, M. R., Bennett, C. L., Halpern, M., Hinshaw, G., Jarosik, N., Kogut, A., Limon, M., Meyer, S. S., Page, L., Tucker, G. S., Weiland, J. L., Wollack, E., and Wright, E. L. First-Year Wilkinson Microwave Anisotropy Probe (WMAP) Observations: Determination of Cosmological Parameters. *ApJS 148* (Sept. 2003), 175–194.

[163] Splinter, R. J., Melott, A. L., Linn, A. M., Buck, C., and Tinker, J. The Ellipticity and Orientation of Clusters of Galaxies in N-Body Experiments. *ApJ 479* (Apr. 1997), 632.

[164] Springel, V. The cosmological simulation code GADGET-2. *MNRAS 364* (Dec. 2005), 1105–1134.

[165] Springel, V., Yoshida, N., and White, S. D. M. GADGET: a code for collisionless and gasdynamical cosmological simulations. *New Astronomy 6* (Apr. 2001), 79–117.

[166] Stadel, J., Potter, D., Moore, B., Diemand, J., Madau, P., Zemp, M., Kuhlen, M., and Quilis, V. Quantifying the heart of darkness with GHALO - a multibillion particle simulation of a galactic halo. *MNRAS 398* (Sept. 2009), L21–L25.

[167] Strigari, L. E., Kaplinghat, M., and Bullock, J. S. Dark matter halos with cores from hierarchical structure formation. *PhRvD 75*, 6 (Mar. 2007), 061303.

[168] Swaters, R. A., Sancisi, R., and van der Hulst, J. M. The H i Halo of NGC 891. *ApJ 491* (Dec. 1997), 140.

[169] Tegmark, M., Strauss, M. A., Blanton, M. R., Abazajian, K., Dodelson, S., Sandvik, H., Wang, X., Weinberg, D. H., Zehavi, I., Bahcall, N. A., Hoyle, F., Schlegel, D., Scoccimarro, R., Vogeley, M. S., Berlind, A., Budavari, T., Connolly, A., Eisenstein, D. J., Finkbeiner, D., Frieman, J. A., Gunn, J. E., Hui, L., Jain, B., Johnston, D., Kent, S., Lin, H., Nakajima, R., Nichol, R. C., Ostriker, J. P., Pope, A., Scranton, R., Seljak, U., Sheth, R. K., Stebbins, A., Szalay, A. S., Szapudi, I., Xu, Y., Annis, J., Brinkmann, J., Burles, S., Castander, F. J., Csabai, I., Loveday, J., Doi, M., Fukugita, M., Gillespie, B., Hennessy, G., Hogg, D. W., Ivezić, Ž., Knapp, G. R., Lamb, D. Q., Lee, B. C., Lupton, R. H., McKay, T. A., Kunszt, P., Munn, J. A., O'Connell, L., Peoples, J., Pier, J. R., Richmond, M., Rockosi, C., Schneider, D. P., Stoughton, C., Tucker, D. L., vanden Berk, D. E., Yanny, B., and York, D. G. Cosmological parameters from SDSS and WMAP. *PhRvD 69*, 10 (May 2004), 103501.

[170] Teyssier, R., Pires, S., Prunet, S., Aubert, D., Pichon, C., Amara, A., Benabed, K., Colombi, S., Refregier, A., and Starck, J.-L. Full-sky weak-lensing simulation with 70 billion particles. *Astron. Astrophys. 497* (Apr. 2009), 335–341.

 doi:10.20944/preprints202303.0387.v1

[171] Teyssier, R., Pires, S., Prunet, S., Aubert, D., Pichon, C., Amara, A., Benabed, K., Colombi, S., Refregier, A., and Starck, J.-L. Full-sky weak-lensing simulation with 70 billion particles. *AA 497* (Apr. 2009), 335–341.

[172] The Dark Energy Survey Collaboration. The Dark Energy Survey. *ArXiv Astrophysics e-prints: astro-ph/0510346* (Oct. 2005).

[173] Tinker, J., Kravtsov, A. V., Klypin, A., Abazajian, K., Warren, M., Yepes, G., Gottlöber, S., and Holz, D. E. Toward a Halo Mass Function for Precision Cosmology: The Limits of Universality. *ApJ 688* (Dec. 2008), 709–728.

[174] Tormen, G. The rise and fall of satellites in galaxy clusters. *MNRAS 290* (Sept. 1997), 411–421.

[175] Tyson, J. A., Wenk, R. A., and Valdes, F. Detection of systematic gravitational lens galaxy image alignments - Mapping dark matter in galaxy clusters. *ApJL 349* (Jan. 1990), L1–L4.

[176] Tyson, J. A., Wittman, D. M., Hennawi, J. F., and Spergel, D. N. LSST: a complementary probe of dark energy. *Nuclear Physics B Proceedings Supplements 124* (July 2003), 21–29.

[177] Vale, C., and White, M. Simulating Weak Lensing by Large-Scale Structure. *ApJ 592* (Aug. 2003), 699–709.

[178] Van Waerbeke, L., Mellier, Y., Erben, T., Cuillandre, J. C., Bernardeau, F., Maoli, R., Bertin, E., McCracken, H. J., Le Fèvre, O., Fort, B., Dantel-Fort, M., Jain, B., and Schneider, P. Detection of correlated galaxy ellipticities from CFHT data: first evidence for gravitational lensing by large-scale structures. *Astron. Astrophys. 358* (June 2000), 30–44.

[179] Van Waerbeke, L., Mellier, Y., and Hoekstra, H. Dealing with systematics in cosmic shear studies: New results from the VIRMOS-Descart survey. *AA 429* (Jan. 2005), 75–84.

[180] Viola, M., Melchior, P., and Bartelmann, M. Shear-flexion cross-talk in weak-lensing measurements. *MNRAS 419* (Jan. 2012), 2215–2225.

 doi:10.20944/preprints202303.0387.v1

[181] Wang, J., and White, S. D. M. Are mergers responsible for universal halo properties? *MNRAS 396* (June 2009), 709–717.

[182] Warren, M. S., Abazajian, K., Holz, D. E., and Teodoro, L. Precision Determination of the Mass Function of Dark Matter Halos. *ApJ 646* (Aug. 2006), 881–885.

[183] Warren, M. S., Quinn, P. J., Salmon, J. K., and Zurek, W. H. Dark halos formed via dissipationless collapse. I - Shapes and alignment of angular momentum. *ApJ 399* (Nov. 1992), 405–425.

[184] Weinberg, D. H., Mortonson, M. J., Eisenstein, D. J., Hirata, C., Riess, A. G., and Rozo, E. Observational probes of cosmic acceleration. *PhR 530* (Sept. 2013), 87–255.

[185] Wittman, D. M., Tyson, J. A., Kirkman, D., Dell'Antonio, I., and Bernstein, G. Detection of weak gravitational lensing distortions of distant galaxies by cosmic dark matter at large scales. *Nature 405* (May 2000), 143–148.

[186] Wright, C. O., and Brainerd, T. G. Gravitational Lensing by NFW Halos. *ApJ 534* (May 2000), 34–40.

[187] Yoshida, N., Springel, V., White, S. D. M., and Tormen, G. Weakly Self-interacting Dark Matter and the Structure of Dark Halos. *ApJL 544* (Dec. 2000), L87–L90.